

Matter trispectrum: theoretical modelling and comparison to N-body simulations

Davide Gualdi,^{a,b} Sergi Novell,^a Héctor Gil-Marín^{a,b} and Licia Verde^{a,c}

^aInstitut de Ciències del Cosmos, University of Barcelona, ICCUB, Barcelona 08028, Spain

^bInstitute of Space Studies of Catalonia (IEEC), E-08034 Barcelona, Spain

^cInstitució Catalana de Recerca i Estudis Avançats, Passeig Lluís Companys 23, Barcelona 08010, Spain

E-mail: dgualdi@icc.ub.edu, sergi.novell@icc.ub.edu, hectorgil@icc.ub.edu,
liciaverde@icc.ub.edu

Abstract. The power spectrum has long been the workhorse summary statistics for large-scale structure cosmological analyses. However, gravitational non-linear evolution moves precious cosmological information from the two-point statistics (such as the power spectrum) to higher-order correlations. Moreover, information about the primordial non-Gaussian signal lies also in higher-order correlations. Without tapping into these, that information remains hidden. While the three-point function (or the bispectrum), even if not extensively, has been studied and applied to data, there has been only limited discussion about the four point/trispectrum. This is because the high-dimensionality of the statistics (in real space a skew-quadrilateral has 6 degrees of freedom), and the high number of skew-quadrilaterals, make the trispectrum numerically and algorithmically very challenging. Here we address this challenge by studying the i-trispectrum, an integrated trispectrum that only depends on four k -modes moduli. We model and measure the matter i-trispectrum from a set of 5000 QUIJOTE N-body simulations both in real and redshift space, finding good agreement between simulations outputs and model up to mildly non-linear scales. Using the power spectrum, bispectrum and i-trispectrum joint data-vector covariance matrix estimated from the simulations, we begin to quantify the added-value provided by the i-trispectrum. In particular, we forecast the i-trispectrum improvements on constraints on the local primordial non-Gaussianity amplitude parameters f_{nl} and g_{nl} . For example, using the full joint data-vector, we forecast f_{nl} constraints up to two times ($\sim 32\%$) smaller in real (redshift) space than those obtained without i-trispectrum.

Contents

| | | |
|----------|--|-----------|
| 1 | Introduction | 2 |
| 2 | Methodology, theory modelling and estimators | 4 |
| 2.1 | Theoretical models of the signals | 5 |
| 2.1.1 | Redshift space i-trispectrum: coordinates | 7 |
| 2.2 | Estimators: measuring P , B , \mathcal{T} of an overdensity field | 8 |
| 2.2.1 | i-trispectrum | 9 |
| 2.3 | Covariance matrix estimation and modelling | 12 |
| 2.4 | Primordial non-Gaussianity imprint on the i-trispectrum | 14 |
| 2.5 | Fisher-based forecasts | 16 |
| 3 | Results | 19 |
| 3.1 | Real space: measure vs. model | 19 |
| 3.1.1 | Analysis set-up | 19 |
| 3.1.2 | Power spectrum and bispectrum | 19 |
| 3.1.3 | i-trispectrum | 22 |
| 3.1.4 | Covariance matrix and Gaussian term analytical model | 26 |
| 3.2 | Primordial non-Gaussianity constraints: forecasts | 27 |
| 3.3 | Redshift space | 30 |
| 4 | Conclusions | 33 |
| A | Theoretical models for power spectrum, bispectrum and i-trispectrum | 37 |
| B | Estimators definition | 39 |
| B.1 | Power spectrum | 40 |
| B.2 | Bispectrum | 41 |
| B.3 | I-trispectrum | 42 |
| B.3.1 | I-trispectrum: connected part and total signal | 43 |
| B.3.2 | Unconnected part | 43 |
| C | Shot-noise correction | 46 |
| D | I-trispectrum covariance: Gaussian term in redshift space | 48 |
| E | Primordial non-Gaussianity | 49 |
| E.1 | Power spectrum | 50 |
| E.2 | Bispectrum | 51 |
| E.3 | Trispectrum | 51 |
| E.3.1 | $T_{(1111)}$ | 52 |
| E.3.2 | $T_{(1112)}$ | 55 |
| E.4 | Recap: all PNG terms | 60 |

1 Introduction

The clustering of large-scale structure (LSS) encloses key information about both the primordial Universe, including the physics of inflation, and the growth of cosmological perturbations which are driven by gravity and the physics of the late-time Universe. Future and forthcoming large-scale structure surveys (e.g., DESI¹ [60]; Euclid² [55]; PFS³ [23]; SKA⁴ [6]; LSST⁵ [1] and WFIRST⁶ [35]) will cover unprecedented effective volumes, giving in principle access to this wealth of cosmological information.

While Bayesian hierarchical modelling, likelihood-free or forward modelling approaches (e.g., [5, 71, 93] and Refs. therein) are extremely promising, to date the workhorse approach still consists in considering and analysing summary statistics. The most popular is, of course, the power spectrum –the Fourier space counterpart of the two-point correlation function– which for a Gaussian random field encloses all the information. However, deviations from Gaussianity induced, e.g., by non-linear gravitational evolution but also of primordial origin, generate higher-order statistics. The bispectrum –the Fourier space counterpart of the three-point correlation function– is the next-to-leading-order statistic and it has been studied somewhat extensively. However, bispectrum measurements from galaxy surveys and their cosmological interpretation is still to a certain degree limited ([33, 76, 88, 99]). This is due to the fact that it is much more challenging and computationally intensive to measure the bispectrum signal, estimate its covariance matrix, account for its selection effects, than it is for the power spectrum.

The trispectrum –the connected part of the four-point correlation function in Fourier space– is even more off the beaten track. The trispectrum is non-zero when four k -vectors make a closed *skew-quadrilateral* (i.e., it is embedded in a 3D space). For simplicity we will loosely use the term *quadrilateral* from now on, but one should keep in mind that we refer to sets of four k -vectors that do not necessarily lie on the same plane. Note that the trispectrum is the lowest-order correlation where the connected part needs to be explicitly disentangled from the unconnected part. In other words, the ensemble average of four Fourier modes whose k -vectors make a closed quadrilateral would be, in general, non-zero even for a Gaussian random field. But what carries additional information not enclosed in the power spectrum is the connected part of that statistic.

While for the cosmic microwave background (CMB) fluctuations the trispectrum has been studied in detail and has been measured [4, 22, 24, 25, 43, 50, 52, 54, 66–68, 72, 85], in the late-time large-scale structure context it has received limited attention [11, 18, 57, 98] mainly focused on its relation with the power spectrum covariance matrix [65, 70, 92]. An effective field theory model of the trispectrum was derived in [12] while a formalism in angular space was recently proposed by [58]. In the presence of a primordial trispectrum, the correction to the non-Gaussian linear bias was derived in [56] Applications of the trispectrum to data are at an even more embryonic stage. The four-point correlation function in configuration space, was originally measured by [27] from the Lick and Zwicky catalogs, from simulations by [90] and recently at small scales from the BOSS NGC CMASS galaxy catalog by [73].

¹<http://desi.lbl.gov>

²<http://sci.esa.int/euclid/>

³<http://pfs.ipmu.jp>

⁴<https://www.skatelescope.org>

⁵<https://www.lsst.org/>

⁶<http://www.cosmos.esa.int/web/wfirst>

CMB studies on the trispectrum have proved its additional constraining power in particular regarding possibly primordial non-Gaussianities, which could confirm or rule out models of the very early Universe (e.g., single/multi field inflation). Even if more noisy and difficult to model due to non-linear gravitational evolution, the late-time 3D matter field trispectrum contains by definition many more modes than the primordial 2D CMB counterpart. It is reasonable to expect that, if measurable, it will provide additional information regarding the same primordial non-Gaussianity parameters. This was also the initial motivation stressed in [98] to look at this statistic.

Therefore the ultimate question we want to address is: "Is there additional information in the matter/halo/galaxy fields which is not captured by the power spectrum and bispectrum but that could be extracted by considering also the trispectrum?". In this paper, as a first step we focus on the matter field. Only if this idealised case shows that there is additional useful information in the trispectrum, then it would provide motivation to extend the treatment to more complex and realistic cases.

Studying the LSS trispectrum is massively more challenging for several reasons. On the theoretical and modelling side, several physical processes contribute to the trispectrum signal: not only a possible primordial signature and systematics/foreground effects as in the CMB, but also the mode-coupling arising from gravity and (non-linear) gravitational clustering. Moreover, the trispectrum of galaxies or other dark matter tracers is also affected by real-world effects such as redshift space distortions and galaxy bias, which need to be modelled consistently (i.e., at least up to third order in perturbation theory).

On the more practical side of measuring the signal from (real or simulated) data, in the CMB only co-planar quadrilaterals are considered, but in the three-dimensional LSS space, the number of quadrilateral configurations increases very rapidly. This has been to-date the showstopper for considering the trispectrum of LSS.

In this paper we address this challenge by considering a specific type of integrated trispectrum of the late-time dark matter overdensity field, which we will call for simplicity i-trispectrum and that depends only on the modulus of the four k -modes (k_1, k_2, k_3, k_4). A first attempt to consider such an estimator was done in [83]. Here we pay particular attention to the numerical implementation and the connection to the theoretical model. In particular in the approach presented here the theoretical model is significantly improved, by reducing drastically the adopted approximations and by performing the full multidimensional integration over the volume in Fourier space.

As it will become apparent later, the i-trispectrum is an integrated trispectrum over (skew) quadrilaterals with all possible folding angles around a diagonal and all possible lengths of the diagonal. This reduces greatly the computational and algorithmic challenge and makes the trispectrum signal accessible.

The analysis is presented in both real and redshift space including possible primordial non-Gaussianities. The theoretical model can be easily extended to the galaxy field in redshift space using an appropriate bias expansion up to third order. The estimator can be directly applied to the galaxy field in redshift space, but this is left for future work.

Modelling the dark matter quantities is a necessarily unavoidable and non-trivial first step (and may in principle be useful for weak lensing applications). It enables us to assess how well the adopted theoretical model reproduces the measured statistics of the simulated dark matter field, before applying any kind of galaxy or halo bias prescription, or real-to-redshift space conversion.

The goal of this paper is to present a theoretical modelling of the dark matter (con-

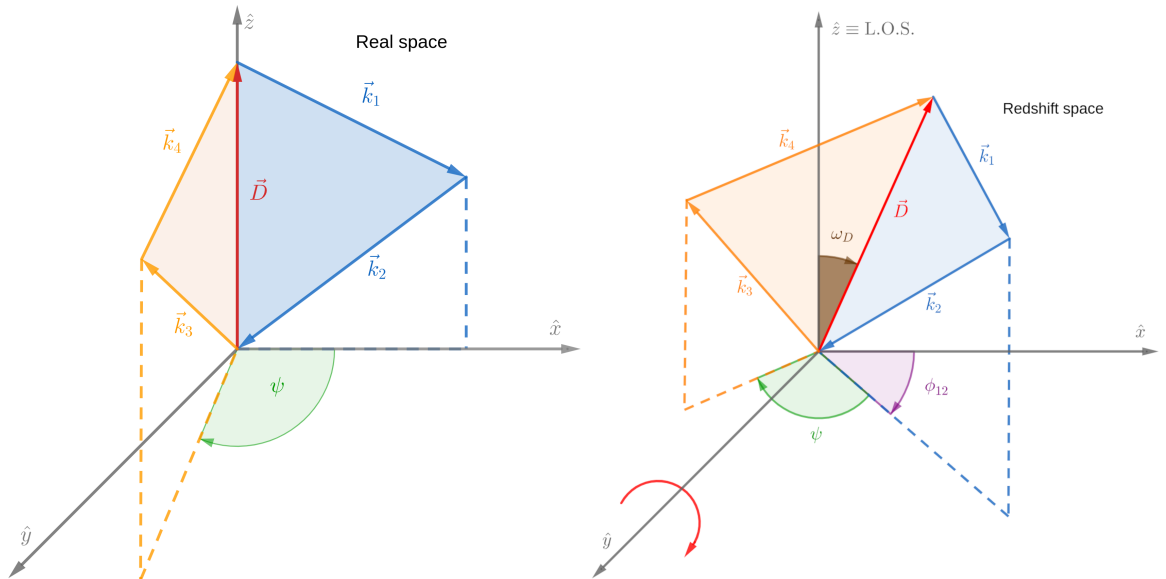


Figure 1. Trispectrum coordinates used to describe each configuration in the analytical model for T . On the left hand side the real space coordinate system. Without loss of generality the diagonal \mathbf{D} can be aligned with the z -axis and the triangle $\mathbf{k}_1 + \mathbf{k}_2 + \mathbf{D} = 0$ can be on the xz -plane. ψ denotes the folding angle of the quadrilateral. On the right hand side is the redshift space coordinate system. Now the line of sight is aligned with the z -axis and therefore another two angles are needed to fully describe the quadrilateral and its T : $\omega_D = \arccos \mu_D$ (the angle between \mathbf{D} and the line of sight., and ϕ_{12} (the angle between the xz -plane and the triangle $\mathbf{k}_1 + \mathbf{k}_2 + \mathbf{D} = 0$).

nected) i-trispectrum signal observed in N-body simulations of structure formation, and to highlight the challenges of characterising correctly its covariance matrix. We also quantify the added value of the i-trispectrum, when combined with power spectrum and bispectrum, especially for constraints on primordial non-Gaussianities. The rest of the paper is organised as follows. In section 2 the methodology of our analysis is presented, including the theoretical modelling of statistics (section 2.1), the estimators applied on the simulated data (section 2.2) and both local primordial non-Gaussianity theory and the formalism necessary for the Fisher forecasts (respectively sections 2.4 and 2.5). The results are presented in the second part of the paper, section 3. In particular, the real space analysis comparing theory with measurements is described in section 3.1 while the Fisher forecast for the primordial non-Gaussianity parameters is reported in section 3.2. Finally, the same analysis and forecasts performed in redshift space are reported in section 3.3. We conclude in section 4 where we also discuss possible further extension of this work.

2 Methodology, theory modelling and estimators

In view of our goal to investigate whether and how the i-trispectrum could be a powerful tool for cosmology, especially to further tighten the constraints on local primordial non-Gaussianity, we have to lay out a suitable methodology. We set out to model and measure the i-trispectrum signal of the dark matter particles field contained in a set of simulations with regular geometry. We use 5000 realisations of the QUIJOTE N-body suite [101].

A theoretical model for the i-trispectrum and an estimator for its measurement are introduced and validated. For completeness we also review the adopted theory model and

the estimators for the power spectrum and bispectrum. Power spectrum, bispectrum and trispectrum are the Fourier counterparts of the 2pt, 3pt and 4pt correlation functions in configuration space, respectively. In terms of averaged correlator of the Fourier transformed density field these are defined as

$$\begin{aligned}
\langle \delta(\mathbf{k}_1)\delta(\mathbf{k}_2) \rangle_c &= (2\pi)^3 \delta^D(\mathbf{k}_1 + \mathbf{k}_2) P(k_1) \\
\langle \delta(\mathbf{k}_1)\delta(\mathbf{k}_2)\delta(\mathbf{k}_3) \rangle_c &= (2\pi)^3 \delta^D(\mathbf{k}_1 + \mathbf{k}_2 + \mathbf{k}_3) B(\mathbf{k}_1, \mathbf{k}_2, \mathbf{k}_3) \\
\langle \delta(\mathbf{k}_1)\delta(\mathbf{k}_2)\delta(\mathbf{k}_3)\delta(\mathbf{k}_4) \rangle_c &= (2\pi)^3 \delta^D(\mathbf{k}_1 + \mathbf{k}_2 + \mathbf{k}_3 + \mathbf{k}_4) T(\mathbf{k}_1, \mathbf{k}_2, \mathbf{k}_3, \mathbf{k}_4),
\end{aligned}
\tag{2.1}$$

where the subscript "c" stands for connected. In the following sub-sections, after introducing the modeling for the data-vectors, the i-trispectrum covariance (both auto and cross-covariance with the power spectrum and bispectrum) is presented and estimated. With this in hand, we perform a Fisher forecast using a theoretical model for the primordial non-Gaussianity signal.

The methodology is described here and the results are presented in section 3.

2.1 Theoretical models of the signals

Our theory model for the matter power spectrum is provided by the CLASS code [59], which returns both the linear and non-linear power spectrum via the HALOFIT [13, 86, 91] fitting formula⁷. We model the tree-level matter bispectrum in two ways: using the second-order standard perturbation theory kernel $F_{\text{SPT}}^{(2)}[\mathbf{k}_1, \mathbf{k}_2]$ [28, 69], which is derived from first principles, and with its effective version $F_{\text{EFF}}^{(2)}[\mathbf{k}_1, \mathbf{k}_2]$ [31, 34], which was calibrated on simulations using the measured non-linear matter power spectrum (P_{nl}) as input. In what follows, unless otherwise stated, the linear power spectrum is indicated by P . Therefore for the bispectrum in real space we have

$$\begin{aligned}
B_{\text{SPT}}(\mathbf{k}_1, \mathbf{k}_2, \mathbf{k}_3) &= 2F_{\text{SPT}}^{(2)}[\mathbf{k}_1, \mathbf{k}_2] P(k_1) P(k_2) + 2 \text{ permutations}, \\
B_{\text{EFF}}(\mathbf{k}_1, \mathbf{k}_2, \mathbf{k}_3) &= 2F_{\text{EFF}}^{(2)}[\mathbf{k}_1, \mathbf{k}_2] P_{\text{nl}}(k_1) P_{\text{nl}}(k_2) + 2 \text{ p.},
\end{aligned}
\tag{2.2}$$

where we indicate the cyclical terms by "permutations" or "p". In the B_{EFF} case the non-linear power spectrum can either be provided by the measured quantity from the N-body simulations (this is the way how the kernel was originally calibrated), or alternatively, by HALOFIT. We also consider the "educated guess" bispectrum model which uses the standard perturbation theory tree-level F_2^{SPT} kernel with the HALOFIT non-linear power spectrum rather than the linear one

$$B_{\text{SPT-NL}}(\mathbf{k}_1, \mathbf{k}_2, \mathbf{k}_3) = 2F_{\text{SPT}}^{(2)}[\mathbf{k}_1, \mathbf{k}_2] P_{\text{nl}}(k_1) P_{\text{nl}}(k_2) + 2 \text{ p.}
\tag{2.3}$$

The tree-level trispectrum model $T_{\text{SPT}}(\mathbf{k}_1, \mathbf{k}_2, \mathbf{k}_3, \mathbf{k}_4)$ has been already derived and presented in several works e.g., [28, 79]; here we use the standard perturbation theory expression reported in the appendix B3 of [38] which we briefly summarise also in appendix A. Appendix A

⁷A more recent fitting formula for the matter power spectrum also implemented in CLASS is HMCODE [63]. We tested that for the chosen k -range the difference between HALOFIT and HMCODE is negligible for our purposes

also reports the full expressions for the power spectrum, bispectrum and trispectrum theory models in redshift space for a biased tracer as a proxy for the galaxy field.

It is important to specify that by trispectrum, T , and thus by trispectrum model T_{SPT} , we mean the signal corresponding to a quadrilateral configuration of a given shape defined by the choice of the four k -vectors $(\mathbf{k}_1, \mathbf{k}_2, \mathbf{k}_3, \mathbf{k}_4)$. In particular, for the matter trispectrum in real space we use [28, 70]

$$\begin{aligned} T_{\text{SPT}}(\mathbf{k}_1, \mathbf{k}_2, \mathbf{k}_3, \mathbf{k}_4) &= 4P(k_1)P(k_2) \times \left\{ F_{\text{SPT}}^{(2)}[\mathbf{k}_1, -\mathbf{k}_{13}] F_{\text{SPT}}^{(2)}[\mathbf{k}_2, \mathbf{k}_{13}] P(k_{13}) \right. \\ &\quad \left. + F_{\text{SPT}}^{(2)}[\mathbf{k}_1, -\mathbf{k}_{14}] F_{\text{SPT}}^{(2)}[\mathbf{k}_2, \mathbf{k}_{14}] P(k_{14}) \right\} + 5\text{p.} \\ &\quad + 6 F_{\text{SPT}}^{(3)}[\mathbf{k}_1, \mathbf{k}_2, \mathbf{k}_3] P(k_1)P(k_2)P(k_3) + 3\text{p.}, \end{aligned} \quad (2.4)$$

where $k_{ij} = |\mathbf{k}_i + \mathbf{k}_j|$. The expression for the second- and third-order standard perturbation theory kernels $F_{\text{SPT}}^{(2,3)}$ can be found in Ref. [38]. As for the case of the bispectrum, in equation 2.4 we might use the linear matter power spectrum for P yielding T_{SPT} or a similar educated guess combining the non-linear matter power spectrum with standard perturbation theory kernels, yielding $T_{\text{SPT-NL}}$.

From equation 2.4, the expression for the theoretical model of the trispectrum, we can easily identify the two terms obtained by expanding the four-point correlator up to sixth order in δ [28]: $T_{\text{SPT}}(\mathbf{k}_1, \mathbf{k}_2, \mathbf{k}_3, \mathbf{k}_4) = T_{(1122)} + T_{(1113)}$ (see also section 2.4, Appendices B and E).

The matter trispectrum (in real space) is a statistic measured on an isotropic field. This reduces the number of degrees of freedom necessary to describe a quadrilateral configuration from eight (needed when the signal depends on the orientation with respect to the line of sight) down to six.

Here we use the convention illustrated in figure 1. We use as diagonal, \mathbf{D} , the one defined by $\mathbf{D} + \mathbf{k}_1 + \mathbf{k}_2 = 0$. The module of this diagonal can then vary between a minimum and a maximum value defined by

$$D_{\min} = \max[|k_1 - k_2|, |k_3 - k_4|] \quad \text{and} \quad D_{\max} = \min[|k_1 + k_2|, |k_3 + k_4|], \quad (2.5)$$

where the above conditions are imposed by the requirement that the triangles formed by the diagonal \mathbf{D} and the two k -vectors ($\{k_1, k_2\}$ and $\{k_3, k_4\}$) are closed. In real space, the orientation with respect to the line of sight does not matter and therefore, for each quadrilateral, one could choose to set the diagonal vector \mathbf{D} parallel to the line of sight direction (namely, z -axis). With this choice, the two triangles defined by $\mathbf{D} + \mathbf{k}_1 + \mathbf{k}_2 = 0$ and $\mathbf{D} - \mathbf{k}_3 - \mathbf{k}_4 = 0$ will be orthogonal to the xy -plane.

Finally, the angle ψ describes the "folding" of the quadrilateral around the diagonal \mathbf{D} , in other words, the angle between the two planes defined by the two triangles $\mathbf{D} + \mathbf{k}_1 + \mathbf{k}_2 = 0$ and $\mathbf{D} - \mathbf{k}_3 - \mathbf{k}_4 = 0$. It should be then clear that $T(\mathbf{k}_1, \mathbf{k}_2, \mathbf{k}_3, \mathbf{k}_4) \equiv T(k_1, k_2, k_3, k_4, D, \psi, [\omega, \phi_{12}])$ where ω, ϕ_{12} are varying only in the redshift space case (see section 2.1.1), because each $\mathbf{k}_1, \mathbf{k}_2, \mathbf{k}_3, \mathbf{k}_4$ set corresponds univocally to a $\{k_1, k_2, k_3, k_4, D, \psi, [\omega, \phi_{12}]\}$ set and vice versa. We choose to study an averaged version of the trispectrum signal which we call i-trispectrum, with each configuration described only by the modulus of the four quadrilateral sides, $\mathcal{T}(k_1, k_2, k_3, k_4)$. In other words, we integrate out, by averaging over all their possible values, the additional two coordinates needed to fully describe a quadrilateral configuration (in real space). According to our adopted convention (figure 1) this means integrating over D and ψ . The redshift space i-trispectrum (see section 2.1.1) monopole is further averaged over ω and ϕ_{12} .

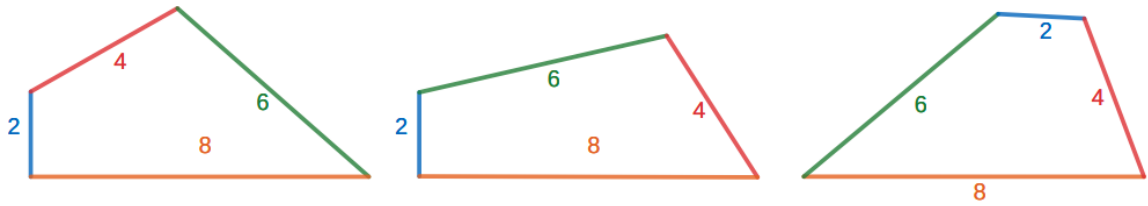


Figure 2. Different quadrilateral shapes allowed for a given choice of (k_1, k_2, k_3, k_4) . The estimator from equation 2.16 automatically averages over all these configurations and that is the reason of the sum in equation 2.6 and 2.7.

Therefore, differently from what happens for the power spectrum (line) and the bispectrum (triangle), the i-trispectrum signal as a function of just (k_1, k_2, k_3, k_4) is an average over many different shapes characterised by different values of one diagonal D and the folding angle around it ψ . The second diagonal that could be used as coordinate and its folding angle is fixed by choosing the first coordinates pair $\{D, \psi\}$.

Following these conventions, we define matter i-trispectrum in real space as a function of the module of the four k -vectors k_1, k_2, k_3, k_4 as

$$\mathcal{T}(k_1, k_2, k_3, k_4) = \frac{1}{3} \sum_{\substack{k_1, k_2, k_3, k_4 \\ k_1, k_3, k_2, k_4 \\ k_1, k_2, k_4, k_3}} \frac{1}{2\pi\Delta D} \int_{D_{\min}}^{D_{\max}} dD \int_0^{2\pi} d\psi T(k_1, k_2, k_3, k_4, D, \psi), \quad (2.6)$$

where $\Delta D = D_{\max} - D_{\min}$. Given a (k_1, k_2, k_3, k_4) set, three different shapes can be obtained by changing the order of the sides, this being the reason for the average in equation 2.6.

This can be understood by looking at the sketch in figure 2. The three different shapes are obtained by changing the ordering of the sides (k_1, k_2, k_3, k_4) ; for simplicity quadrilaterals shown lie on a plane i.e., no folding around the diagonal is shown in the sketch, where the diagonal D is always defined from the first two entries of T 's arguments.

From equation 2.6 is easy to appreciate the improvement over [83] comparing with their equation 34. While they approximate the theoretical model for the integrated trispectrum estimator using an amplitude factor, here we perform explicitly the full multi-dimensional integration in Fourier space.

The corresponding estimator applied on data will be later defined in equation 2.16. In appendix A the theoretical models for redshift space power spectrum, bispectrum and trispectrum are briefly reported.

2.1.1 Redshift space i-trispectrum: coordinates

When redshift space distortions are present, and in the partial sky/plane parallel approximation, the signal is not isotropic anymore [41, 48]. The preferred direction is given by the line of sight, which, by convention, we align with the \hat{z} direction. Hence, compared to the real space case discussed above, in order to define the orientation with respect to the line of sight of all the possible quadrilaterals (defined by the set of coordinates $(k_1, k_2, k_3, k_4, D, \psi)$), only two additional parameters are necessary.

First we define an angle ϕ_{12} to describe the rotation of the triangle $\mathbf{D} + \mathbf{k}_1 + \mathbf{k}_2 = 0$ away from the xz -plane (illustrated in the right part of figure 1).

As remaining parameter we choose the cosine of the angle between the diagonal, \mathbf{D} , and the line of sight, μ_D . Then by rotating each vector by an angle $\omega_D = \arccos \mu_D$, together with the choice of angles (ψ, ϕ_{12}) , all the possible orientations/shapes can be defined (and spanned when integrating over).

It is indeed important to notice that the orientation with respect to the quadrilateral line of sight, together with its shape, can also be modified by varying both angles ϕ_{12} and ψ . These three variables (ψ, ϕ_{12}, μ_D) may be used as a natural basis for an expansion in terms of Legendre polynomials of the full anisotropic i-trispectrum signal. The redshift space i-trispectrum monopole $\mathcal{T}^{(0)}$ can be obtained by performing the four-dimensional integration of the redshift space trispectrum, T^S :

$$\begin{aligned} \mathcal{T}^{(0)}(k_1, k_2, k_3, k_4) &= \frac{1}{3} \sum_{\substack{k_1, k_2, k_3, k_4 \\ k_1, k_3, k_2, k_4 \\ k_1, k_2, k_4, k_3}} \frac{1}{8\pi^2 \Delta D} \int_{D_{\min}}^{D_{\max}} dD \int_{-1}^{+1} d\mu_D \int_0^{2\pi} d\phi_{12} \int_0^{2\pi} d\psi \\ &\times T^S(k_1, k_2, k_3, k_4, D, \mu_D, \phi_{12}, \psi). \end{aligned} \quad (2.7)$$

2.2 Estimators: measuring \mathbf{P} , \mathbf{B} , \mathcal{T} of an overdensity field

Given an overdensity field, we need a procedure to estimate the statistics of interest: power spectrum, bispectrum and i-trispectrum. The overdensity field, as sampled for example by particles or haloes in an N-body simulation or by galaxies in a survey, is a discrete distribution, which contains a shot-noise contribution to the measured statistics. The first step is then to distribute through a mass assignment scheme (see for example [45, 82]) each particle's contribution to a cell in a three-dimensional discrete grid, in order to derive a pixelised overdensity distribution $\delta_{\mathbf{x}}$. Then, estimators should be adapted to take advantage of discrete Fast Fourier Transforms algorithms (FFT) [29]. This procedure is described in detail in appendices B (and C for what concerns the shot-noise subtraction). We review here the key steps and present the main results derived following the approach introduced by Refs. [74, 75] and used also in Ref. [97]. We will start here writing integrals (as in an idealized case where the fields were continuous and the volume infinite) and not discrete sums (realistic case for pixelized fields and finite volumes) to define the estimators in Fourier space to better show the fundamental connection between theoretical modelling and numerical implementation of the estimators. Given a cubic realisation of size L and volume $V = L^3$, the overdensity $\delta_{\mathbf{x}}$ is usually pixelised within N^3 cells whose volume is V/N^3 .

Starting from the expressions for the direct and inverse Fourier transforms of the matter density perturbation field,

$$\delta_{\mathbf{k}} = \int d\mathbf{x}^3 \delta_{\mathbf{x}} e^{i\mathbf{k}\mathbf{x}} \quad \text{and} \quad \delta_{\mathbf{x}} = \frac{1}{(2\pi)^3} \int d\mathbf{k}^3 \delta_{\mathbf{k}} e^{-i\mathbf{k}\mathbf{x}}, \quad (2.8)$$

where the integration is over the whole volume in configuration and Fourier space, the following quantities can be defined:

$$I_k(\mathbf{x}) = \int_k \frac{d\mathbf{q}^3}{(2\pi)^3} \delta_{\mathbf{q}} e^{-i\mathbf{x}\mathbf{q}} \quad \text{and} \quad J_k(\mathbf{x}) = \int_k \frac{d\mathbf{q}^3}{(2\pi)^3} e^{-i\mathbf{x}\mathbf{q}}, \quad (2.9)$$

where the integration is over the spherical shell with radius defined by the k -vector module and with thickness Δk . Given these ingredients, we can define the integral version of the

power spectrum estimator (bandpower evaluated in a thin shell around k_1):

$$\begin{aligned}\hat{P}(k_1) &= \frac{(2\pi)^{-3}}{N_p} \int_{k_1} d\mathbf{q}_1^3 \int_{k_2} d\mathbf{q}_2^3 \delta_{\mathbf{q}_1} \delta_{\mathbf{q}_2} \delta^D(\mathbf{q}_1 + \mathbf{q}_2) \\ &= \frac{k_f^3}{(2\pi)^3} \frac{\int_{k_1} d\mathbf{q}_1^3 \int_{k_1} d\mathbf{q}_2^3 \delta_{\mathbf{q}_1} \delta_{\mathbf{q}_2} \delta^D(\mathbf{q}_1 + \mathbf{q}_2)}{\int_{k_1} d\mathbf{q}_1^3 \int_{k_1} d\mathbf{q}_2^3 \delta^D(\mathbf{q}_1 + \mathbf{q}_2)},\end{aligned}\quad (2.10)$$

where δ^D is the Dirac's delta and where each integral is performed over a spherical shell of radius k_i for $i = 1, 2$ and thickness Δk , the width of the bandpower. $N_p = V_p/k_f^3$ is the number of pairs found inside the integration volume in Fourier space, where $V_p = 4\pi k^2 \Delta k$ is the integration volume in Fourier space while $k_f = 2\pi/L$ is the box's fundamental frequency. Converting the integrals into discrete sums as described in appendix B the estimator becomes

$$\hat{P}(k_1) = \frac{L^3}{N^6} \sum_{i=1}^{N^3} I_{k_1}^D(x_i) I_{k_1}^D(x_i) \times \left[\sum_{j=1}^{N^3} J_{k_1}^D(y_j) J_{k_1}^D(y_j) \right]^{-1}, \quad (2.11)$$

where I^D and J^D (full expression reported in equation B.10) denote the pixelized (D stands for discrete as a pixelized version of a continuous field is often referred to as "discretized") of the quantities defined in equation 2.9 for a grid with N^3 cells.

Similarly, for the bispectrum we start from the unbiased estimator

$$\begin{aligned}\hat{B}(k_1, k_2, k_3) &= \frac{V(2\pi)^{-6}}{N_t} \int_{k_1} d\mathbf{q}_1^3 \int_{k_2} d\mathbf{q}_2^3 \int_{k_3} d\mathbf{q}_3^3 \delta_{\mathbf{q}_1} \delta_{\mathbf{q}_2} \delta_{\mathbf{q}_3} \delta^D(\mathbf{q}_1 + \mathbf{q}_2 + \mathbf{q}_3) \\ &= \frac{V k_f^6}{(2\pi)^6} \frac{\int_{k_1} d\mathbf{q}_1^3 \int_{k_2} d\mathbf{q}_2^3 \int_{k_3} d\mathbf{q}_3^3 \delta_{\mathbf{q}_1} \delta_{\mathbf{q}_2} \delta_{\mathbf{q}_3} \delta^D(\mathbf{q}_1 + \mathbf{q}_2 + \mathbf{q}_3)}{\int_{k_1} d\mathbf{q}_1^3 \int_{k_2} d\mathbf{q}_2^3 \int_{k_3} d\mathbf{q}_3^3 \delta^D(\mathbf{q}_1 + \mathbf{q}_2 + \mathbf{q}_3)},\end{aligned}\quad (2.12)$$

where $N_t = V_t/k_f^6$ is the number of triangles included in the integration volume in Fourier space ($V_t = 8\pi^2 k_1 k_2 k_3 \Delta k^3$ is the integration volume in Fourier space for the bispectrum). As for the power spectrum, the above estimator can be expressed in terms of discrete sums (see equation B.14):

$$\hat{B}(k_1, k_2, k_3) = \left(\frac{L^6}{N^9} \right) \sum_{i=1}^{N^3} I_{k_1}^D(x_i) I_{k_2}^D(x_i) I_{k_3}^D(x_i) \times \left[\sum_{j=1}^{N^3} J_{k_1}^D(y_j) J_{k_2}^D(y_j) J_{k_3}^D(y_j) \right]^{-1}. \quad (2.13)$$

2.2.1 i-trispectrum

The idea to define an estimator for the trispectrum which depends only on the magnitude of the four k -modes defining the quadrilateral was pioneered by [83]. Here, using the approach of [75] we make the estimator fast enough to be applicable to a large set of independent synthetic realisations and eventually on data and, by performing explicitly the angular integrations, make it transparently connected to the theoretical model for the trispectrum.

Analogously to the power spectrum and bispectrum, the estimator for the four-point correlator could be defined as a quantity proportional to a suitable average of four $\delta_{\mathbf{k}}$ modes. However, differently from the power spectrum and bispectrum cases, this will not be a particularly useful i-trispectrum estimator; when taking the ensemble average of such quantity, two terms appear –according to Wick's theorem–: a connected (c) and an unconnected (u) part.

So the estimator simply identified with the four-point correlator estimator will include both these contributions:

$$\begin{aligned}
\hat{\mathcal{T}}_{\text{c+u}}(k_1, k_2, k_3, k_4) &= \frac{V^2(2\pi)^{-9}}{N_{\mathbf{q}}} \int_{k_1} d\mathbf{q}_1^3 \int_{k_2} d\mathbf{q}_2^3 \int_{k_3} d\mathbf{q}_3^3 \int_{k_4} d\mathbf{q}_4^3 \\
&\times \delta_{\mathbf{q}_1} \delta_{\mathbf{q}_2} \delta_{\mathbf{q}_3} \delta_{\mathbf{q}_4} \delta^D(\mathbf{q}_1 + \mathbf{q}_2 + \mathbf{q}_3 + \mathbf{q}_4) \\
&= \frac{V^2 k_{\text{f}}^9}{(2\pi)^9} \frac{\int_{k_1} d\mathbf{q}_1^3 \int_{k_2} d\mathbf{q}_2^3 \int_{k_3} d\mathbf{q}_3^3 \int_{k_4} d\mathbf{q}_4^3 \delta_{\mathbf{q}_1} \delta_{\mathbf{q}_2} \delta_{\mathbf{q}_3} \delta_{\mathbf{q}_4} \delta^D(\mathbf{q}_1 + \mathbf{q}_2 + \mathbf{q}_3 + \mathbf{q}_4)}{\int_{k_1} d\mathbf{q}_1^3 \int_{k_2} d\mathbf{q}_2^3 \int_{k_3} d\mathbf{q}_3^3 \int_{k_4} d\mathbf{q}_4^3 \delta^D(\mathbf{q}_1 + \mathbf{q}_2 + \mathbf{q}_3 + \mathbf{q}_4)},
\end{aligned} \tag{2.14}$$

where $N_{\mathbf{q}} = V_{\mathbf{q}}/k_{\text{f}}^9$ is the number of skew-quadrilaterals in the integration volume in Fourier space (see [39]'s appendix for a derivation of the trispectrum integration volume in Fourier space $V_{\mathbf{q}} = 16\pi^3 k_1 k_2 k_3 k_4 \Delta k^5$). Notice that this estimator automatically averages over all the possible shapes and permutations included in the model of equation 2.6.

In fact,

$$\begin{aligned}
\langle \hat{\mathcal{T}}_{\text{c+u}}(k_1, k_2, k_3, k_4) \rangle &= \frac{V^2(2\pi)^{-9}}{N_{\mathbf{q}}} \int_{k_1} d\mathbf{q}_1^3 \int_{k_2} d\mathbf{q}_2^3 \int_{k_3} d\mathbf{q}_3^3 \int_{k_4} d\mathbf{q}_4^3 \\
&\times [\langle \delta_{\mathbf{q}_1} \delta_{\mathbf{q}_2} \delta_{\mathbf{q}_3} \delta_{\mathbf{q}_4} \rangle_{\text{c}} + \langle \delta_{\mathbf{q}_1} \delta_{\mathbf{q}_2} \rangle \langle \delta_{\mathbf{q}_3} \delta_{\mathbf{q}_4} \rangle + 2\text{p.}] \delta^D(\mathbf{q}_1 + \mathbf{q}_2 + \mathbf{q}_3 + \mathbf{q}_4),
\end{aligned} \tag{2.15}$$

where $\langle \delta_{\mathbf{q}_1} \delta_{\mathbf{q}_2} \delta_{\mathbf{q}_3} \delta_{\mathbf{q}_4} \rangle_{\text{c}}$ denotes the connected i-trispectrum part, and the three permutations of the product of two terms proportional to the power spectrum ($\langle \delta_{\mathbf{q}_i} \delta_{\mathbf{q}_j} \rangle \langle \delta_{\mathbf{q}_{i'}} \delta_{\mathbf{q}_{j'}} \rangle$) are the unconnected part. The unconnected part is not of particular interest here, since it is completely determined by the field's power spectrum.

The signal of interest and the one we want to isolate is the connected part, the i-trispectrum. In other words, the i-trispectrum estimator should be obtained by subtracting the unconnected part from the total signal measured by the four-point correlator estimator in equation 2.14:

$$\hat{\mathcal{T}}(k_1, k_2, k_3, k_4) \equiv \hat{\mathcal{T}}_{\text{c}}(k_1, k_2, k_3, k_4) = \hat{\mathcal{T}}_{\text{c+u}}(k_1, k_2, k_3, k_4) - \hat{\mathcal{T}}_{\text{u}}(k_1, k_2, k_3, k_4). \tag{2.16}$$

In the cosmological context of interest and for Gaussian initial conditions, perturbation theory predicts the unconnected part (which is intrinsically a linear order quantity) to be dominant with respect to the connected one (which is intrinsically third order). This will later be proven using the simulations measurements, with the unconnected part resulting to be two orders of magnitude larger than the connected one.

As derived in appendix B.3.1 the discretised estimator for the total signal of the four-

point correlator in Fourier space is⁸

$$\begin{aligned} \hat{\mathcal{T}}_{c+u}(k_1, k_2, k_3, k_4) &= \frac{L^9}{N^{12}} \sum_{i=1}^{N^3} I_{k_1}^D(x_i) I_{k_2}^D(x_i) I_{k_3}^D(x_i) I_{k_4}^D(x_i) \\ &\times \left[\sum_{j=1}^{N^3} J_{k_1}^D(y_j) J_{k_2}^D(y_j) J_{k_3}^D(y_j) J_{k_4}^D(y_j) \right]^{-1}. \end{aligned} \quad (2.17)$$

In order to isolate the unconnected term and to subtract it from the total signal measured from the simulations we define the estimator

$$\begin{aligned} \hat{\mathcal{T}}_u(k_1, k_2, k_3, k_4) &= \frac{V(2\pi)^{-9}}{N_q} \int_{k_1} d\mathbf{q}_1^3 \int_{k_2} d\mathbf{q}_2^3 \delta_{\mathbf{q}_1} \delta_{\mathbf{q}_2} \delta^D(\mathbf{q}_1 + \mathbf{q}_2) \\ &\times \int_{k_3} d\mathbf{q}_3^3 \int_{k_4} d\mathbf{q}_4^3 \delta_{\mathbf{q}_3} \delta_{\mathbf{q}_4} \delta^D(\mathbf{q}_3 + \mathbf{q}_4) + 2 \text{ p.}, \end{aligned} \quad (2.18)$$

where the above expression captures the fact that the unconnected part by definition is non-zero when at least one of the terms $\propto P^2$ – each involving product of the two-point correlators $\langle \delta\delta \rangle \langle \delta\delta \rangle$ – is non-zero. This contribution then appears only for those quadrilaterals sets with two pairs of equal sides (or all four equal sides). The corresponding discretised estimator is (appendix B.3.2)

$$\begin{aligned} \hat{\mathcal{T}}_u(k_1, k_2, k_3, k_4) &= \frac{L^9}{N^{15}} \sum_{i=1}^{N^3} I_{k_1}^D(x_i) I_{k_2}^D(x_i) \sum_{\ell=1}^{N^3} I_{k_3}^D(z_\ell) I_{k_4}^D(z_\ell) \\ &\times \left[\sum_{j=1}^{N^3} J_{k_1}^D(y_j) J_{k_2}^D(y_j) J_{k_3}^D(y_j) J_{k_4}^D(y_j) \right]^{-1}. \end{aligned} \quad (2.19)$$

From equation 2.18 we can also derive an analytical expression to model the unconnected signal of the four-point correlator in Fourier space $\mathcal{T}_u^{\text{th}}$ (see equation B.22 for the derivation):

$$\langle \hat{\mathcal{T}}(k_1, k_2, k_3, k_4)_u \rangle \approx . \quad (2.20)$$

where δ_{ij}^K denotes the Kronecker delta for $\mathbf{k}_i - \mathbf{k}_j$ and S_{1234} is a symmetry factor whose value is one in case the quadrilateral has two pairs of equal sides, three if the four sides are the same and zero otherwise. It is important to notice that since the quadrilateral diagonal D is not a fixed parameter given the four sides, $\Delta D = D_{\text{max}} - D_{\text{min}}$. Δk_i are the bin sizes chosen for the k -modes and the diagonal D . These will be later defined in section 3.1.1 in terms of the fundamental frequency k_f given by the analysis set-up.

⁸Recall that we describe the i-trispectrum using only the four sides of the quadrilateral as coordinates and not also the diagonal (as introduced to compute the theoretical expression for the estimator). This is motivated by numerical computation time considerations. If we had used the diagonal D as additional coordinate, by writing the estimator with the closure conditions $\delta^D(\mathbf{q}_1 + \mathbf{q}_2 + \mathbf{D}) \times \delta^D(\mathbf{q}_3 + \mathbf{q}_4 - \mathbf{D})$, in the above expression there would have been a double sum over each grid element, implying a computation scaling as $\propto N^6$ instead of $\propto N^3$. Introducing the diagonal here is not necessary because the estimator defined as a function of (k_1, k_2, k_3, k_4) automatically integrates over all possible shapes given by the allowed values of the diagonal D (and the folding angle ψ).

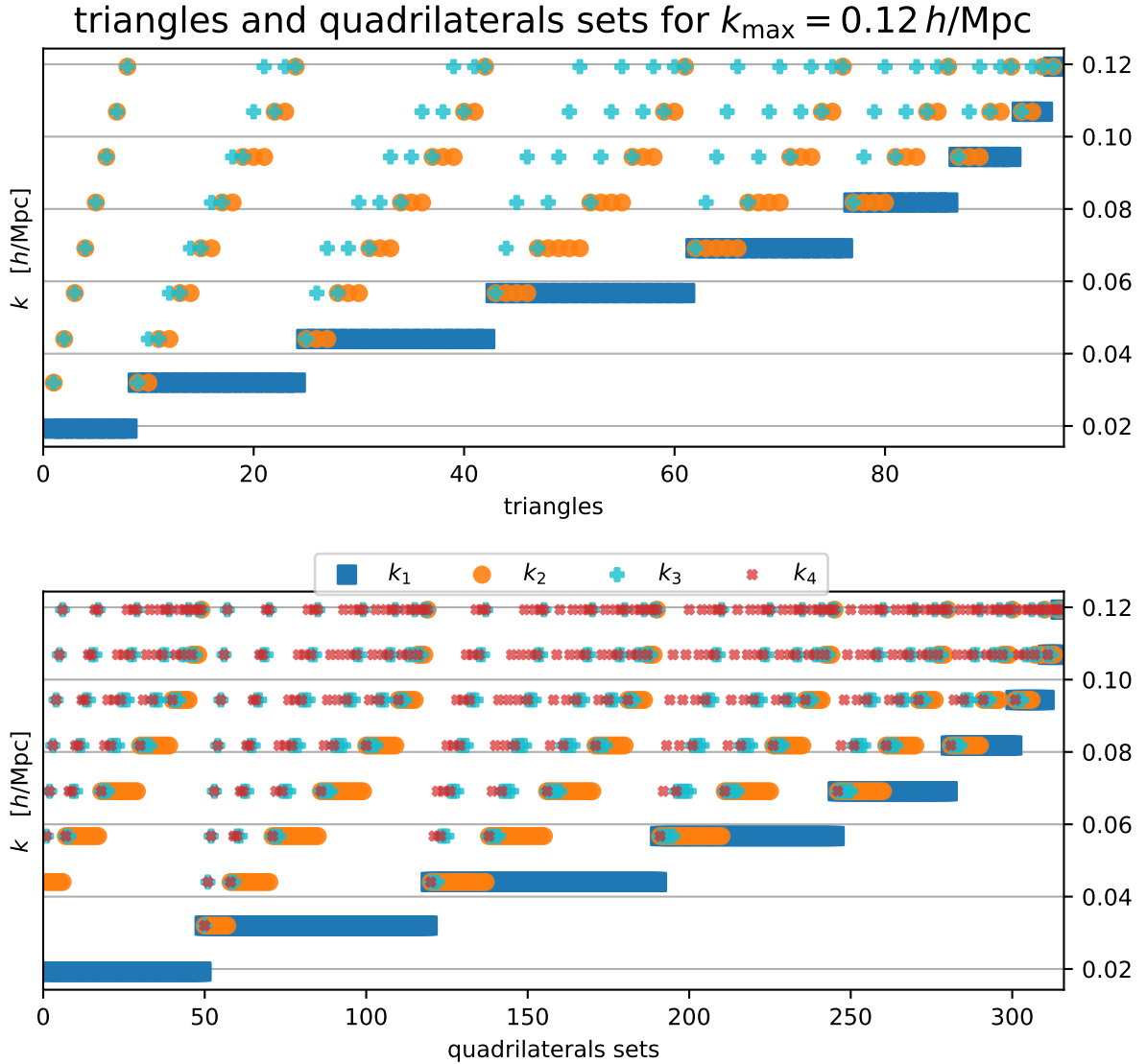


Figure 3. Illustration of the convention adopted for the ordering of triangles and quadrilaterals sets in the bispectrum and i-trispectrum data-vectors, respectively. k_1 increases from left to right while the other sides follow the ordering $k_1 \leq k_2 \leq k_3$ and $k_1 \leq k_2 \leq k_3 \leq k_4$ for both triangles and quadrilaterals sets.

We are aware that another option would be to simply discard all the symmetric configurations and by doing so avoiding the quadrilaterals sets whose i-trispectrum has an unconnected part. While an interesting avenue to explore, we find that it would imply a loss of constraining power, therefore here we proceed with the estimator of equation 2.16, since it allows harvesting the information contained in the i-trispectrum of symmetric configurations.

2.3 Covariance matrix estimation and modelling

The power spectrum, bispectrum and i-trispectrum for different k -bins, triangles and quadrilaterals sets can be organised into a data-vector. In our case, the measured power spectrum,

bispectrum and i-trispectrum joint data-vector is given by the elements

$$\mathbf{d} = \left(\hat{P}_{k_1}, \dots, \hat{P}_{k_{\max}^P}; \hat{B}_{k_1 k_1 k_1}, \dots, \hat{B}_{k_{\max}^B k_{\max}^B k_{\max}^B}; \hat{\mathcal{T}}_{k_1 k_1 k_1 k_1}, \dots, \hat{\mathcal{T}}_{k_{\max}^{\mathcal{T}} k_{\max}^{\mathcal{T}} k_{\max}^{\mathcal{T}} k_{\max}^{\mathcal{T}}} \right), \quad (2.21)$$

where each statistic is characterised by its own maximum k -value, k_{\max} . The theoretical counterpart of this data-vector is composed by the adopted model for each of the statistics, which we label \mathbf{d}_{th} . Sometimes for brevity we will refer to $\mathbf{d}(k_{\max})$ as the data-vector defined above measured for the same k_{\max} for all statistics. The configurations ordering for both bispectrum and i-trispectrum in terms of the k -values of the triangle and quadrilaterals sets sides is shown in figure 3. In order to avoid double-counting shapes, once k_1 is chosen the other sides respect the ordering $k_1 \leq k_2 \leq k_3$ and $k_1 \leq k_2 \leq k_3 \leq k_4$ for triangles and quadrilaterals sets respectively. In the figure, k_1 (in blue) increases from left to right and the x -axis reports the label (index) of the configuration. For each configuration the figure shows the length of k_2 (orange), k_3 (cyan) and k_4 (red).

Besides the estimator for the statistic of choice (which comprises the elements of the data-vector \mathbf{d}) and the theoretical expression of the estimator (elements of \mathbf{d}_{th}), the remaining key ingredient of all the parameter constraints analyses and forecasts is the covariance matrix, which encodes the uncertainty and correlation present in the data-vector. The uncertainty is related to the error associated with the individual element measurement while correlation quantifies how dependent to each other the different elements of the data-vector are.

The covariance matrix of the i-trispectrum and the cross-covariance with power spectrum and bispectrum are fundamental ingredients for assessing the impact of adding this four-point statistic to a parameter constraints analysis. In what follows, for brevity we refer to the full joint power spectrum, bispectrum and i-trispectrum covariance, or data-vector, as PBT . Usually in this kind of forecasts studies, an analytical template is used and often the covariance is assumed to be diagonal (i.e., no correlation between different k -bins), with only a Gaussian component (i.e., ignoring contributions from non-linear clustering), together with assuming no cross-correlation between different n -point statistics.

Alternatively, given a set of measurements from independent realisations of the data-vector \mathbf{d} of interest, the covariance matrix $\mathbf{Cov}_{\mathbf{d}}$ can be numerically estimated by

$$\mathbf{Cov}_{\mathbf{d}} = \frac{1}{N_{\text{sim}} - 1} \sum_{i=1}^{N_{\text{sim}}} (\mathbf{d}_i - \langle \mathbf{d} \rangle) (\mathbf{d}_i - \langle \mathbf{d} \rangle)^{\top}, \quad (2.22)$$

where N_{sim} is the number of independent realisations (here we use 5000 realisations see section 3.1) used to measure the data-vector and $\langle \mathbf{d} \rangle$ denotes the average across the whole set of realisations and \top denotes the transpose.

The inverse of a covariance matrix $\mathbf{Cov}_{\mathbf{d}}^{-1}$ estimated from a finite number of realisation is known to be biased [42, 84]. We correct this by using the Hartlap factor $h_f = (N_{\text{sim}} - N_{\mathbf{d}} - 2)/(N_{\text{sim}} - 1)$ [42], where $N_{\mathbf{d}}$ is the data-vector's size while N_{sim} is the number of simulations used to estimate the covariance (5000 in our case⁹). Notice that $h_f \rightarrow 1$ when $N_{\text{sim}} \gg N_{\mathbf{d}}$. A more accurate correction to the inverse of the covariance matrix estimated from a finite number of independent realisations and its effect on the resulting likelihood was introduced by [84]. We tested that for the purpose of evaluating the added benefit of including the i-trispectrum in the analysis, the difference between the two corrections is negligible.

⁹While the QUIJOTE [101] suite offers more than 5000 realisations, we only use 5000 for each redshift for computational reasons. Given the maximum length of our data-vector, this number is more than enough to estimate the inverse of the covariance matrix. In fact the Hartlap factor is $h_f = 0.51$ or higher.

Often the lack of a large number of independent realisations is the reason why resorting to an analytical model for the covariance is appealing. In particular, if the overdensity field can be approximated by a Gaussian random field, the covariance matrix can be modelled analytically (especially for simulated cubic boxes). We refer to this approximation as Gaussian and its non-zero terms in the covariance as Gaussian terms. Recent studies on the power spectrum and bispectrum covariance matrices and their analytical models can be found in Refs. [39, 89, 102].

For what concerns the i-trispectrum, we compute, for the first time, the Gaussian terms at leading order following the approach developed, for the power spectrum and bispectrum, in [37, 38].

The real space matter field i-trispectrum covariance matrix is a specific case of the more general covariance in redshift space for biased tracers, whose derivation is reported in the appendix D at equation D.1. Since the kernels of the real space matter field do not depend on the relative orientation of the k -vectors, and there is no dependence of each k -vector orientation with respect to the line of sight, no integration is required. Consequently, the analytical expression for the diagonal elements of \mathbf{Cov} in the Gaussian approximation (see equation D.1 for full expression) reduces to

$$C_G^{\mathcal{T}_u \mathcal{T}_u}(k_1, k_2, k_3, k_4) = \frac{(2\pi)^9 R_{1234}}{V_s V_{1234}^q} \times P(k_1) P(k_2) P(k_3) P(k_4), \quad (2.23)$$

where the expression of the Fourier integration volume, V_{1234}^q , is given in equation B.21; R_{1234} is a symmetry factor (given by $n!$, where n is the number of repeated k modules) that counts the number of possible permutations of equal sides between the two identical quadrilaterals sets, and its values for a given symmetry are given in equation D.2; V_s is the effective survey volume.

We will compare the diagonal elements of the covariance numerically estimated from the simulations with the above theoretical model later in section 3.1.4 to show that for the i-trispectrum the Gaussian approximation is only reasonable at high redshifts.

2.4 Primordial non-Gaussianity imprint on the i-trispectrum

Deviations from Gaussianity of the primordial gravitational potential [8] are a powerful tool to constrain models of inflation [10] describing how the large-scale structure we currently observe was generated. In this work we focus on primordial non-Gaussianities (PNG) of the local type which are parametrised by an amplitude parameter $f_{\text{nl}}^{\text{local}}$ (we will refer to it as f_{nl} from now on for simplicity). The Bardeen's gravitational potential Φ [8] can be written as a polynomial expansion in terms of a Gaussian field ϕ with coefficients f_{nl} and g_{nl} up to third order:

$$\Phi(\mathbf{x}) = \phi(\mathbf{x}) + \frac{f_{\text{nl}}}{c^2} [\phi^2(\mathbf{x}) - \langle \phi^2(\mathbf{x}) \rangle] + \frac{g_{\text{nl}}}{c^4} [\phi^3(\mathbf{x}) - 3\phi(\mathbf{x})\langle \phi^2(\mathbf{x}) \rangle] + \dots \quad (2.24)$$

where c is the speed of light which is needed in the expansion since in this formalism ϕ has units of c^2 . For more details see appendix E.

A detection of $|f_{\text{nl}}| \gtrsim 1$ would rule out single field inflationary models since they predict a much smaller value of the same parameter [19, 61], while at the same time it would favour multi-field inflationary models or alternatives to inflation. At the moment of writing, the

tightest constraints, from the *Planck* analysis of CMB data, are $f_{\text{nl}} = 0.9 \pm 5.1$ (at 68% confidence level) [4]. For large-scale structure, using the DR14 eBOSS quasars sample and exploiting the scale dependent bias effect induced by primordial non-Gaussianity [21, 62] (see [9] for a recent study on the impact of galaxy bias uncertainties on PNG constraints), the state of the art constraints are $-26 < f_{\text{nl}} < 14$ (at 68% confidence level) [15].

To date, only the bispectrum has been thoroughly studied in the literature for its sensitivity to primordial non-Gaussianity signatures at the lowest-order in perturbation theory [46, 53, 78, 79, 100]. Recently Ref. [39] suggested that the bispectrum anisotropic signal could boost even further the late-time constraints on f_{nl} . The expressions for the primordial non-Gaussianity contributions to the matter power spectrum and bispectrum are reported in appendix E.

The large-scale structure trispectrum as a test for Gaussianity of the initial conditions was proposed in [98]. Since then the trispectrum has been mainly considered for CMB analyses, targeted to produce constraints on primordial non-Gaussianity [25, 43, 50, 64, 66, 72, 85], in particular with *Planck* [24] deriving constraints on both $\tau_{\text{nl}} = 0.4 \pm 0.9 \times 10^4$ and $g_{\text{nl}} = -1.2 \pm 2.8 \times 10^5$. For what concerns late-time analyses, the 21-cm background anisotropies trispectrum was studied in Ref. [18], while Ref. [11] included the trispectrum of LSS to measure the energy-scale of inflation through its relation with primordial non-Gaussianities.

As described in detail in appendix E.3, and following [46, 79], one can see that in the presence of primordial non-Gaussianity, when expanding the four-point correlator (with shorthand notation $\langle \delta\delta\delta\delta \rangle$) whose connected component is the trispectrum, four terms appear:

$$\langle \delta\delta\delta\delta \rangle = T_{(1111)} + T_{(1112)} + T_{(1122)} + T_{(1113)}. \quad (2.25)$$

The third and fourth terms, $T_{(1122)}$ and $T_{(1113)}$, represent the standard trispectrum due to gravitational collapse (when limiting the expansion to order $\propto \delta^6$, or in terms of the Gaussian primordial potential $\propto \phi^6$). The first term $T_{(1111)}$ produces two terms proportional to f_{nl}^2 and g_{nl} , respectively. The second term $T_{(1112)}$ is a mixture of primordial non-Gaussianity and gravitational non-linear evolution and it is proportional to f_{nl} . Therefore the model for the primordial non-Gaussianity imprint on the matter trispectrum in real space, T^{PNG} , is given

by¹⁰,

$$\begin{aligned}
T^{\text{PNG}}(\mathbf{k}_1, \mathbf{k}_2, \mathbf{k}_3, \mathbf{k}_4) &= T_{(1111)} + T_{(1112)} \\
&= \times \left\{ \frac{f_{\text{nl}}^2}{c^4} 4 \frac{\mathcal{M}_{k_3} \mathcal{M}_{k_4}}{\mathcal{M}_{k_1} \mathcal{M}_{k_2}} P(k_1) P(k_2) \left[\frac{P(|\mathbf{k}_1 + \mathbf{k}_3|)}{\mathcal{M}_{|\mathbf{k}_1 + \mathbf{k}_3|}^2} + \frac{P(|\mathbf{k}_1 + \mathbf{k}_4|)}{\mathcal{M}_{|\mathbf{k}_1 + \mathbf{k}_4|}^2} \right] + 5 \text{ p.} \right. \\
&\quad \left. + \frac{g_{\text{nl}}}{c^4} \left[6 \mathcal{M}_{k_4} \frac{P(k_1) P(k_2) P(k_3)}{\mathcal{M}_{k_1} \mathcal{M}_{k_2} \mathcal{M}_{k_3}} + 3 \text{ p.} \right] \right\} \\
&\quad + \frac{f_{\text{nl}}}{c^2} \times \left\{ \left[4 \frac{\mathcal{M}_{k_1}}{\mathcal{M}_{k_2}} P(k_2) P(k_3) \frac{P(|\mathbf{k}_3 + \mathbf{k}_4|)}{\mathcal{M}_{|\mathbf{k}_3 + \mathbf{k}_4|}} F^{(2)}[-\mathbf{k}_3, \mathbf{k}_3 + \mathbf{k}_4] + 5 \text{ p.} \right] \right. \\
&\quad \left. + \left[2 \frac{\mathcal{M}_{|\mathbf{k}_3 + \mathbf{k}_4|}}{\mathcal{M}_{k_1} \mathcal{M}_{k_2}} P(k_1) P(k_2) P(k_3) F^{(2)}[\mathbf{k}_3 + \mathbf{k}_4, -\mathbf{k}_3] + 2 \text{ p.} \right] \right\} + 3 \text{ p.} .
\end{aligned} \tag{2.26}$$

where $\mathcal{M}_k = (3D_+/5\Omega_m H_0^2) k^2 \mathbb{T}_k$, with D_+ being the linear growth factor, Ω_m the matter density parameter, H_0 the Hubble constant and $\mathbb{T}(k)$ the transfer function. From the above equation we can see that the term that has the potential to significantly improve the bispectrum constraining power for f_{nl} is $T_{(1112)}$. This is because $T_{(1112)}$ has a similar functional form and k -dependence as the matter bispectrum PNG correction (equation E.29 in the appendix).

Figure 4 shows, for matter bispectrum and i-trispectrum in real space, the ratio between primordial and gravitational components for $f_{\text{nl}} = 1$ and $g_{\text{nl}} = 10^5$. For the bispectrum, as expected, the ratio is $\mathcal{O} \sim 10^{-3} - 10^{-4}$ depending on scale, for the i-trispectrum there are configurations where this ratio is larger and reaches $\mathcal{O} \sim 10^{-2}$. These are symmetric configurations of the i-trispectrum and the boost is driven by the sum of k -vectors appearing at the denominator of one of the two components of $T_{(1112)}$ reported in equation 2.26.

2.5 Fisher-based forecasts

Before developing all the required theoretical and technical tools necessary to employ a new statistics in the analysis of real survey data, there are mainly two ways to assess the additional information harvested by measuring this new statistics on a cosmological field. One method is to look at the general improvement of the full data-vector signal-to-noise (including both old and new statistics). The other, more specific, alternative is to forecast the improvements on the parameters of interest constraints obtained by employing the new statistics.

With the covariance matrix \mathbf{Cov} for a given data-vector in hand, we can define two quantities for these purposes. These are the cumulative signal-to-noise (S/N) and the Fisher information matrix (F); from the latter, both conditional and marginalised errors on the model parameters can be estimated.

The (expected) cumulative signal-to-noise as a function of the maximum k -value, given a (theoretical description of a) data-vector and the relative covariance matrix $\mathbf{Cov}_{\mathbf{d}}$, is computed as

$$(\text{S/N}) = \sqrt{\mathbf{d}_{\text{th}}^{\text{T}} \mathbf{Cov}_{\mathbf{d}}^{-1} \mathbf{d}_{\text{th}}}. \tag{2.27}$$

¹⁰The corresponding redshift space quantity for the matter field is simply obtained by replacing the matter case kernels $F^{(i)}$ with the redshift space ones $Z^{(i)}$ as done in appendix A for the purely gravitational terms $T_{(1122)}$ and $T_{(1113)}$.

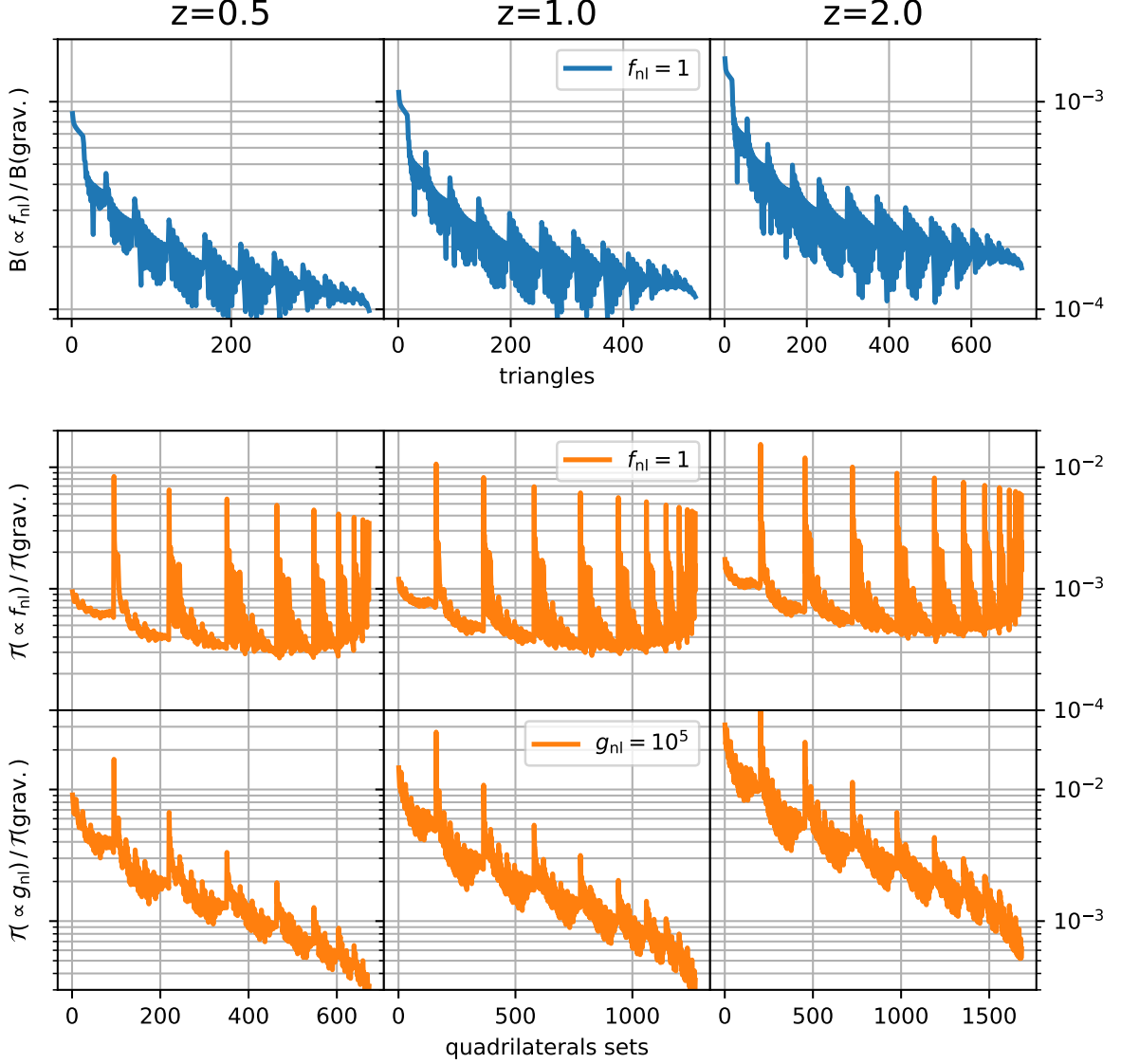


Figure 4. Primordial imprint on the matter bispectrum and i-trispectrum in real space. The first two rows from the top show the ratio between the primordial signal proportional to f_{nl} and the gravitational component for the bispectrum and i-trispectrum, for $f_{\text{nl}} = 1$. In the bottom row the i-trispectrum signal proportional to g_{nl} , also divided by the gravitational part, is displayed for $g_{\text{nl}} = 10^5$. The analytical expression for these terms is given in equation 2.26. In particular for the quadrilateral symmetric configurations, the integrals in the model of equation 2.6 have been checked to converge for $k_{\text{min}} \lesssim 10^{-4} h/\text{Mpc}$.

where the data-vectors \mathbf{d} should be interpreted as functions of k_{max} .

Given a theoretical model description of the data-vector, $\mathbf{d}_{\text{th}}(\theta_i)$, with dependence on model parameters θ_i , the Fisher information matrix is the Hessian matrix of the associated log likelihood, \mathcal{L} , with the derivatives taken with respect to the model parameters,

$$F_{ij} = - \left\langle \frac{\partial^2 \mathcal{L}}{\partial \theta_i \partial \theta_j} \right\rangle \Big|_{\theta_{\text{ml}}} \quad (2.28)$$

where θ_{ml} indicates that the derivatives are evaluated at the likelihood maximum.

In the case of a single-parameter estimate, the minimum achievable error is given by $\Delta\theta_{\text{min}}^i = 1/\sqrt{F_{ii}}$. In the general multi-parameter case, this is the conditional error as it assumes that all other parameters are perfectly known. To obtain the marginal error, in the multi-parameter case the inverse of the Fisher information matrix needs to be used $\Delta\theta_{\text{min}}^i = \sqrt{F_{ii}^{-1}}$ [94]. Using the data-vector's covariance matrix and its derivatives with respect to the model parameters, each element of the Fisher information matrix can be computed as

$$F_{ij} = \frac{\partial \mathbf{d}_{\text{th}}^\top}{\partial \theta_i} \mathbf{Cov}_{\mathbf{d}}^{-1} \frac{\partial \mathbf{d}_{\text{th}}}{\partial \theta_j} \quad (2.29)$$

since here (as in most Fisher forecasts and in most large-scale structure studies) we adopt a Gaussian likelihood with fixed covariance matrix (see e.g., [14, 49]).

In what follows we will make use of another related quantity: the cumulative χ^2 as a function of k_{max} . Given a measured data-vector \mathbf{d} and its theoretical model \mathbf{d}^{th} , the cumulative χ^2 can be computed using the full covariance matrix, χ_{Cov}^2 , or can be approximated (as often done in practice) by considering only the diagonal elements, $\chi_{\sigma^2}^2$. These expressions read,

$$\begin{aligned} \chi_{\text{Cov}}^2(k_{\text{max}}) &= (\mathbf{d}_{\text{th}}(k_{\text{max}}) - \langle \mathbf{d}(k_{\text{max}}) \rangle)^\top \mathbf{Cov}_{\mathbf{d}}^{-1}(k_{\text{max}}) (\mathbf{d}_{\text{th}}(k_{\text{max}}) - \langle \mathbf{d}(k_{\text{max}}) \rangle) \\ \chi_{\sigma^2}^2(k_{\text{max}}) &= \sum_{i|\forall d^i \in \mathbf{d}_{\text{th}}(k_{\text{max}})} \frac{(d_{\text{th}}^i(k_{\text{max}}) - \langle d^i(k_{\text{max}}) \rangle)^2}{\sigma_i^2(k_{\text{max}})} \quad \text{where,} \\ \sigma_i^2(k_{\text{max}}) &= \frac{1}{N_{\text{sim}} - 1} \sum_{\ell=1}^{N_{\text{sim}}} (d_\ell^i(k_{\text{max}}) - \langle d^i(k_{\text{max}}) \rangle)^2. \end{aligned} \quad (2.30)$$

$\mathbf{d}_{\text{th}}(k_{\text{max}})$, $\mathbf{d}(k_{\text{max}})$ is a shorthand for the data-vector with configurations limited by k_{max} (same for the covariance $\mathbf{Cov}_{\mathbf{d}}^{-1}(k_{\text{max}})$), while $\langle d^i(k_{\text{max}}) \rangle$ and $\sigma_i^2(k_{\text{max}})$ are the mean and the variance for the i -th mode (with i running over all the elements of the data-vector $\mathbf{d}(k_{\text{max}})$) estimated from the set of simulations. Here we assume (as often done) that the number of degrees of freedom, N_{dof} , corresponds to the length of the data-vector up to a certain k_{max} minus one. χ_{Cov}^2 includes the cross correlations among different elements of the data vector, $\chi_{\sigma^2}^2$, on the other hand, assumes the different data-vector elements to be uncorrelated and therefore uses only the variance. The χ^2 is popular because it offers a relatively quick, although often inaccurate, goodness of fit test.

Notice that while in our analysis we will adopt the mean of the measured data-vector as reference for the χ^2 -test, we will not use the error on the mean (which would be computed by dividing the variance in equation 2.30 by the number of realisations used), but the one relative to a single realisation. This is because deriving a dark matter statistics model which would be accurate enough to return a good χ^2 for an average over thousands of Gpc³ is beyond the scope of this work.

3 Results

3.1 Real space: measure vs. model

In this section we compare the measurements of the power spectrum, bispectrum and i-trispectrum estimators from the set of QUIJOTE simulations [101] to the respective theoretical models (section 2.1) for three different redshift snapshots: $z = \{0.5, 1, 2\}$. We also measure the i-trispectrum auto and cross (with power spectrum and bispectrum) covariance matrix, and compare its diagonal elements with an analytical model.

3.1.1 Analysis set-up

We use 5000 realisations of the N-body simulations from the QUIJOTE suite [101]. Given the length of our data vector we estimate that $N_{\text{sim}} = 5000$ offer an optimum balance between speed and computational resources and accuracy of the estimate of the covariance matrix and its inverse. The simulations follow the gravitational evolution of 512^3 dark matter particles, in a periodic cubic box with size $L = 1h^{-1}\text{Gpc}$. The initial conditions for the simulations were generated at $z = 127$ using 2LPT [20, 77, 87], and we concentrate on the snapshots at redshifts $z = 0.5, 1$ and 2 .

The underlying cosmology of the QUIJOTE simulations is a flat ΛCDM model (consistent with the latest CMB constraints [17]). Specifically, the matter and baryon density parameters are $\Omega_{\text{m}} = 0.3175$, $\Omega_{\text{b}} = 0.049$, and the dark energy equation of state parameter is $w = -1$; the reduced Hubble parameter is $h = 0.6711$, the late-time dark matter fluctuations amplitude parameter is $\sigma_8 = 0.834$, the scalar spectral index is $n_s = 0.9624$, and neutrinos are massless, i.e. $M_\nu = 0.0$ eV.

We discretise the box in 256^3 grid cells, and consider a bin size of $\Delta k = 2k_{\text{f}}$, where $k_{\text{f}} = 0.00625 h/\text{Mpc}$ is the fundamental frequency. Since non-linearities increase as the redshift decreases, perturbation theory, and hence our model, breaks down at different scales for different redshifts. In the following analysis the quadrilaterals sets sides for the i-trispectrum are limited to $k_{\text{max}}(z = 0.5) = 0.15 h/\text{Mpc}$, $k_{\text{max}}(z = 1) = 0.17 h/\text{Mpc}$ and $k_{\text{max}}(z = 2) = 0.19 h/\text{Mpc}$. For both power spectrum and bispectrum we display results for a k_{max} which is one third larger than the one for the i-trispectrum at each redshift (i.e. $k_{\text{max}}(z = 0.5) = 0.2 h/\text{Mpc}$, $k_{\text{max}}(z = 1) = 0.22 h/\text{Mpc}$ and $k_{\text{max}}(z = 2) = 0.25 h/\text{Mpc}$). In what follows, the triangles (for the bispectrum) and quadrilaterals sets (for the i-trispectrum) are ordered and labelled according to the convention illustrated in figure 3.

We assume a Poissonian shot-noise and we subtract it from the measured signal using the procedure described in appendix C. This consists in using measured quantities (such as power spectra and bispectra) to build the shot-noise corrections given in the literature e.g., [98].

3.1.2 Power spectrum and bispectrum

In figure 5 the mean and the standard deviation of the power spectrum measurements from the QUIJOTE simulations (orange solid lines) are compared to the theoretical model predictions. The adopted k -bin size is $\Delta k = 0.0126 h/\text{Mpc}$ and the *rms* is computed by the scatter among the 5000 realisations. Both linear theory (red dashed) and HALOFIT (blue dot-dashed) $P(k)$ predictions are shown. In the first row the power spectra are multiplied by a factor of $k^{\frac{3}{2}}$ and normalised by the linear growth factor squared at each snapshot's redshift, $D_+(z)^2$, also computed using CLASS. The next row shows the ratio between the theoretical models and the simulation measurement (simulation output in orange, HALOFIT in blue dot-dashed and

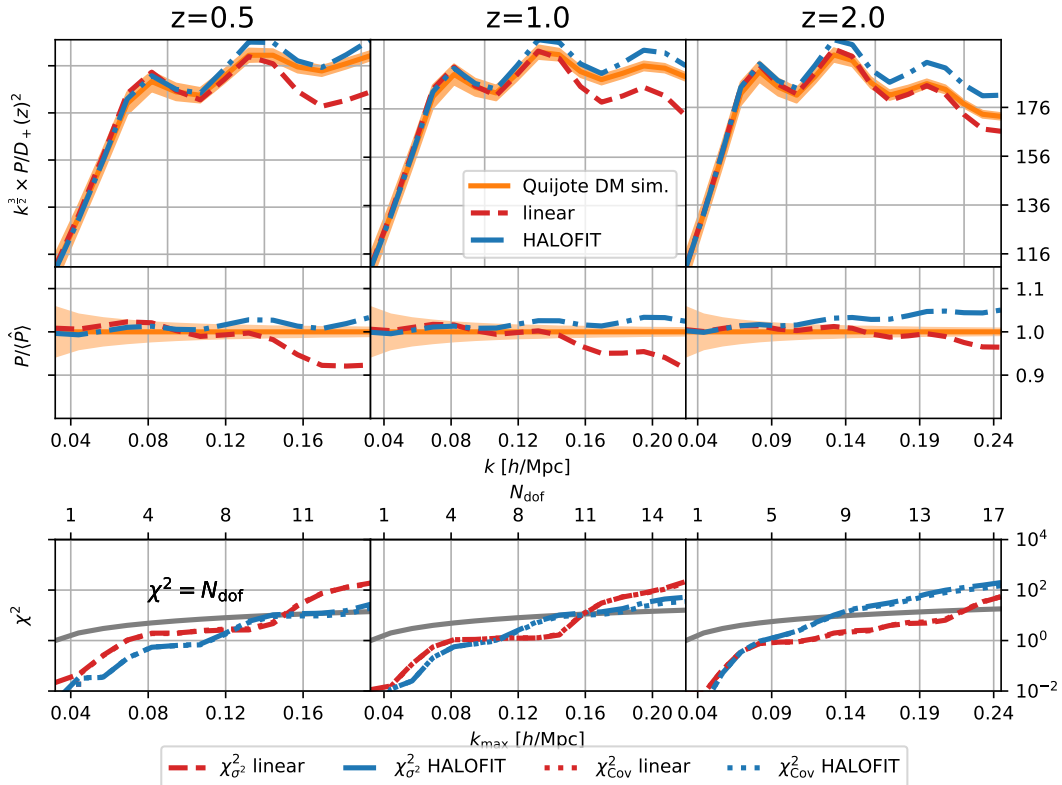


Figure 5. Matter power spectra (real space) measured from the QUIJOTE simulations at redshifts $z = 0.5, 1, 2$ compared with the theoretical models. The orange line is the power spectrum measured from the simulations, with the shaded orange area being the standard deviation estimated from a set of 5000 different realisations, while the red and blue lines are respectively the linear and HALOFIT power spectrum given by CLASS [59] using the same underlying cosmology of the simulations [101]. The top row shows the quantity $k^{3/2}P(k)D_+^{-2}(z)$ where D_+ denotes the linear growth rate. The second row shows the ratio of the power spectrum to the one measured from the simulation output. The orange shaded area indicate the simulations' standard deviation. On the lower part, the cumulative χ^2 using both linear and HALOFIT for \mathbf{d}_{th} , is plotted, along with the number of degrees of freedom (see text for more details). Dashed and dotted lines overlap because the covariance for the power spectrum at these scales is to a good approximation diagonal. Notice that the variances and covariances used for the χ^2 -tests are relative to a single realisation of 1 Gpc^3 volume.

linear theory prediction in red dashed). The third row shows the cumulative χ^2 computed as described in equation 2.30. It is possible to appreciate the redshift dependence of the k_{max} up to which the models fit the data well. While for $z = 0.5$ and 1 HALOFIT performs better than the linear power spectrum prediction, at $z = 2$ the opposite happens and the linear model has a good χ^2 up to $k \sim 0.20 h/\text{Mpc}$. This effect is understood as follows. In this range of scales at this redshift many k -modes are undergoing gravitational collapse simultaneously (for those k values such that $k^3P(k)/(2\pi)^3 \simeq 1$, which is the regime where structure formation is more complex to describe with halo-model/semi-analytic approaches. On the other hand, at later times, when the structure formation may be more nonlinear (and naively more difficult to model), the collapse happens in a more ordered way, and it is easier for HALOFIT to capture it. One should also recall that HALOFIT is designed to match the power spectrum shape up to $k \simeq 10 h/\text{Mpc}$, so it is not surprising that its description of the power spectrum is not too

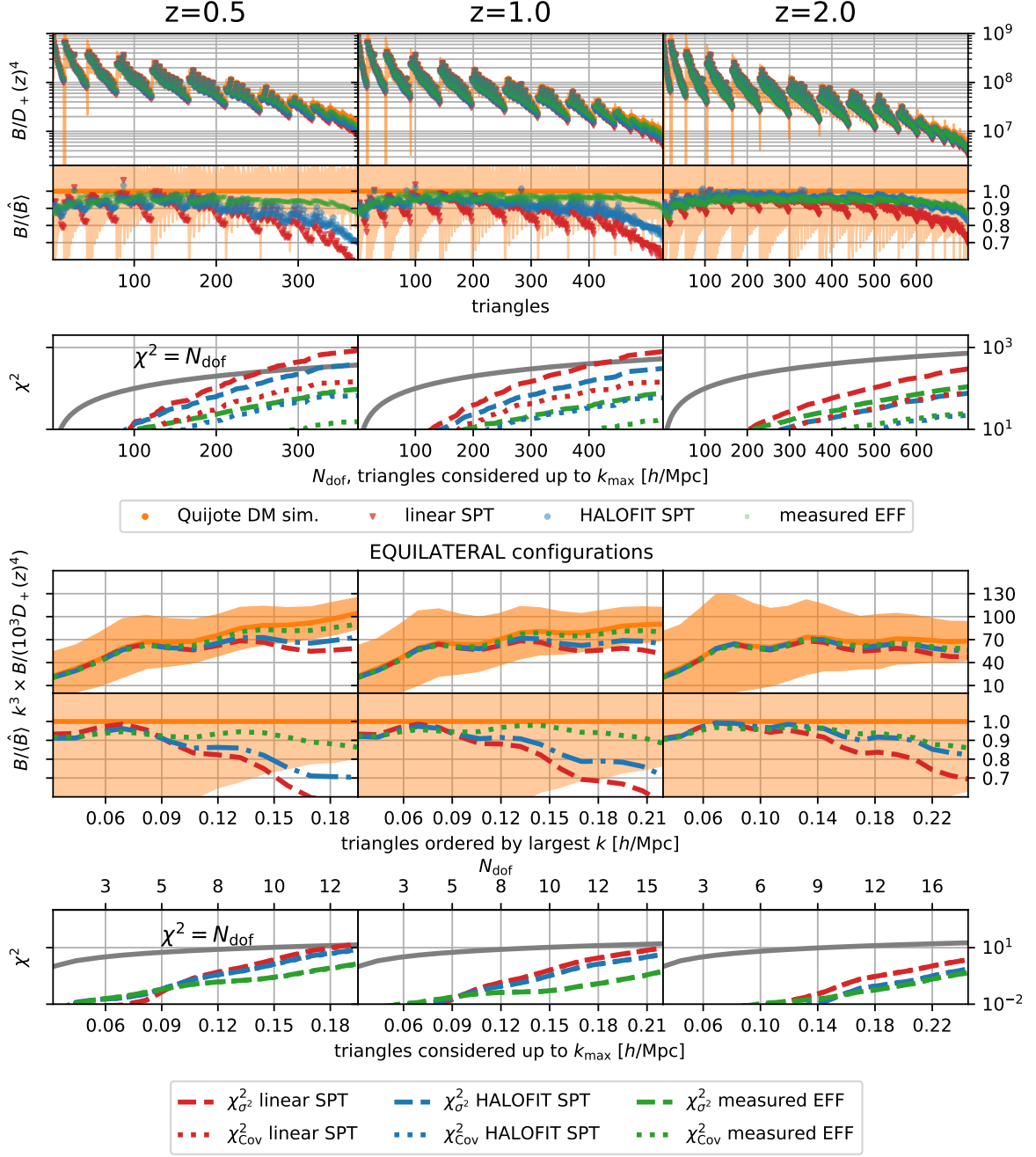


Figure 6. Same as figure 5 but for the bisppectrum. The top half of the plot shows all configurations and the bottom half shows only equilateral triangle configurations to make the dependence on scale easier to interpret. In addition to standard perturbation theory (SPT) prediction using linear (red) and HALOFIT (blue) power spectra as input, the green lines correspond to the B^{EFF} bisppectrum prediction using the effective kernels [31, 34] and for non-linear power spectrum the average of the simulations measurements. In both cases the cumulative χ^2 and the degrees of freedom curves are reported. The difference between $\chi_{\sigma^2}^2$ and χ_{Cov}^2 from equation 2.30 is visible only in the “all shapes” case (top half of the plot); equilateral configurations are only very weakly correlated.

accurate at relatively weakly non-linear scales.

The cumulative chi-square computed with $\chi_{\sigma_2}^2$ and χ_{Cov}^2 from equation 2.30 almost perfectly overlap: at these scales the power spectrum modes are not very correlated and the $P(k)$ covariance matrix is quasi-diagonal.

Figure 6 shows the same information for the bispectrum. In the top half of the plot all triangle configurations are shown, while the lower half displays only equilateral configurations in order to make the scale dependence easier to interpret.

In addition to the SPT models using the linear and HALOFIT power spectra as input (B_{SPT} and $B_{\text{SPT-NL}}$), we also present the comparison of the measurements with the effective model B_{EFF} (see equation 2.2 and Refs. [31, 34]). In this case we use the mean of the power spectrum measurements from the simulations as non-linear power spectrum input for the effective model ("measured EFF" in the figure). The SPT model with HALOFIT non-linear power spectrum always outperforms the standard SPT one (with linear power spectrum) and becomes closer to the effective bispectrum model as the redshift increases. At all redshifts, the effective bispectrum model significantly increases the maximum k at which the model fits the measurements. It is interesting to note how the B_{EFF} model, with the effective kernel calibrated for only specific shapes from N-body simulations, offers a better description than SPT for all triangle shapes.

The difference between the cumulative χ^2 assuming uncorrelated bispectrum modes and accounting for the full covariance, $\chi_{\sigma_2}^2$ and χ_{Cov}^2 (equation 2.30), is visible in the "all shapes" case (top half of the plot): different bispectrum modes (triangles) are in general correlated; equilateral configurations on the other hand are only very weakly correlated.

3.1.3 i-trispectrum

As described in section 2.2.1, in order to obtain the i-trispectrum signal, the unconnected part needs to be subtracted from the total signal measured using the estimator presented in equation 2.14. In figure 7 we compare the unconnected signal theory template $\mathcal{T}_u^{\text{th}}$, (equation 2.20) with the measurement performed using the estimator $\hat{\mathcal{T}}_u$ in equation 2.19. The unconnected part is approximately two orders of magnitude larger than the connected part (which is expected from standard perturbation theory, being the unconnected part a lower order term with respect than the connected one).

To avoid systematic errors due to limitations in the perturbation theory description of the unconnected part of the signal, we prefer to estimate the unconnected contribution using $\hat{\mathcal{T}}_u$ equation 2.19 instead of the analytical model. This is to be subtracted from the total signal $\hat{\mathcal{T}}_{\text{c+u}}$ to obtain the i-trispectrum $\hat{\mathcal{T}}_c$ according to equation 2.16. In the lower panel of figure 7 the ratio between the models for the i-trispectrum unconnected part using linear and HALOFIT matter power spectra can be seen to diverge from one as the size of the quadrilateral sides (k_1, k_2, k_3, k_4) increases, as expected from the breaking down of perturbation theory at non-linear scales (see figure 3 to visualise how the sides vary among configurations).

In figure 8 we show the comparison between the resulting measured i-trispectrum $\hat{\mathcal{T}}_c$, and the theoretical model, $\mathcal{T}_c^{\text{th}}$ defined in equations 2.4 and 2.6 (same conventions as for figure 6). For easier interpretation, in the lower part only equilateral configurations are shown.

The integrated theoretical model (equations 2.4 and 2.6), both for linear and HALOFIT power spectrum, performs reasonably well. When all the quadrilaterals sets are considered, the cumulative χ^2 closely follows the line for our adopted N_{dof} , number of degrees of freedom. Notice that the different quadrilaterals sets making up the i-trispectrum data-vector are correlated, as it can be inferred from the covariance matrix shown in figure 9, therefore the

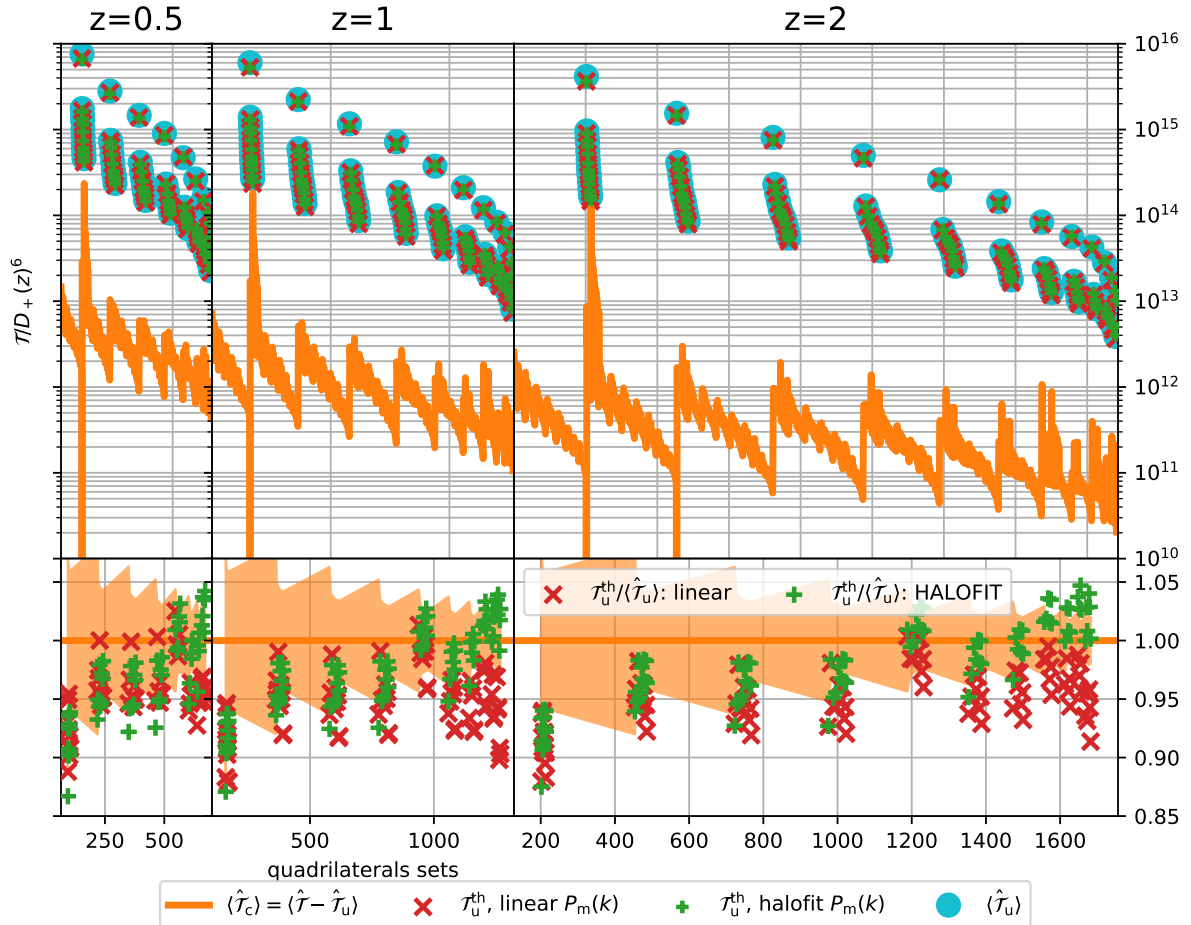


Figure 7. Connected ($\hat{\mathcal{T}}_c$) and unconnected ($\hat{\mathcal{T}}_u$) components of the total average four-point correlator signal $\hat{\mathcal{T}}_{c+u}$ measured from the 5000 dark matter simulations, using the estimator from equation 2.16 at redshifts $z = 0.5, 1, 2$. Since the k -range of interest varies with redshift (k_{\max} increases with z as the field is more linear) the number of configurations shown also depends on redshift (see text for details). The light-blue dots (with error bars too small to be visible in this plot) correspond to the unconnected term $\hat{\mathcal{T}}_u$ measured from the simulations using the estimator described in equation 2.19. The green (+) and red (×) signs represent the theory prediction for the unconnected signal (equation 2.20) computed respectively using linear and HALOFIT matter power spectra. The orange line corresponds to the mean of 5000 measurements of the total signal minus the unconnected part estimated also from 5000 measurements (equation 2.18), the orange shaded area indicates the standard deviation (scatter among the 5000 simulations) for each mode. \mathcal{T}_u is about two orders of magnitude larger than \mathcal{T}_c : in fact the unconnected part is of order $\propto \delta^4$ while the connected one is $\propto \delta^6$. The fact that for both linear and HALOFIT versions the ratio between model and estimated unconnected part oscillates by approximately $\sim 10\%$ justifies the choice of subtracting the measured unconnected term from the total signal estimated by the four-point correlator (equation 2.16).

effective number of degrees of freedom is effectively lower than the number of configurations used.

An improvement in the fit could be obtained by extending the effective model of the kernels to the third-order ones needed to compute the i-trispectrum. At the same time the second order kernels could be fitted using both bispectrum and i-trispectrum. We leave this to future work.

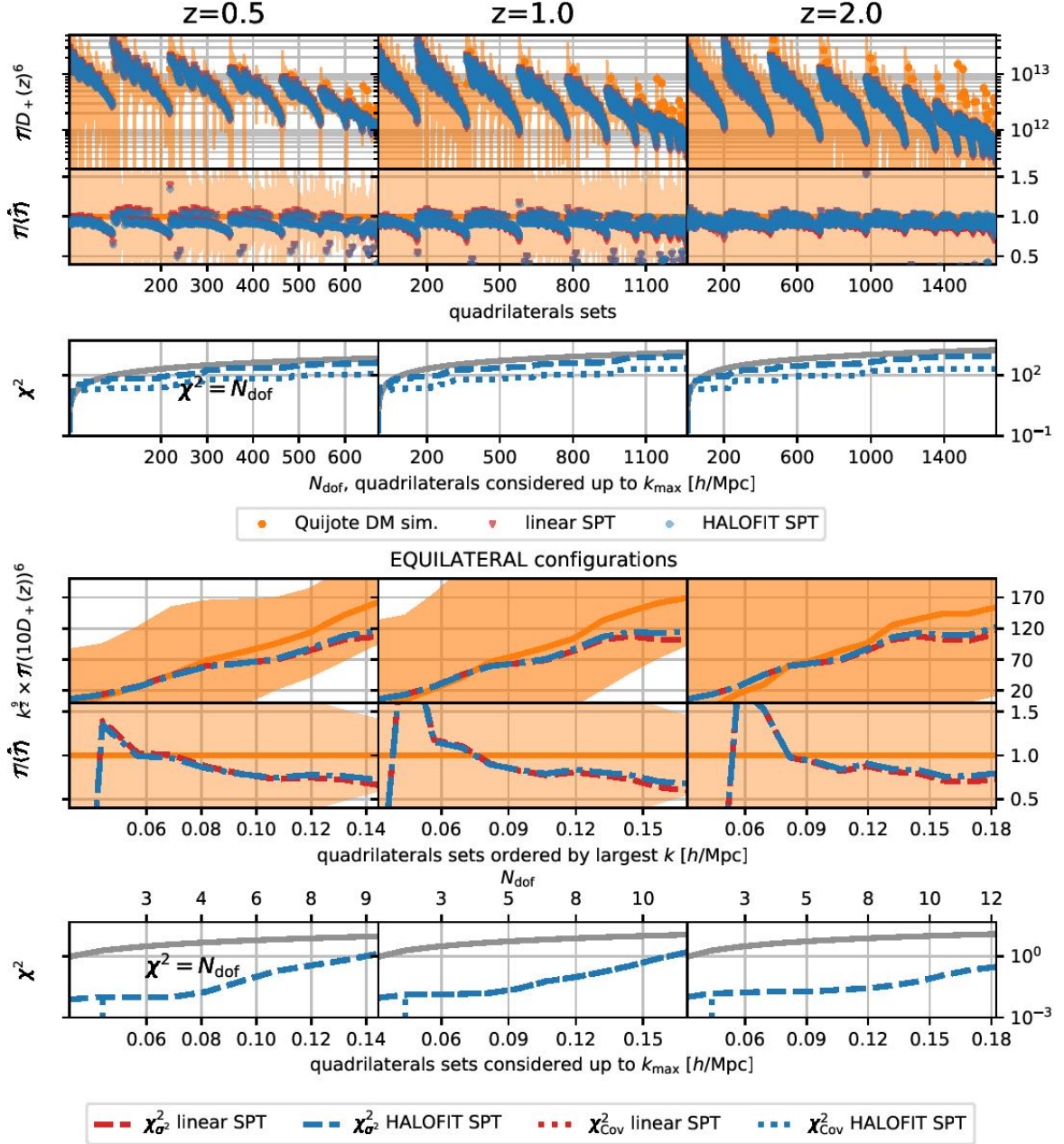


Figure 8. Same as figures 5 and 6 but for the i-trispectrum. The theoretical model $\mathcal{T}_c^{\text{th}}$ recovers the mean of the measurements $\langle \hat{\mathcal{T}}_c \rangle$ well within the estimated variance. The cumulative χ^2 , by closely following the number of degrees of freedom's curve, confirms the good match between theory and measurements at all the considered redshifts ($z = 0.5, 1, 2$) up to each respective smallest scale considered $k_{\text{max}} = 0.15, 0.17, 0.19 h/\text{Mpc}$. Similarly to the bispectrum in figure 6, the difference between $\chi_{\sigma^2}^2$ and χ_{Cov}^2 from equation 2.30 is significant only when all the possible quadrilaterals sets are considered (equilateral configurations appear to be significantly less correlated than generic ones and that is the reason why the different χ^2 -lines almost perfectly overlap).

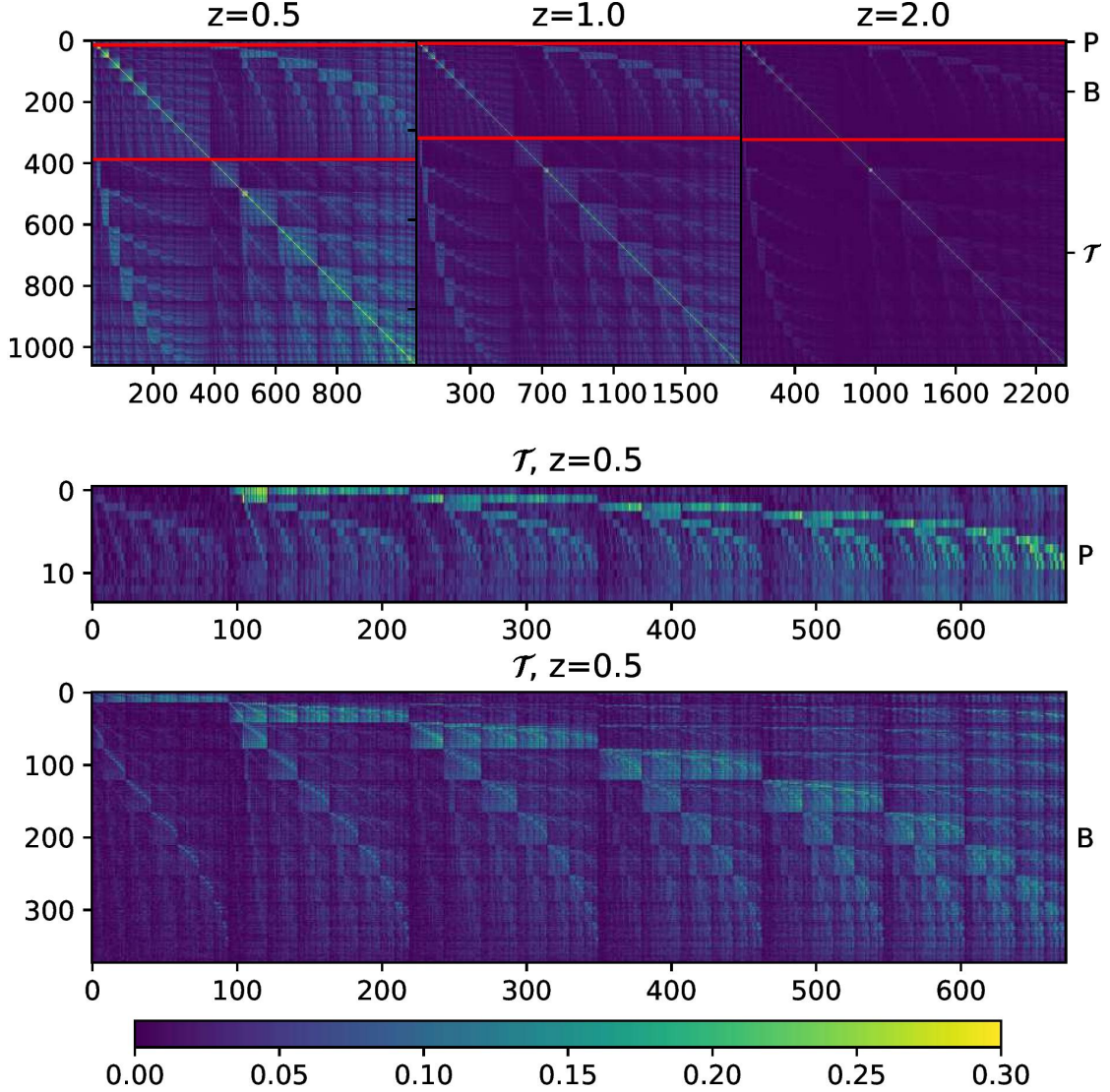


Figure 9. Reduced covariance matrix, $r_{ij} = \text{Cov}_d^{ij} / \sqrt{\text{Cov}_d^{ii} \text{Cov}_d^{jj}}$, estimated from the set of 5000 simulations at each redshift. In the top row the joint PBT covariance matrices are displayed while the central and bottom rows show a zoom-in of the cross correlation between i-trispectrum and power spectrum / bispectrum at $z = 0.5$. The ordering of configurations is the same as seen in figures 6 and 8. From left to right the different columns show the results for $z = 0.5, 1, 2$ with $k_{\text{max}} = 0.15, 0.17, 0.19 h/\text{Mpc}$, respectively. The horizontal red lines guide the eye to recognise the covariance parts corresponding to power spectrum, bispectrum and i-trispectrum. The covariance matrices acquire more structure as z decreases, which is a sign of non-linear growth and stronger mode coupling among different configurations/data-vector's elements. Especially for low redshifts ($z = 0.5, 1$), the above plots show that both the correlation between different modes of the same statistics and cross-correlation between modes of different statistics are not negligible and reach up to $\sim 30\%$ the value of the diagonal elements. A Fisher forecast using a theoretically computed diagonal covariance matrix under the Gaussian approximation (as it is often done in the literature) would in this case produce too optimistic constraints by underestimating the redundancy in the data-vector due to correlation among different elements.

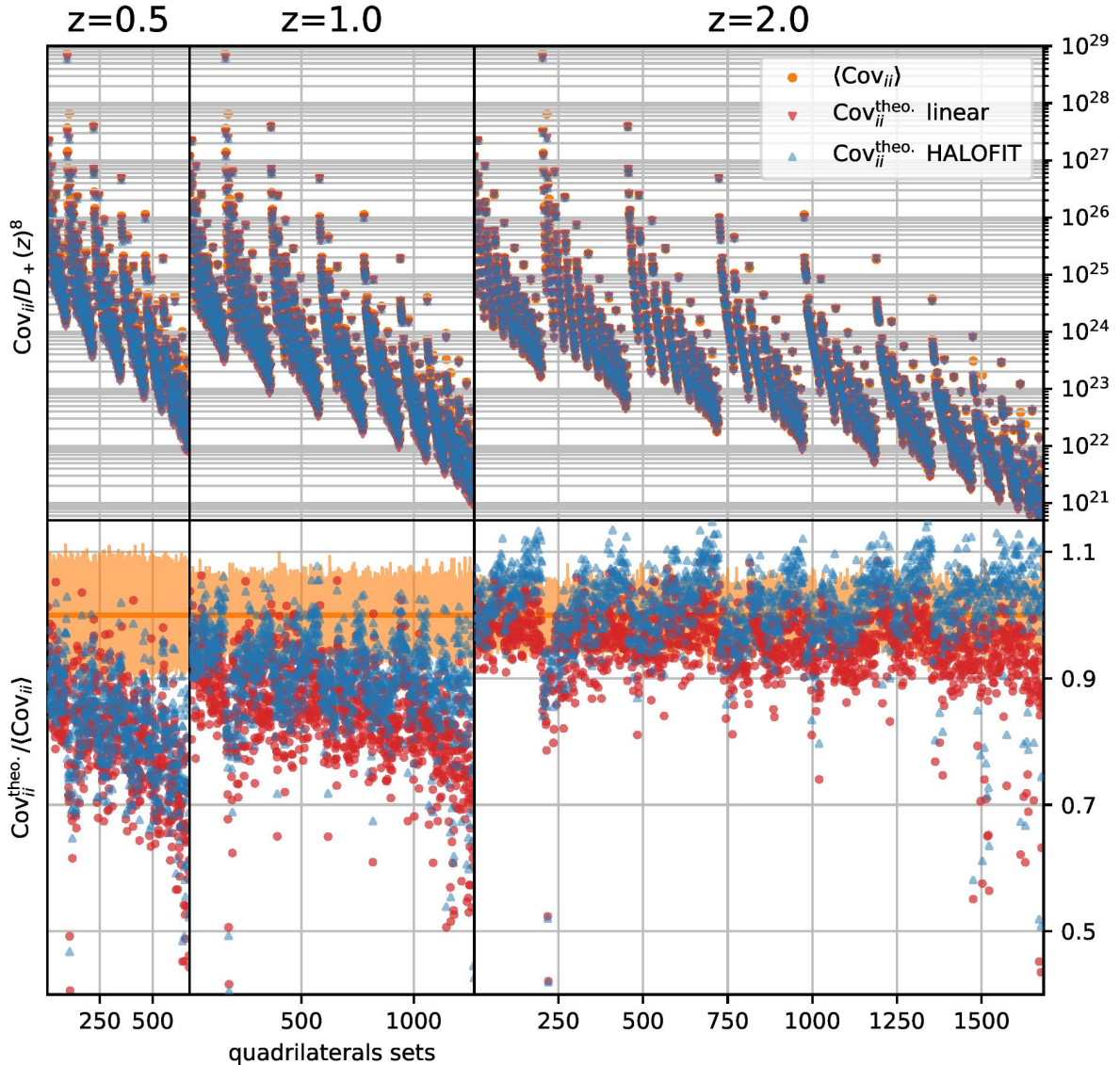


Figure 10. Comparison between the diagonal elements of the numerically-estimated i-trispectrum covariance matrix and the theoretical model (only Gaussian term) of equation 2.23. The model is shown for both the linear (red) and HALOFIT (blue) power spectrum. The orange shaded area is the *rms* estimated by jackknife i.e. standard deviation for the diagonal elements obtained by splitting the 5000 simulations into $(16_{z=0.5}, 9_{z=1}, 7_{z=2})$ equally populated subsets and then by estimating the covariance matrix diagonal for each subset. From the different estimates it was then possible to derive a standard deviation for each covariance matrix diagonal element. In agreement with what is observed in figure 9, the Gaussian approximation for the covariance diagonal becomes increasingly better as the redshift increases. Together with figure 9, this highlights the importance of using the numerically-estimated covariance matrix and not a Gaussian approximation for redshifts lower than $z = 2$. Using only the Gaussian term would indeed significantly underestimate both the correlation between different data-vector's elements (figure 9) and the non-linearly induced auto-correlation of each element with itself.

3.1.4 Covariance matrix and Gaussian term analytical model

The covariance matrix of the i-trispectrum and that of the full power spectrum, bispectrum and i-trispectrum data vector (PBT for short), are fundamental ingredients for assessing the

impact of adding this four-point statistic to a parameter constraints analysis. Usually in this kind of forecasts studies, an analytical template is used and often the covariance is assumed to be diagonal with only a Gaussian component, together with assuming zero cross-correlation between different n -point statistics.

In this section we show that following the above assumption in the case of the i-trispectrum would induce a significant bias leading to an overestimate of the i-trispectrum constraining power when added to the power spectrum and bispectrum data-vector. To this purpose, we numerically estimate the $\text{PB}\mathcal{T}$ covariance matrix from the simulations as described in section 2.3. The k_{max} at each redshift for each statistics are the same as described in section 3.1.1.

Figure 9 shows the reduced covariance matrix, $r_{ij} = \text{Cov}_{\mathbf{d}}^{ij} / \sqrt{\text{Cov}_{\mathbf{d}}^{ii} \text{Cov}_{\mathbf{d}}^{jj}}$, numerically evaluated from the 5000 simulations. The top row shows the full ($\text{PB}\mathcal{T}$) covariance (to guide the eye, the red lines indicate the P, B and \mathcal{T} sections). In the central and bottom rows of figure 9 the cross-correlations of the i-trispectrum with both power spectrum and bispectrum are displayed at $z = 0.5$. As the redshift increases it is evident how the different elements of the joint data-vector become less and less correlated since the field is more linear and the mode-mixing induced by gravitational collapse is less important. At redshift $z = 0.5$ for the i-trispectrum, the off-diagonal elements of the reduced covariance become up to ~ 0.3 . This means that two different configurations can be cross-correlated as much as one third of their auto-correlation value. In other words, the level of redundancy in the data-vector increases as the redshift decreases.

Note also that the cross-correlations between power spectra of k -modes and bispectra of triangle configurations with the i-trispectra of quadrilaterals sets (up to the i-trispectrum k_{max}) are non-negligible at low redshifts.

A quantitative idea of the importance of the non-Gaussian contributions appearing in the i-trispectrum covariance matrix can be obtained by comparing the analytical model of the diagonal Gaussian term of equation 2.23 with the one estimated numerically. This is shown in figure 10: the difference increases as the redshift decreases. The shaded area is obtained by estimating the scatter of the covariance diagonal elements as follows. We take measurements from $N_{\text{G}}(z) = (16_{z=0.5}, 9_{z=1}, 7_{z=2})$ groups of simulations boxes randomly selected from the whole set of 5000 realisations. The $N_{\text{G}}(z)$ is set by requiring that the number of simulation boxes per group (i.e. $5000/N_{\text{G}}(z)$) is no smaller than half of the data-vector dimension. Note that the number of realisations used to estimate the covariance can safely be lower than the respective data-vector's dimension since we are just interested in deriving the diagonal elements, without inverting the covariance [42]. This confirms what is seen in figure 9, that for the i-trispectrum data-vector the non-Gaussian terms in the covariance are not negligible, in particular at lower redshifts.

The visible difference between $\chi_{\sigma^2}^2$ and χ_{Cov}^2 (equation 2.30) in figure 8 when all the configurations are considered further supports the importance of going beyond the Gaussian diagonal covariance approximation for the i-trispectrum (and also previously in figure 6 for the bispectrum) also for evaluating the goodness of fit of a theoretical model.

3.2 Primordial non-Gaussianity constraints: forecasts

For local primordial non-Gaussianity, a first assessment of the additional constraining power given by the i-trispectrum can be made via a Fisher-based forecast, considering the real space matter field. Promising results in this idealised case can motivate a more realistic analysis (e.g., for biased discrete tracers, in redshift space).

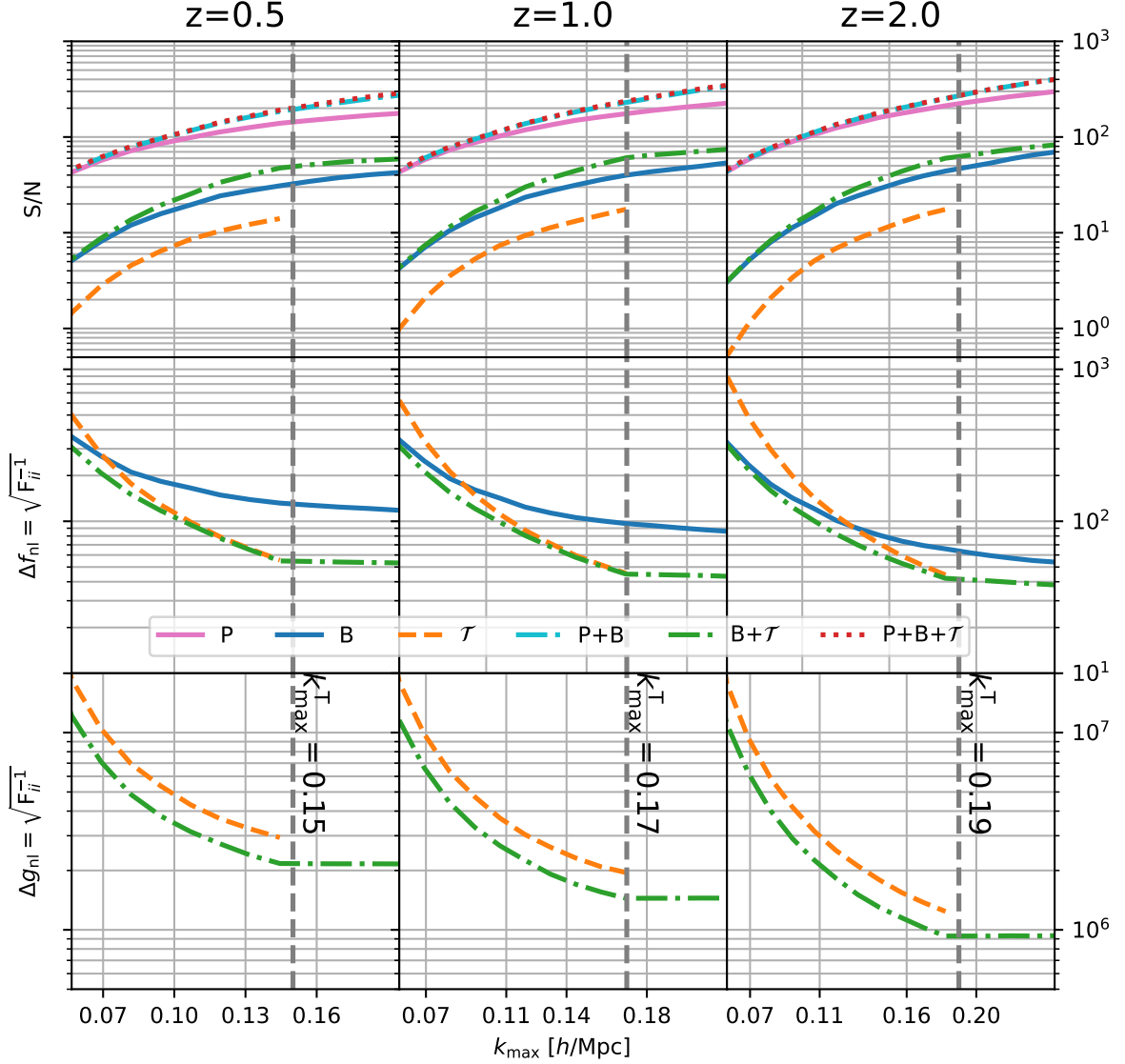


Figure 11. Signal-to-noise ratio and primordial non-Gaussianity constraints forecasts. The cumulative signal-to-noise ratio computed using equation 2.27 is displayed on the top row for the following statistics combinations: power spectrum (pink), bispectrum (blue), i-trispectrum (orange), power spectrum plus bispectrum (cyan), bispectrum plus i-trispectrum (green), power spectrum plus bispectrum plus i-trispectrum (red). In the second and third rows the forecasts for the constraints (equation 2.29) on the primordial non-Gaussianity parameters f_{nl} and g_{nl} are shown as a function of the maximum k -values considered. The dashed vertical lines indicate the i-trispectrum $k_{\text{max}}^{\text{T}}$, beyond which no additional quadrilaterals sets configurations are added to the joint data-vector as k_{max} increases. Even if adding the i-trispectrum to the joint power spectrum and bispectrum data-vector does not produce a significant change in terms of cumulative signal-to-noise, the benefits are evident when looking at the forecast for the constraints on the primordial non-Gaussianity parameters f_{nl} and g_{nl} .

Moreover, in this conservative scenario, we only consider conditional errors on the non-Gaussianity parameters, i.e., assuming all other parameters are fixed. If these were let free to vary, we expect the improvements on the constraints given by the i-trispectrum to be larger due to the reduction of the degeneracies present in the parameters space. This expectation is

motivated by the analogy with the findings of [3, 16, 40, 81, 103] obtained when adding the bispectrum to the power spectrum constraining power.

In particular for the forecasted constraints on f_{nl} and g_{nl} , when considering only the bispectrum we report $\Delta f_{\text{nl}}^{\text{min}} = 1/\sqrt{F_{f_{\text{nl}}f_{\text{nl}}}}$ while for the i-trispectrum and bispectrum plus i-trispectrum we use $\Delta f_{\text{nl}}^{\text{min}} = \sqrt{F_{f_{\text{nl}}f_{\text{nl}}}^{-1}}$ and $\Delta g_{\text{nl}}^{\text{min}} = \sqrt{F_{g_{\text{nl}}g_{\text{nl}}}^{-1}}$ (i.e., we report the error on a non-Gaussianity parameter marginalised over the other one accounting for the covariance between g_{nl} and f_{nl}).

In figure 11 we show both cumulative signal-to-noise ratio (equation 2.27) and Fisher forecasts (equation 2.29) for the constraints on f_{nl} and g_{nl} as a function of k_{max} for each of the redshifts considered in the analysis. The colours/line-styles are as follows: power spectrum only in magenta, bispectrum in blue, i-trispectrum in orange (dashed), joint power spectrum and bispectrum in cyan (dashed), joint bispectrum and i-trispectrum in green (dot-dashed) and full PBT in red (dotted). In the cumulative signal-to-noise (top row) plots one can appreciate the increase in signal generated by adding the i-trispectrum to the bispectrum, especially in the mildly non-linear regime (as k increases). Because of the logarithmic scale, it is difficult to notice the improvement when also the power spectrum is considered. The relative magnitude of the i-trispectrum effect when added to the bispectrum is similar to that observed when adding the bispectrum to the power spectrum.

Similarly, the middle row of figure 11 shows the substantial improvement obtained by using the i-trispectrum together with the bispectrum in order to constrain f_{nl} . We assumed in this work that the power spectrum sensitivity to and constraining power for primordial non-Gaussianity is negligible compared to bispectrum and i-trispectrum. This is because we are considering the dark matter particles as tracers. When moving to haloes this is no longer a reasonable approximation since PNG leaves a distinctive signature in the halo power spectrum through the scale dependent bias [21, 62]. Moreover the inclusion of the power spectrum would be fundamental for constraining additional cosmological or nuisance parameters, which in this analysis have been kept fixed.

Note, perhaps not unexpectedly [98], that in the very mildly non-linear regime ($k > 0.1 h/\text{Mpc}$ at $z = 0.5$) virtually all the constraining power for f_{nl} comes from the i-trispectrum. Even if the bispectrum is not sensitive at the considered order in perturbation theory ($\propto \delta^4$ for the bispectrum) to g_{nl} , when used together with the i-trispectrum it helps in reducing the degeneracy present in $T_{(1111)}$ between the two terms proportional to f_{nl}^2 and g_{nl} (see bottom row of figure 11).

The vertical dashed lines in figure 11 mark the maximum k -value used to build the quadrilaterals sets for the i-trispectrum. We considered larger k -values for power spectrum and bispectrum in order to show that even if the i-trispectrum would be employed up to a lower k_{max} (similarly to what happens between power spectrum and bispectrum), its effect is still significant.

Finally in table 1 we summarise these findings. The table reports values for the forecasted 1D 68% confidence interval regions for both f_{nl} and g_{nl} . Especially at lower redshifts, adding the i-trispectrum produces constraints on f_{nl} that are two times tighter than the ones produced by the bispectrum alone.

The results displayed in figure 11 and table 1 are encouraging for the prospect of large scale structures surveys, such as DESI [60], which are expected to produce constraints on local primordial non-Gaussianity parameters which will be competitive and complementary to the ones obtained up now by CMB experiments such as *Planck* [4]. While certainly encouraging,

| $k_{\max} [h/\text{Mpc}] \rightarrow$ | | 0.12 | | | 0.15 | | | 0.17 | | | 0.19 | | |
|---|-------------------|-----------------|-----------|-----------|-----------------|-----------|-----------|-----------------|-----------|-----------|-----------------|-----------|-----------|
| | d | $z = 0.5, 1, 2$ | | | $z = 0.5, 1, 2$ | | | $z = 0.5, 1, 2$ | | | $z = 0.5, 1, 2$ | | |
| Δf_{nl} | B | 149 | 124 | 102 | 132 | 106 | 81 | 124 | 98 | 69 | 121 | 94 | 66 |
| | \mathcal{T} | 80 | 87 | 109 | 56 | 60 | 71 | - | 44 | 51 | - | - | 44 |
| | $B + \mathcal{T}$ | 78 | 81 | 83 | 55 | 58 | 60 | 54 | 45 | 47 | 53 | 45 | 42 |
| $1 - \frac{\Delta f_{\text{nl}}^{B+\mathcal{T}}}{\Delta f_{\text{nl}}^B}$ | [%] | 48 | 35 | 19 | 58 | 45 | 26 | 56 | 53 | 32 | 56 | 52 | 36 |
| Δg_{nl} ($\times 10^{-4}$) | \mathcal{T} | 368 | 304 | 252 | 296 | 231 | 179 | - | 195 | 138 | - | - | 124 |
| | $B + \mathcal{T}$ | 273 | 225 | 183 | 219 | 174 | 130 | 218 | 145 | 103 | 218 | 144 | 93 |
| $1 - \frac{\Delta g_{\text{nl}}^{B+\mathcal{T}}}{\Delta g_{\text{nl}}^{\mathcal{T}}}$ | [%] | 14 | 12 | 11 | 19 | 17 | 16 | - | 20 | 16 | - | - | 17 |

Table 1. 1D 68% forecasted credible regions for both f_{nl} and g_{nl} as a function of k_{\max} for the bispectrum, i-trispectrum and bispectrum plus i-trispectrum in real space. The highlighted numbers correspond to the improvement on the parameters constraints given by employing both bispectrum and i-trispectrum, with respect to using only the bispectrum. All the values have been obtained through a Fisher forecast where the covariance matrix has been estimated from 5000 measurements on simulations and its inverse corrected by the corresponding Hartlap factor [42]. Each simulation's volume is $1 [\text{Gpc}/h]^3$.

it would be naive to conclude that these findings translate not just qualitatively but also quantitatively to realistic surveys. Real world issues such as survey geometry, galaxy bias and redshift space distortions may affect the above conclusions. In what follows, we present a first step towards more realistic estimates.

3.3 Redshift space

While the real space analysis presented so far indicates that in principle there is additional, useful information in the i-trispectrum, realistic observations are affected by redshift space distortions. To assess whether the real space results also hold in redshift space, in this section we present the same analysis performed on the redshift space matter density field. For this purpose, for each statistics we limit ourselves to the monopole signal only. Of course, there is potentially a lot of additional information enclosed in redshift space multipoles, but this will be presented elsewhere.

The theoretical modelling for the quantities in redshift space is presented in appendix A. Notice that, as normally done for power spectrum and bispectrum, in redshift space T^s is corrected by a term D_{FoG}^T modelling the Fingers-of-God effect (hereafter FoG) [44] (see appendix A).

We choose to focus on the redshift $z = 0.5$ case, which as it can be seen from figures 5,

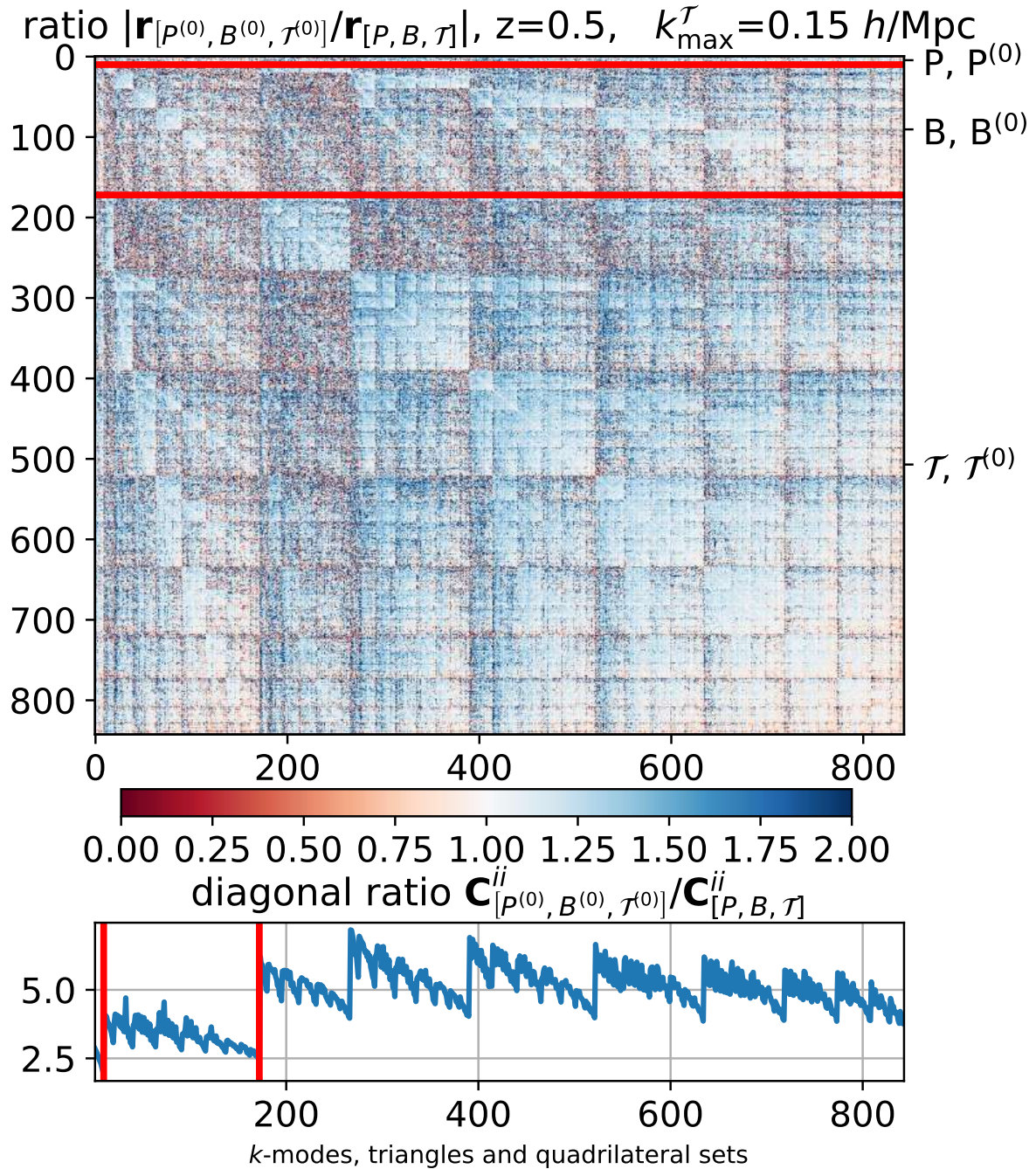


Figure 12. Absolute value of the ratio between the reduced covariance matrices for the data-vector measured in both real and redshift space for the $z = 0.5$ case. The absolute value helps with noticing how the off-diagonal cross-correlation between different data-vector elements increases when the measurement is performed in redshift space. This seems to be relevant especially for the configurations relative to the largest scales considered (top left corner of each auto-covariance matrix, see figure 3 for better visualising the ordering of the configurations for bispectrum and i-trispectrum as a function of the scale). Indeed for the bispectrum, for which $k_{\max}^B = 1.3 \times k_{\max}^{\mathcal{T}}$, the bottom corner of the auto-covariance shows the opposite effect, a reduction of the cross-correlation between different triangles having sides with the largest k -values (smallest scales).

6 and 8, is the case where the modelling is most severely tested: the field is more non-linear and smaller error bars are derived from the measurements on simulations (compared to the $z = 1, 2$ cases).

We begin by comparing the covariance matrix for the full data-vector in redshift space to the real space one. The overall structure of the redshift space matrix is very similar to that shown in the top panel of figure 9, however in details, the redshift space covariance shows more coupling between different data-vector elements. To better appreciate this, figure 12 shows the absolute value of the ratio (redshift to real space) of the elements of the reduced covariance matrices at $z = 0.5$. The off-diagonal cross-correlation between different data-vectors elements increases when the measurement is performed in redshift space, especially at the largest scales (top left region of each auto-covariance block). For the small-scales bispectrum on the other hand, the smallest scales (bottom right region of the relevant blocks) show a reduction of the cross-correlation.

We attribute this effect to two factors. First the k_{\max} for the bispectrum is higher than for the i-trispectrum, therefore proportionally more modes are affected by FoG effect and in the stable-clustering regime. Secondly the i-trispectrum, as it was described in section 2.1.1, is by definition an integrated quantity over many different quadrilateral shapes and hence it shows increased correlations.

Before we can proceed to show the comparison between simulation output and theoretical modelling for the data-vector, we recall that the parameters describing the small-scales FoG damping are ultimately phenomenological parameters that must be directly fit or calibrated on N-body simulations (and possibly marginalised over).

We use a χ^2_{Cov} minimisation (equation 2.30) to find the values for the small-scales fingers-of-God parameters σ_P , σ_B and σ_T (equations A.4 and A.5). This is illustrated in figure 15 in appendix A. In what follows, we adopt the values of σ_P , σ_B and σ_T that minimise the respective χ^2_{Cov} . These FoG parameters are kept fixed in the Fisher forecast analysis.

Figures 5 and 6 have shown that in real space at $z = 0.5$ the HALOFIT matter power spectrum model perform better than the linear one, also as input for the bispectrum model. Therefore for all the results presented in this section we use the HALOFIT matter power spectrum as input for computing the theoretical models. In order to obtain the best possible fit, we employ the redshift space version of the effective kernel $Z^{(2)}$ [34] for both bispectrum and i-trispectrum models (equation A.1).

Figure 13 is the redshift space monopole equivalent of the $z = 0.5$ panels of figures 5, 6 and 8. Together with the lines showing the models for the power spectrum, bispectrum and i-trispectrum models computed using the FoG parameters best-fit values, the models without FoG correction are also shown. As expected, the FoG term becomes more important as k increases and hence in particular for power spectrum and bispectrum whose k_{\max} is larger than the i-trispectrum one. In the i-trispectrum case, the FoG correction helps in stabilising the ratio between model and mean of the measurements around unity for all the considered quadrilaterals sets.

The forecasted constraints for primordial non-Gaussianity parameters and their improvement when adding the i-trispectrum to the bispectrum are shown in figure 14 and reported in table 2. In the left side of figure 14 the ratio between primordial non-Gaussianity and gravitational components for both bispectrum and i-trispectrum is displayed in the redshift space case (dashed lines) and for comparison also in real space (solid line, half transparent identical colours).

Clearly the measurement in redshift space suppresses the strength of the primordial non-

Gaussian component of the signal with respect to the gravitational one. This effect appears to be stronger in the i-trispectrum than for the bispectrum.

This can be understood as follows. The redshift-space distortions on large scales are gravity-driven and give a larger boost to the gravitational signal than to the PNG signal; an effect we refer to as Kaiser-boost effect. This can be easily appreciated in the left column of figure 11 where the change from real to redshift space is shown by using for the same colour both a lighter and a darker tone, respectively. Being a higher order statistic, the Kaiser-boost is naturally larger for the trispectrum than for the bispectrum as it is highlighted by the larger shift in the ratio between primordial and gravitational components. To further visualize this, in figure 17 of appendix E we focus on the Kaiser boost for equilateral configurations for both B and \mathcal{T} . Because of cosmic variance, this boost also increases the errors (via the covariance matrix).

In the top-right corner of the cumulative signal-to-noise plot, the reduction in the ratio (S/N) is evident only for the i-trispectrum alone before the $k_{\max}^{\mathcal{T}}(z = 0.5) = 0.15 h/\text{Mpc}$ threshold. For the bispectrum something similar happens at smaller scales, around $k_{\max} \sim 0.18 h/\text{Mpc}$.

Finally the bottom right corner showing the forecasted constraints on both f_{nl} and g_{nl} , for the different statistics combinations, connects all the elements appearing in the previous results of this section regarding the measurement, modelling and forecasts in redshift space. The increased cross-correlation between different quadrilaterals sets, highlighted by the ratio between redshift and real space covariance matrices in figure 12, together with the decrease for the i-trispectrum of both the relevance of the primordial term with respect to the gravitational one and of the cumulative signal-to-noise ratio, result in a smaller impact in redshift space of the i-trispectrum in improving the constraints on both f_{nl} and g_{nl} with respect to the bispectrum alone. This is quantitatively described in table 2.

Nevertheless the improvements are still significant, reaching for f_{nl} a $\sim 32\%$ reduction of the 68% 1D confidence interval when both bispectrum and i-trispectrum are employed in the analysis. The improvement for f_{nl} become larger as $k_{\max}^{\mathcal{T}}$ increases. This implies that improving the modelling of the signal to extend the k -range to include smaller scales could return even tighter constraints on f_{nl} .

4 Conclusions

In this work we have undertaken the first step towards employing the four-point correlation function's Fourier transform, the trispectrum, in cosmological analyses of current and future galaxy clustering data-sets.

The major challenge associated to the trispectrum is its high-dimensionality: six degrees of freedom are necessary to describe a skew-quadrilateral (eight in redshift space); this makes the trispectrum algorithmically and numerically prohibitive.

We propose here to overcome this difficulty by using a compressed version of the trispectrum signal, which we refer to as the i-trispectrum. The i-trispectrum integrates the signal over all the skew-quadrilaterals defined by a set of four k -modes moduli (k_1, k_2, k_3, k_4). As such, the i-trispectrum provides a solution to the trispectrum challenge by reducing the number of degrees of freedom down to four.

For the first time we model and measure the i-trispectrum both in real and redshift space. We present the i-trispectrum estimator (equation 2.16) which we then use to measure the signal from the QUIJOTE simulations suite at different redshifts, and compare it with

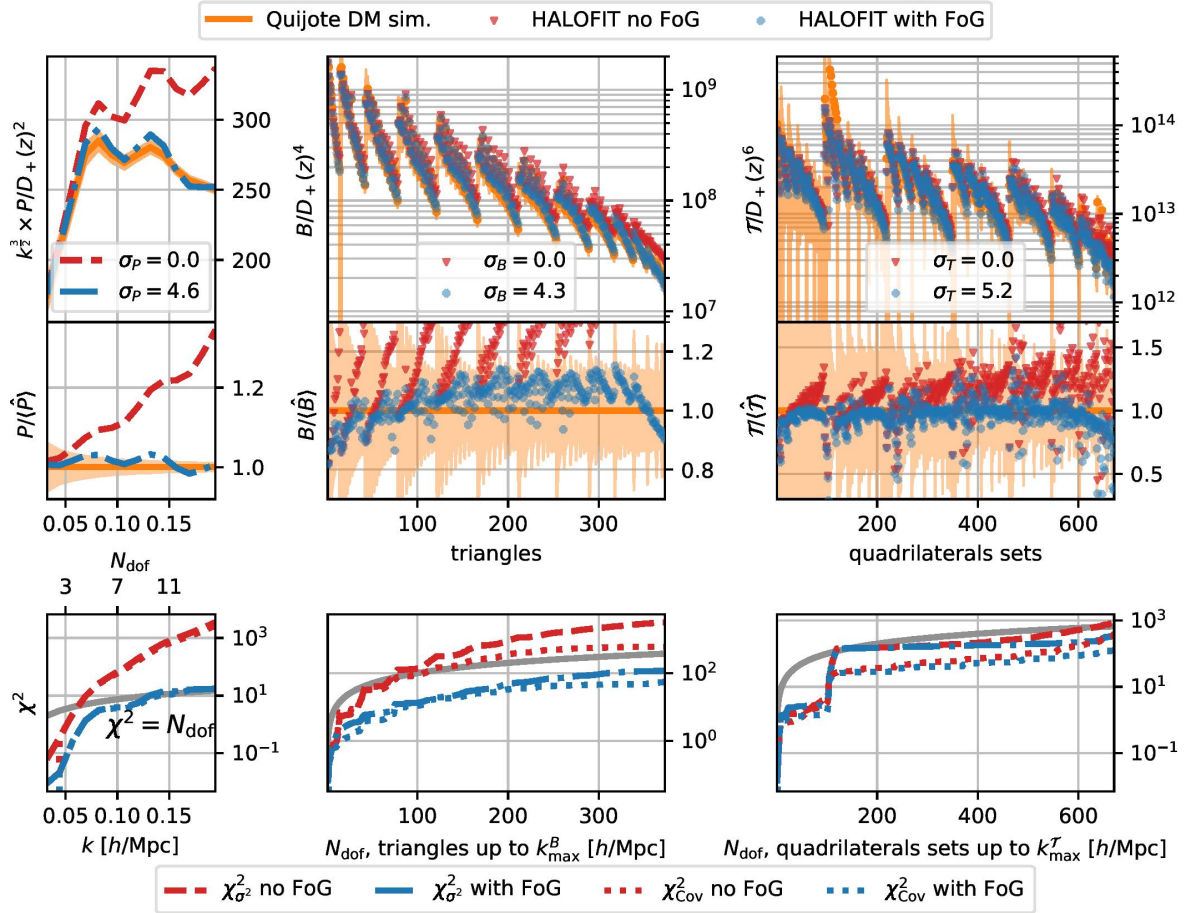


Figure 13. Comparison between measurements of the power spectrum, bispectrum and i-trispectrum monopoles from the QUIJOTE simulations in redshift space at $z = 0.5$ and their relative theoretical models. Differently from what shown in the real space case in figure 6, here we use the effective kernels for the bispectrum with both the linear and HALOFIT fiducial matter power spectrum as input. Also in this case we have that $k_{\max}^P = k_{\max}^B = 1.3 \times k_{\max}^T$, where $k_{\max}^T(z = 0.5) = 0.15 h/\text{Mpc}$. As expected for the chosen redshift, the power spectrum monopole tree level model (equation A.1) computed using the HALOFIT prescription for the matter power spectrum achieves a much better fit than the one using the linear one. The effective model of the redshift second order perturbation theory kernels [34] allows the bispectrum monopole model to have a very good fit up to the maximum k -value. Using the effective second order kernel $Z^{(2)}$ also for the i-trispectrum model returns a very good fit. Especially when the FoG damping is used the ratio between theory and average measurement stabilises around unity for the entire k -range considered.

a theoretical model of the i-trispectrum (equation 2.6) based on perturbation theory. We find very good agreement between i-trispectrum model and measurements (figure 8) up to a maximum k that, as expected, depends on redshift ($k_{\max}^{z=0.5} = 0.15 h/\text{Mpc}$, $k_{\max}^{z=1} = 0.17 h/\text{Mpc}$ and $k_{\max}^{z=2} = 0.19 h/\text{Mpc}$).

It is important to point out that the unconnected component of the four-point correlator (\mathcal{T}_u) must be estimated and subtracted from the total measured four-point signal to isolate the i-trispectrum. The unconnected part is far from being negligible for symmetric configurations (figure 7), and its removal is fundamental in order to isolate the the signal (i-trispectrum)

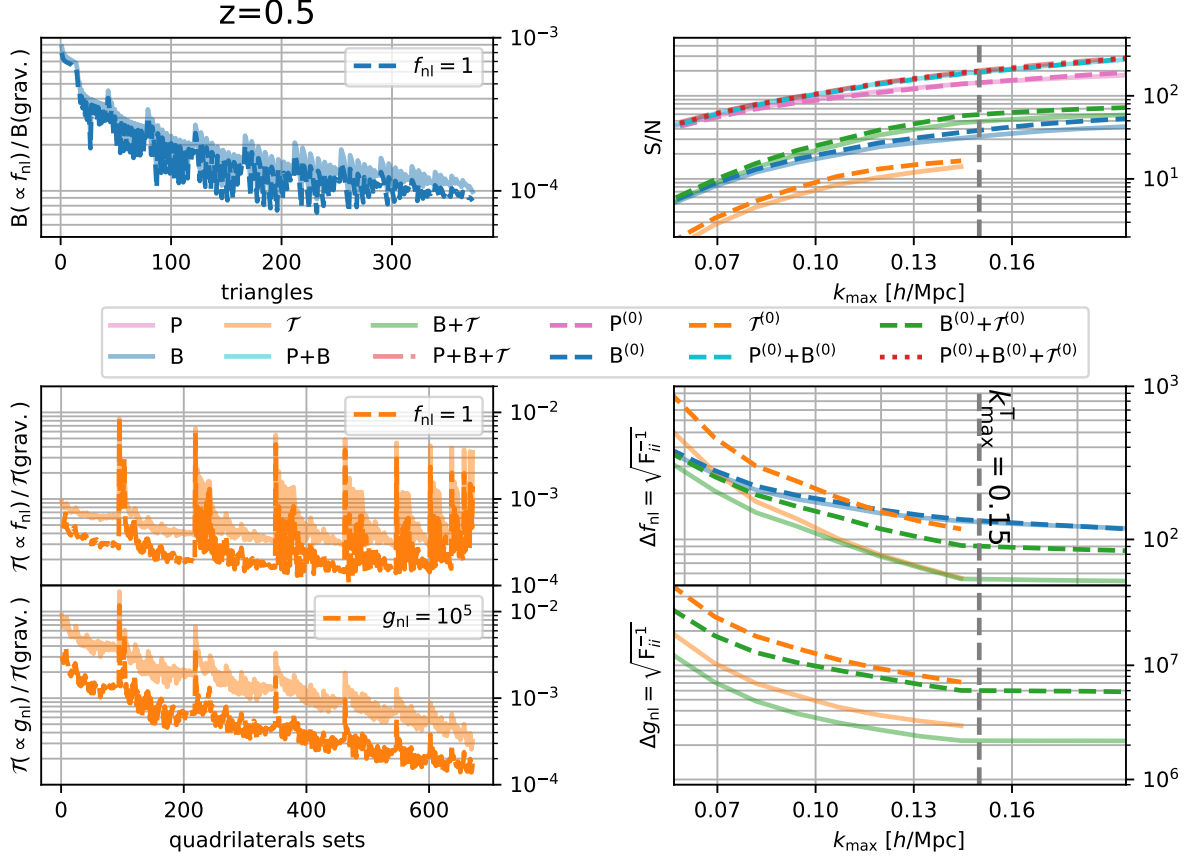


Figure 14. Equivalent of figures 4 (left side) and 11 (right side) for the redshift space case ($z = 0.5$). The real space quantities are reported in lighter tones. Comparing with figure 4 relative to the real space case, we see that while the ratio between primordial and gravitational part for the bispectrum is basically left unchanged, the same ratio for the i-trispectrum monopole is on average slightly lower for both terms proportional to f_{nl} and g_{nl} when passing from real (lighter tone) to redshift (darker tone) space. This reflects into a lower impact in improving the constraints on f_{nl} when adding the i-trispectrum signal to the bispectrum with respect to the bispectrum monopole alone. Even if the parameter constraints improvements for both f_{nl} and g_{nl} are smaller than the ones reported in table 1 for the real case, the i-trispectrum monopole added value is still significant (see table 2 for the exact values) and increases for increasing $k_{\text{max}}^{\mathcal{T}}$.

containing cosmological information of the field not already present in the power spectrum.

From 5000 QUIJOTE simulations we also estimate and present the i-trispectrum covariance matrix and its cross-correlation with power spectrum and bispectrum (figure 9). Comparing it with the simplest covariance analytical model (Gaussian field), we show that non-Gaussian and off-diagonal terms are only negligible above $z \sim 2$ (figure 10). At lower redshifts, where most of the volume of present and forthcoming surveys is located, the Gaussian covariance approximation should not be used.

In analogy to the findings for the Cosmic Microwave Background anisotropies, we envisage the i-trispectrum to be particularly useful to improve the constraints on primordial non-Gaussianity (PNG) arising from lower-order statistics. We thus derive an analytical model for the local PNG signature in the i-trispectrum (equation 2.26 and figure 4), and produce realistic (using a numerically estimated covariance matrix to account for all the

| $z = 0.5, k_{\max} [h/\text{Mpc}] \rightarrow$ | | 0.10 | 0.12 | 0.15 | 0.17 |
|---|-------------------------------|----------------|----------------|----------------|----------------|
| | d | RSD (real) | RSD (real) | RSD (real) | RSD (real) |
| Δf_{nl} | $B^{(0)}$ | 194 (183) | 157 (149) | 135 (132) | 125 (124) |
| | $\mathcal{T}^{(0)}$ | 240 (136) | 153 (80) | 117 (56) | - - |
| | $B + \mathcal{T}^{(0)}$ | 164 (122) | 118 (78) | 91 (55) | 88 (54) |
| $1 - \frac{\Delta f_{\text{nl}}^{B^{(0)}+\mathcal{T}^{(0)}}}{\Delta f_{\text{nl}}^{B^{(0)}}}$ | [%] | 15 (34) | 25 (48) | 32 (58) | 30 (56) |
| Δg_{nl} ($\times 10^{-4}$) | $\mathcal{T}^{(0)}$ | 1404 (545) | 938 (368) | 710 (296) | - - |
| | $B^{(0)} + \mathcal{T}^{(0)}$ | 1049 (379) | 767 (273) | 589 (219) | 583 (218) |
| $1 - \frac{\Delta g_{\text{nl}}^{B^{(0)}+\mathcal{T}^{(0)}}}{\Delta g_{\text{nl}}^{\mathcal{T}^{(0)}}}$ | [%] | 8 (11) | 4 (14) | 5 (19) | - - |

Table 2. 1D 68% forecasted credible regions for both f_{nl} and g_{nl} as a function of k_{\max} for the bispectrum, i-trispectrum and bispectrum plus i-trispectrum in redshift space. Each simulation’s volume is $1 [\text{Gpc}/h]^3$.

cross-correlations), idealized (matter field, hence low shot noise) but incomplete (non including the scale-dependent bias effect) Fisher forecasts on the PNG amplitude parameters f_{nl} and g_{nl} constraints.

In fact, additional information is indeed expected to be enclosed in the statistics of biased tracers showing the scale-dependent bias effect [21], which for the bispectrum and hence by analogy for the trispectrum, is not just present at very large scales but it is spread over many configurations [30, 80, 96].

Including the i-trispectrum in the power spectrum and bispectrum analysis has a significant impact in the resulting constraints (figure 11 and table 1). In particular, in real space the 68% marginalised credible intervals for f_{nl} are approximately halved when the i-trispectrum constraining power is added to the bispectrum.

The redshift space results –monopole only– (section 3.3, figure 13) are qualitatively similar to the real space ones. However the redshift space covariance matrix shows an increased correlation between the i-trispectra of different quadrilaterals sets at the largest scales (figure 12). Only at high k -values this trend inverts, possibly because of the impact of the Finger-of-God effects. This is why the i-trispectrum added value in terms of f_{nl} and g_{nl} constraints (figure 14 and table 2) is reduced compared to the real space case. Nevertheless the inclusion of the i-trispectrum provides a significant $\sim 30\%$ improvement on f_{nl} ’s 68% 1D marginalised credible intervals.

There are some conservative aspects to our analysis, since by considering the matter field there is no scale dependent bias effect [21, 62] boosting the PNG signal. Moreover

we consider a parameter space limited to the two primordial non-Gaussianity amplitudes f_{nl} and g_{nl} . It is reasonable to expect that when considering haloes/galaxies in redshift space, thus constraining a larger parameter set, the inclusion of the i-trispectrum to the data-vector can provide more significant improvements. For example the constraints on the growth rate f , the bias coefficients, the amplitude of dark matter clustering σ_8 , could be also significantly tightened by including the i-trispectrum. Therefore the i-trispectrum has the potential of reducing degeneracies between nuisance (e.g., galaxy bias) and cosmological parameters usually constrained by clustering analysis.

It is important to highlight that both in real and redshift space, the i-trispectrum added value becomes larger as k_{max} increases. This motivates an update of the standard perturbation theory effective model [31, 34] using the i-trispectrum together with the bispectrum to fit the required parameters (Novell et al. in preparation).

The next step in order to bring the i-trispectrum into contact with real LSS data, is to model the signal of haloes or galaxies as biased tracers of the underlying dark matter field. For this we need to extend to third order the multivariate bias expansion necessary to account for the scale-dependent bias effect. This has already been done in redshift space at second order for the bispectrum [7, 30, 95, 96]. We plan to do this in future work.

An advantage of using higher-order statistics such as the bispectrum and i-trispectrum is to derive constraints on f_{nl} and g_{nl} highly complementary to CMB ones, without needing the signal from very large scales ($k \lesssim 0.001 h/\text{Mpc}$) often affected by observational systematic errors, while at the same time including small scales modes. This may not be competitive for the quasars (where volume is very large but the signal to noise ratio is low), but it is interesting for emission line galaxies (ELGs) and luminous red galaxies (LRGs) which cover less volume but have higher signal to noise.

Finally, even more than for the bispectrum [36], an optimal compression algorithm will be needed in order to make it feasible to exploit the i-trispectrum full potential by using the maximum number of quadrilaterals sets allowed by the survey specifications.

We envision that, even if focused mainly on spectroscopic surveys and dark matter tracers, the estimator and the modelling presented here will be of relevance to broader sections of cosmology.

A Theoretical models for power spectrum, bispectrum and i-trispectrum

Below we report the standard perturbation theory (SPT) expressions used in the modelling of the data-vector for the analysis presented in the main text. For completeness we write the models for power spectrum, bispectrum and i-trispectrum for biased tracers in redshift space, with dependence on the orientation with respect to the line of sight ($\mu = \cos(\theta)$ with θ the angle of the k -vector with respect to the line of sight). The expressions for the real space matter field are simply obtained by setting the linear bias parameter to unity in the SPT kernels while all the higher-order bias parameters $b_{i>1}$ together with the logarithmic growth rate parameter f are set to zero. In particular, the halo power spectrum in real space is related at first order to the matter one by $P_{\text{h}}(k) = b_1^2 P(k)$; the real space expressions for the matter bispectrum are reported in the main text in equations 2.2, the real space, matter SPT expression for the i-trispectrum is given in the main text in equation 2.4. In redshift

space and for biased fields we have

$$\begin{aligned}
P^s(\mathbf{k}) &= Z^{(1)}[\mu, b_1, f]^2 P(k) \\
B^s(\mathbf{k}_1, \mathbf{k}_2, \mathbf{k}_3) &= Z^{(1)}[\mu_1, b_1, f] Z^{(1)}[\mu_2, b_1, f] Z^{(2)}[\mathbf{k}_1, \mathbf{k}_2, b_1, b_2, b_{s_2}, f] P(k_1)P(k_2) + 2 \text{ p.} \\
T^s(\mathbf{k}_1, \mathbf{k}_2, \mathbf{k}_3, \mathbf{k}_4) &= 4 Z^{(1)}[\mu_1, b_1, f] Z^{(1)}[\mu_2, b_1, f] P(k_1)P(k_2) \\
&\quad \times \left\{ Z^{(2)}[\mathbf{k}_1, -\mathbf{k}_{13}, b_1, b_2, b_{s_2}, f] Z^{(2)}[\mathbf{k}_2, \mathbf{k}_{13}, b_1, b_2, b_{s_2}, f] P(k_{13}) \right. \\
&\quad \left. + Z^{(2)}[\mathbf{k}_1, -\mathbf{k}_{14}, b_1, b_2, b_{s_2}, f] Z^{(2)}[\mathbf{k}_2, \mathbf{k}_{14}, b_1, b_2, b_{s_2}, f] P(k_{14}) \right\} + 5 \text{ p.} \\
&\quad + 6 Z^{(1)}[\mu_1, b_1, f] Z^{(1)}[\mu_2, b_1, f] Z^{(1)}[\mu_3, b_1, f] \\
&\quad \times Z^{(3)}[\mathbf{k}_1, \mathbf{k}_2, \mathbf{k}_3, b_1, b_2, b_{s_2}, b_3, f] P(k_1)P(k_2)P(k_3) + 3 \text{ p.} \tag{A.1}
\end{aligned}$$

where the redshift-space distortions kernels can be found for example in Ref. [51]’s appendix and a specific study on a more accurate bias expansion at cubic order was done by the authors of Ref. [2]. For what concerns the primordial non-Gaussianity terms reported in equation 2.26 and appendix E for matter field in real space, the equivalent redshift space expressions are obtained by simply replacing the matter field perturbation theory kernels $F^{(i)}$ with the redshift space ones $Z^{(i)}$. Notice that this can be done only for the matter field since when considering haloes or galaxies, the scale-dependent bias effect [21, 62] introduces additional non-negligible terms. As it can be seen from the above expression (see also appendix E.3), the i-trispectrum is composed of two different terms d expansions in perturbation theory up to order $\propto \delta^6$ [28]:

$$T^s(\mathbf{k}_1, \mathbf{k}_2, \mathbf{k}_3, \mathbf{k}_4) = T_{(1122)}^s + T_{(1113)}^s. \tag{A.2}$$

The isotropic signal component –monopole– for both power spectrum and bispectrum in redshift space is given by

$$P^{(0)} = \frac{1}{2} \int_{-1}^1 d\mu P^s(k, \mu) \quad \text{and} \quad B^{(0)} = \frac{1}{4} \int_{-1}^1 d\mu_1 d\mu_2 B^s(\mathbf{k}_1, \mathbf{k}_2, \mathbf{k}_3), \tag{A.3}$$

while the i-trispectrum monopole was defined in the main text in equation 2.7.

To model the small-scales incoherent velocity dispersion, a damping term is added for each statistics [44]. Similarly to the prescriptions used for power spectrum and bispectrum in [32] which require two effective parameters σ_P and σ_B entering the Lorentzian damping functions in front of the respective data-vectors

$$\begin{aligned}
D_{\text{FoG}}^P &= \frac{1}{[1 + k^2 \mu^2 \sigma_P^2 / 2]^2} \\
D_{\text{FoG}}^B &= \frac{1}{[1 + (k_1^2 \mu_1^2 + k_2^2 \mu_2^2 + k_3^2 \mu_3^2)^2 \sigma_B^4 / 2]^2}, \tag{A.4}
\end{aligned}$$

in the case of the i-trispectrum we use the *ansatz*:

$$D_{\text{FoG}}^T = \frac{1}{[1 + (k_1^2 \mu_1^2 + k_2^2 \mu_2^2 + k_3^2 \mu_3^2 + k_4^2 \mu_4^2)^3 \sigma_T^6 / 2]^2}. \tag{A.5}$$

The parameters σ_P , σ_B , σ_T , should be seen as effective parameters to be calibrated on simulations (or measured/marginalised over when analysing the data). In our case we find for each statistic the best-fit value of the respective FoG parameter by minimising the χ_{Cov}^2 as in equation 2.30. The results of this procedure are displayed in figure 15 and the best-fit values are $\sigma_P = 4.6 \text{ Mpc}/h$, $\sigma_B = 4.3 \text{ Mpc}/h$ and $\sigma_T = 5.2 \text{ Mpc}/h$.

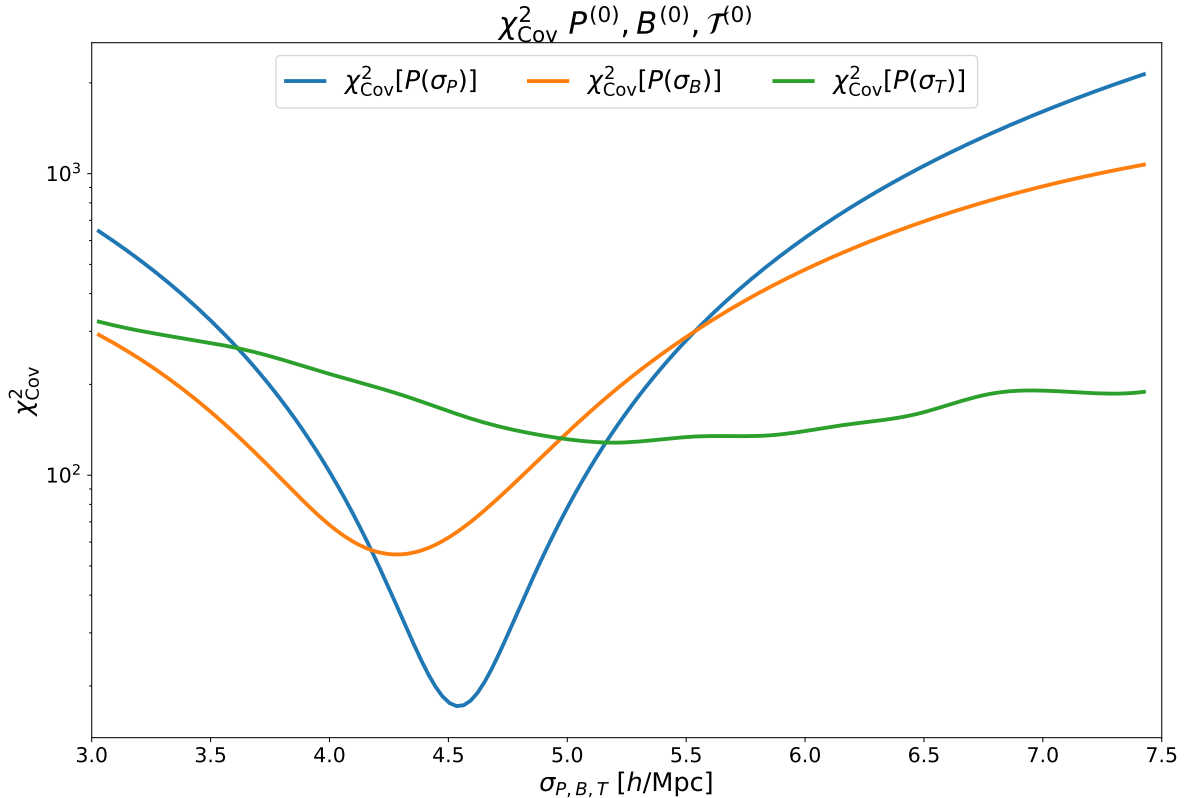


Figure 15. χ_{Cov}^2 -test (equation 2.30) used to find the best-fitting values for the Fingers-of-God parameters, σ_P , σ_B and σ_T (equations A.4 and A.5), for the power spectrum, bispectrum and i-trispectrum of the 5000 realisations of the QUIJOTE N-body simulations.

B Estimators definition

Assuming a cubic survey volume V of size L , the fundamental frequency is $k_f = \frac{2\pi}{L}$. If we divide the box into N equal volume cubic cells per side, the Nyquist frequency is defined as $k_{\text{Ny}} = N \times k_f/2$.

Let's recall that the first step in order to measure statistics in Fourier space from data/simulations is to grid sample the chosen tracers field by using an appropriate mass assignment scheme (see for example [82]). This returns a value of the density field at each grid-node in configuration space. From this set-up it is afterwards possible to exploit discrete Fast Fourier Transforms algorithms (FFT) [29] to obtain the Fourier transform of the density field at each node. The two grids (mass assignment and Fourier transform steps) could in principle be taken to be different but often they coincide (as in our case).

In this section we will refer to the process of converting an estimator in integral form into one written in terms of discrete sums and hence that can be applied onto a pixelated field as "pixelisation".

Using the density (matter/galaxy) perturbation variable δ we define the Fourier transform direct and inverse arbitrary convention:

$$\delta_{\mathbf{k}} = \int d\mathbf{x}^3 \delta_{\mathbf{x}} e^{i\mathbf{k}\mathbf{x}} \quad \text{and} \quad \delta_{\mathbf{x}} = \frac{1}{(2\pi)^3} \int d\mathbf{k}^3 \delta_{\mathbf{k}} e^{-i\mathbf{k}\mathbf{x}}. \quad (\text{B.1})$$

B.1 Power spectrum

The integral version of the estimator for the power spectrum is defined as [37]

$$\hat{P}(k_1) = \frac{(2\pi)^{-3}}{N_p(k_1)} \int_{k_1} d\mathbf{q}_1^3 \int_{k_1} d\mathbf{q}_2^3 \delta_{\mathbf{q}_1} \delta_{\mathbf{q}_2} \delta^D(\mathbf{q}_{12}), \quad (\text{B.2})$$

where each integral is performed over a spherical shell of radius k_i and thickness Δk , and $\mathbf{q}_{12} \equiv \mathbf{q}_1 + \mathbf{q}_2$. N_p is the number of modes found inside the integration volume in Fourier space and it is defined as

$$N_p(k_1) = \frac{V_p(k_1)}{k_f^3} = \frac{1}{k_f^3} \int_{k_1} d\mathbf{q}_1^3 \int_{k_1} d\mathbf{q}_2^3 \delta^D(\mathbf{q}_{12}). \quad (\text{B.3})$$

In order to derive the pixelised version of the above estimator we need the Dirac's delta expression as Fourier transform of 1:

$$\delta^D(\mathbf{q}) = \int \frac{d\mathbf{x}^3}{(2\pi)^3} e^{i\mathbf{x}\mathbf{q}}. \quad (\text{B.4})$$

Therefore in equations B.2 and B.3 we can expand the Dirac's delta and rearrange the order of integration. Proceeding with equation B.2 by also expanding N_p we have

$$\begin{aligned} \hat{P}(k_1) &= (2\pi)^{-3} \int d\mathbf{x}^3 \int_{k_1} d\mathbf{q}_1^3 \delta_{\mathbf{q}_1} e^{i\mathbf{x}\mathbf{q}_1} \int_{k_1} d\mathbf{q}_2^3 \delta_{\mathbf{q}_2} e^{i\mathbf{x}\mathbf{q}_2} \\ &\quad \times \left[k_f^{-3} \int d\mathbf{y}^3 \int_{k_1} d\mathbf{q}_1^3 e^{i\mathbf{y}\mathbf{q}_1} \int_{k_1} d\mathbf{q}_2^3 e^{i\mathbf{y}\mathbf{q}_2} \right]^{-1}. \end{aligned} \quad (\text{B.5})$$

Now we introduce the two quantities:

$$I_{k_i}(\mathbf{x}) = \int_{k_i} \frac{d\mathbf{q}_i^3}{(2\pi)^3} \delta_{\mathbf{q}_i} e^{i\mathbf{x}\mathbf{q}_i} \quad \text{and} \quad J_{k_i}(\mathbf{x}) = \int_{k_i} \frac{d\mathbf{q}_i^3}{(2\pi)^3} e^{i\mathbf{x}\mathbf{q}_i}, \quad (\text{B.6})$$

which applied to equation B.5 give,

$$\hat{P}(k_1) = (2\pi)^3 k_f^3 \int d\mathbf{x}^3 I_{k_1}(\mathbf{x}) I_{k_2}(\mathbf{x}) \times \left[(2\pi)^6 \int d\mathbf{y}^3 J_{k_1}(\mathbf{y}) J_{k_2}(\mathbf{y}) \right]^{-1}. \quad (\text{B.7})$$

To take advantage of fast Fourier transform techniques, each continuous integral over the whole spatial volume can be pixelised as $\int d\mathbf{x}^3 \rightarrow \Delta V \sum_{\ell=1}^{N^3}$, where $\Delta V = \frac{L^3}{N^3}$ is the volume of each cell. Then equation B.7 can be rewritten as,

$$\begin{aligned} \hat{P}(k_1) &= (2\pi)^{-3} k_f^3 \sum_{\iota=1}^{N^3} I_{k_1}(x_\iota) I_{k_2}(x_\iota) \times \left[\sum_{j=1}^{N^3} J_{k_1}(y_j) J_{k_2}(y_j) \right]^{-1} \\ &= L^{-3} \sum_{\iota=1}^{N^3} I_{k_1}(x_\iota) I_{k_2}(x_\iota) \times \left[\sum_{j=1}^{N^3} J_{k_1}(y_j) J_{k_2}(y_j) \right]^{-1}. \end{aligned} \quad (\text{B.8})$$

We start by pixelising the Fourier transform of the density field $\delta_{\mathbf{q}_i}$:

$$\delta_{\mathbf{q}_i} = \int d\mathbf{x}^3 \delta_{\mathbf{x}} e^{i\mathbf{x}\mathbf{q}_i} \quad \longrightarrow \quad \left(\frac{L}{N}\right)^3 \sum_{j=1}^{N^3} e^{iq_i x_j} \delta_{x_j} = \left(\frac{L}{N}\right)^3 F_{\mathbf{q}_i}, \quad (\text{B.9})$$

where F_i is the quantity computed from the Discrete Fourier Transforms algorithm (in our case FFTW [26]). Then we can proceed to pixelise both quantities in equation B.6:

$$\begin{aligned} I_{k_i}(\mathbf{x}) &= \int_{k_i} \frac{d\mathbf{q}_i^3}{(2\pi)^3} e^{i\mathbf{x}\mathbf{q}_i} \left(\frac{L}{N}\right)^3 F_{\mathbf{q}_i} = \int \frac{d\mathbf{q}^3}{(2\pi)^3} e^{i\mathbf{x}\mathbf{q}} \left(\frac{L}{N}\right)^3 F_{\mathbf{q}}^i \\ &\rightarrow \left(\frac{L}{N}\right)^3 \left(\frac{1}{N}\right)_{\text{IFT}}^3 \sum_{\ell=1}^{N^3} e^{i\mathbf{x}\mathbf{q}_\ell} F_{\mathbf{q}_\ell}^i = \left(\frac{L}{N}\right)^3 \left(\frac{1}{N}\right)_{\text{IFT}}^3 I_{k_i}^D(\mathbf{x}) \\ J_{k_i}(\mathbf{x}) &= \int_{k_i} \frac{d\mathbf{q}_i^3}{(2\pi)^3} e^{i\mathbf{x}\mathbf{q}_i} = \int \frac{d\mathbf{q}^3}{(2\pi)^3} e^{i\mathbf{x}\mathbf{q}} S_{\mathbf{q}}^i \\ &\rightarrow \left(\frac{1}{N}\right)_{\text{IFT}}^3 \sum_{\ell=1}^{N^3} e^{i\mathbf{x}\mathbf{q}_\ell} S_{\mathbf{q}_\ell}^i = \left(\frac{1}{N}\right)_{\text{IFT}}^3 J_{k_i}^D(\mathbf{x}) \end{aligned} \quad (\text{B.10})$$

where in the first step the index i is used to indicate that the integrand is non-null only within the shell with radius k_i and thickness Δk . Hence $S_{\mathbf{q}}^i$ is defined so that it is equal to unity for \mathbf{q} inside the k_i -shell and zero outside. The normalisation factor due to the discrete inverse Fourier transform has been specified using the "IFT" subscript (inverse Fourier transform).

Finally with the pixelised result of equation B.10, B.8 becomes:

$$\begin{aligned} \hat{P}(k_1) &= L^{-3} \sum_{i=1}^{N^3} I_{k_1}(x_i) I_{k_2}(x_i) \times \left[\sum_{j=1}^{N^3} J_{k_1}(y_j) J_{k_2}(y_j) \right]^{-1} \\ &\rightarrow L^{-3} \left(\frac{L}{N}\right)^6 \left(\frac{1}{N}\right)_{\text{IFT}}^6 \sum_{i=1}^{N^3} I_{k_1}^D(x_i) I_{k_2}^D(x_i) \times \left[\left(\frac{1}{N}\right)_{\text{IFT}}^6 \sum_{j=1}^{N^3} J_{k_1}^D(y_j) J_{k_2}^D(y_j) \right]^{-1} \\ &= \frac{L^3}{N^6} \sum_{i=1}^{N^3} I_{k_1}^D(x_i) I_{k_2}^D(x_i) \times \left[\sum_{j=1}^{N^3} J_{k_1}^D(y_j) J_{k_2}^D(y_j) \right]^{-1}. \end{aligned} \quad (\text{B.11})$$

By construction, $\hat{P}(k_1)$ has the appropriate dimension of length to the power of 3.

B.2 Bispectrum

Starting from the unbiased estimator as defined in [37], for the bispectrum we have,

$$\hat{B}(k_1, k_2, k_3) = \frac{V(2\pi)^{-6}}{N_t(k_1, k_2, k_3)} \int_{k_1} d\mathbf{q}_1^3 \int_{k_2} d\mathbf{q}_2^3 \int_{k_3} d\mathbf{q}_3^3 \delta_{\mathbf{q}_1} \delta_{\mathbf{q}_2} \delta_{\mathbf{q}_3} \delta^D(\mathbf{q}_{123}), \quad (\text{B.12})$$

where $\mathbf{q}_{123} \equiv \mathbf{q}_1 + \mathbf{q}_2 + \mathbf{q}_3$, N_t is the number of triangles included in the integration volume in Fourier space,

$$N_t(k_1, k_2, k_3) = \frac{V_t(k_1, k_2, k_3)}{k_f^6} = \frac{1}{k_f^6} \int_{k_1} d\mathbf{q}_1^3 \int_{k_2} d\mathbf{q}_2^3 \int_{k_3} d\mathbf{q}_3^3 \delta^D(\mathbf{q}_{123}) . \quad (\text{B.13})$$

Proceeding then as for the power spectrum and decomposing the Dirac's deltas using equation B.4 to derive the quantities in equation B.6 and pixelising using equation B.10 we have that

$$\begin{aligned} \hat{B}(k_1, k_2, k_3) &= V(2\pi)^3 k_f^6 \int d\mathbf{x}^3 I_{k_1}(\mathbf{x}) I_{k_2}(\mathbf{x}) I_{k_3}(\mathbf{x}) \times \left[(2\pi)^9 \int d\mathbf{y}^3 J_{k_1}(\mathbf{y}) J_{k_2}(\mathbf{y}) J_{k_3}(\mathbf{y}) \right]^{-1} \\ &\rightarrow L^{-3} \left(\frac{L}{N} \right)^9 \left(\frac{1}{N} \right)_{\text{IFT}}^9 \sum_{i=1}^{N^3} I_{k_1}^D(x_i) I_{k_2}^D(x_i) I_{k_3}^D(x_i) \\ &\times \left[\left(\frac{1}{N} \right)_{\text{IFT}}^9 \sum_{j=1}^{N^3} J_{k_1}^D(y_j) J_{k_2}^D(y_j) J_{k_3}^D(y_j) \right]^{-1} \\ &= \left(\frac{L^6}{N^9} \right) \sum_{i=1}^{N^3} I_{k_1}^D(x_i) I_{k_2}^D(x_i) I_{k_3}^D(x_i) \times \left[\sum_{j=1}^{N^3} J_{k_1}^D(y_j) J_{k_2}^D(y_j) J_{k_3}^D(y_j) \right]^{-1} . \end{aligned} \quad (\text{B.14})$$

The dimension of \hat{B} is by construction length to the power of 6.

B.3 I-trispectrum

In analogy to the bispectrum, for the (integrated) i-trispectrum (see main text for more details) we begin by defining the unbiased estimator

$$\begin{aligned} \hat{\mathcal{T}}_{c+u}(k_1, k_2, k_3, k_4) &= \frac{V^2(2\pi)^{-9}}{N_q(k_1, k_2, k_3, k_4)} \int_{k_1} d\mathbf{q}_1^3 \int_{k_2} d\mathbf{q}_2^3 \int_{k_3} d\mathbf{q}_3^3 \\ &\times \int_{k_4} d\mathbf{q}_4^3 \delta_{\mathbf{q}_1} \delta_{\mathbf{q}_2} \delta_{\mathbf{q}_3} \delta_{\mathbf{q}_4} \delta^D(\mathbf{q}_{1234}) , \end{aligned} \quad (\text{B.15})$$

where $\mathbf{q}_{1234} \equiv \mathbf{q}_1 + \mathbf{q}_2 + \mathbf{q}_3 + \mathbf{q}_4$, N_q is the number of skew-quadrilaterals in the integration volume in Fourier space, defined as

$$N_q(k_1, k_2, k_3, k_4) = \frac{V_q(k_1, k_2, k_3, k_4)}{k_f^9} = \frac{1}{k_f^9} \int_{k_1} d\mathbf{q}_1^3 \int_{k_2} d\mathbf{q}_2^3 \int_{k_3} d\mathbf{q}_3^3 \int_{k_4} d\mathbf{q}_4^3 \delta^D(\mathbf{q}_{1234}) . \quad (\text{B.16})$$

We can confirm that it is actually an unbiased estimator, as for the cases of power spectrum and bispectrum, by taking the ensemble average,

$$\begin{aligned} \langle \hat{\mathcal{T}}_{c+u}(k_1, k_2, k_3, k_4) \rangle &= \frac{V^2(2\pi)^{-9}}{N_q(k_1, k_2, k_3, k_4)} \int_{k_1} d\mathbf{q}_1^3 \int_{k_2} d\mathbf{q}_2^3 \int_{k_3} d\mathbf{q}_3^3 \int_{k_4} d\mathbf{q}_4^3 \langle \delta_{\mathbf{q}_1} \delta_{\mathbf{q}_2} \delta_{\mathbf{q}_3} \delta_{\mathbf{q}_4} \rangle \\ &\times \delta^D(\mathbf{q}_{1234}) \\ &= \frac{V^2(2\pi)^{-9}}{N_q(k_1, k_2, k_3, k_4)} \int_{k_1} d\mathbf{q}_1^3 \int_{k_2} d\mathbf{q}_2^3 \int_{k_3} d\mathbf{q}_3^3 \\ &\times \int_{k_4} d\mathbf{q}_4^3 [\langle \delta_{\mathbf{q}_1} \delta_{\mathbf{q}_2} \delta_{\mathbf{q}_3} \delta_{\mathbf{q}_4} \rangle_c + \langle \delta_{\mathbf{q}_1} \delta_{\mathbf{q}_2} \rangle \langle \delta_{\mathbf{q}_3} \delta_{\mathbf{q}_4} \rangle + 2 \text{p.}] \delta^D(\mathbf{q}_{1234}) . \end{aligned} \quad (\text{B.17})$$

We then separately analyse the connected term and the unconnected one obtained by applying Wick's theorem to complete the proof of the above estimator being unbiased.

B.3.1 I-trispectrum: connected part and total signal

If one considers only the connected part of the total signal estimator introduced in equation B.17, it is possible to recover the correspondence with the i-trispectrum signal

$$\begin{aligned}
\langle \hat{\mathcal{T}}_c(k_1, k_2, k_3, k_4) \rangle &= \frac{V^2 (2\pi)^{-9} k_f^9}{V_q(k_1, k_2, k_3, k_4)} \int_{k_1} d\mathbf{q}_1^3 \int_{k_2} d\mathbf{q}_2^3 \int_{k_3} d\mathbf{q}_3^3 \int_{k_4} d\mathbf{q}_4^3 \\
&\times (2\pi)^3 \delta^D(\mathbf{q}_{1234})^2 T(\mathbf{q}_1, \mathbf{q}_2, \mathbf{q}_3, \mathbf{q}_4) \\
&= \frac{(2\pi)^{-3} k_f^3}{V_q(k_1, k_2, k_3, k_4)} \int_{k_1} d\mathbf{q}_1^3 \int_{k_2} d\mathbf{q}_2^3 \int_{k_3} d\mathbf{q}_3^3 \int_{k_4} d\mathbf{q}_4^3 (2\pi)^3 k_f^{-3} \delta^D(\mathbf{q}_{1234}) T(\mathbf{q}_1, \mathbf{q}_2, \mathbf{q}_3, \mathbf{q}_4) \\
&= \frac{1}{V_q(k_1, k_2, k_3, k_4)} \int_{k_1} d\mathbf{q}_1^3 \int_{k_2} d\mathbf{q}_2^3 \int_{k_3} d\mathbf{q}_3^3 \int_{k_4} d\mathbf{q}_4^3 \delta^D(\mathbf{q}_{1234}) T(\mathbf{q}_1, \mathbf{q}_2, \mathbf{q}_3, \mathbf{q}_4) \\
&\approx \mathcal{T}_c(k_1, k_2, k_3, k_4) \frac{1}{V_q(k_1, k_2, k_3, k_4)} \int_{k_1} d\mathbf{q}_1^3 \int_{k_2} d\mathbf{q}_2^3 \int_{k_3} d\mathbf{q}_3^3 \int_{k_4} d\mathbf{q}_4^3 \delta^D(\mathbf{q}_{1234}) \\
&= \mathcal{T}(k_1, k_2, k_3, k_4) .
\end{aligned} \tag{B.18}$$

Here, as in [47], we exploited the fact that $\delta^{D^2} \approx \delta^D k_f^{-3}$. In the last passage we assumed that if the k -shell's thickness Δk is small enough, then after the implicit average over the possible diagonals values, $\mathcal{T}(k_1, k_2, k_3, k_4)$ can be brought outside of the integrals. Under these approximations, this connected part of the estimator is unbiased and equivalent to measuring the i-trispectrum.

Then the full four-point correlation estimator can be pixelised (again using equation B.10 for the total estimator trispectrum + unconnected part) as

$$\begin{aligned}
\hat{\mathcal{T}}_{c+u}(k_1, k_2, k_3, k_4) &= V^2 (2\pi)^3 k_f^9 \int d\mathbf{x}^3 I_{k_1}(\mathbf{x}) I_{k_2}(\mathbf{x}) I_{k_3}(\mathbf{x}) I_{k_4}(\mathbf{x}) \\
&\times \left[(2\pi)^{12} \int d\mathbf{y}^3 J_{k_1}(\mathbf{y}) J_{k_2}(\mathbf{y}) J_{k_3}(\mathbf{y}) J_{k_4}(\mathbf{y}) \right]^{-1} \\
&\rightarrow \frac{L^9}{N^{12}} \sum_{i=1}^{N^3} I_{k_1}^D(x_i) I_{k_2}^D(x_i) I_{k_3}^D(x_i) I_{k_4}^D(x_i) \times \left[\sum_{j=1}^{N^3} J_{k_1}^D(y_j) J_{k_2}^D(y_j) J_{k_3}^D(y_j) J_{k_4}^D(y_j) \right]^{-1} .
\end{aligned} \tag{B.19}$$

From the last line of equation B.19 we see that also the pixelised version of the estimator $\hat{\mathcal{T}}_{c+u}$ has by construction dimensions of length to the power of 9.

B.3.2 Unconnected part

We now expand the unconnected part of the estimator for one of the three possible permutations:

$$\begin{aligned}
\langle \hat{\mathcal{T}}_u(k_1, k_2, k_3, k_4) \rangle &= \frac{V^2 (2\pi)^{-9} k_f^9}{V_q(k_1, k_2, k_3, k_4)} \int_{k_1} d\mathbf{q}_1^3 \int_{k_2} d\mathbf{q}_2^3 \int_{k_3} d\mathbf{q}_3^3 \int_{k_4} d\mathbf{q}_4^3 \\
&\times (2\pi)^3 \delta^D(\mathbf{q}_{12}) P(\mathbf{q}_1) (2\pi)^3 \delta^D(\mathbf{q}_{34}) P(\mathbf{q}_3) \delta^D(\mathbf{q}_{1234}) \quad (+2\text{p.}) \\
&= \frac{(2\pi)^3 k_f^3}{V_q(k_1, k_2, k_3, k_4)} \int_{k_1} d\mathbf{q}_1^3 \int_{k_2} d\mathbf{q}_2^3 \int_{k_3} d\mathbf{q}_3^3 \int_{k_4} d\mathbf{q}_4^3 \\
&\times \delta^D(\mathbf{q}_{12}) \delta^D(\mathbf{q}_{34}) \delta^D(\mathbf{q}_{1234}) P(\mathbf{q}_1) P(\mathbf{q}_3) \quad (+2\text{p.}) \\
&= \frac{(2\pi)^3 k_f^3}{V_q(k_1, k_2, k_3, k_4)} \int_{k_1} d\mathbf{q}_1^3 \int_{k_2} d\mathbf{q}_2^3 \delta^D(\mathbf{q}_{12}) P(\mathbf{q}_1) \int_{k_3} d\mathbf{q}_3^3 \int_{k_4} d\mathbf{q}_4^3 \delta^D(\mathbf{q}_{34})^2 P(\mathbf{q}_3) \quad (+2\text{p.}) \\
&= \frac{(2\pi)^3}{V_q(k_1, k_2, k_3, k_4)} \int_{k_1} d\mathbf{q}_1^3 \int_{k_2} d\mathbf{q}_2^3 \delta^D(\mathbf{q}_{12}) P(\mathbf{q}_1) \int_{k_3} d\mathbf{q}_3^3 \int_{k_4} d\mathbf{q}_4^3 \delta^D(\mathbf{q}_{34}) P(\mathbf{q}_3) \quad (+2\text{p.}).
\end{aligned} \tag{B.20}$$

To evaluate B.20 two alternatives are possible: the analytical approach or the numerical one. In the analytical approach we use the theoretical expressions for the integration volume in Fourier space for both power spectrum and i-trispectrum [39]. The analytical approach derives the theoretical result for the model of the integrated trispectrum unconnected part, since a-priori its precise form is unknown (it is expected of course to be proportional to $\propto P(k_i)P(k_j)$).

The numerical approach on the other end, proves that the estimator defined for the unconnected part of the integrated trispectrum is unbiased. In this case one can pixelise this unconnected part of the estimator as done for the connected part. In both cases the unconnected part needs to be subtracted from the measured total signal in order to obtain the i-trispectrum.

Analytical approach We start by recalling the two expressions for the integration volumes [39]:

$$V_p(k_1) = 4\pi k_1^2 \Delta k_1 \quad \text{and} \quad V_q(k_1, k_2, k_3, k_4) = 16\pi^3 k_1 k_2 k_3 k_4 \Delta k_1 \Delta k_2 \Delta k_3 \Delta k_4 \Delta D, \tag{B.21}$$

where Δk_i is the bin-size for the i -th k -mode. Resuming from the last line of equation B.20 and assuming that, if the k -shells are thin enough, the averaged value of the power spectrum does not differ significantly from the value computed at the centre of the bin, we have that

$$\begin{aligned}
\langle \hat{\mathcal{T}}(k_1, k_2, k_3, k_4) \rangle_u &\approx \frac{(2\pi)^3}{V_q(k_1, k_2, k_3, k_4)} P(k_1) P(k_3) \int_{k_1} d\mathbf{q}_1^3 \int_{k_2} d\mathbf{q}_2^3 \delta^D(\mathbf{q}_{12}) \\
&\times \int_{k_3} d\mathbf{q}_3^3 \int_{k_4} d\mathbf{q}_4^3 \delta^D(\mathbf{q}_{34}) \quad (+x\text{p.}) \\
&= (2\pi)^3 P(k_1) P(k_3) \delta_{12}^K \delta_{34}^K \frac{4\pi k_1^2 \Delta k_1 \times 4\pi k_3^2 \Delta k_3}{16\pi^3 k_1 k_2 k_3 k_4 \Delta k_1 \Delta k_2 \Delta k_3 \Delta k_4 \Delta D} + (x\text{p.}) \\
&= \frac{(2\pi)^3 \delta_{12}^K \delta_{34}^K P(k_1) P(k_3)}{\pi \Delta k_2 \Delta k_4 \Delta D} + (x\text{p.}).
\end{aligned} \tag{B.22}$$

where $x = 2$ for the case of a quadrilateral with four equal sides, $k_1 = k_2 = k_3 = k_4$. In the case of quadrilaterals sets with pairs of equal sides there is only one non-null permutation ($x = 0$). Given the algorithm we use to generate quadrilaterals sets (see figure 3), in our work the above only happens for example $k_1 = k_2$ and $k_3 = k_4$.

A quick dimensional analysis shows that this result has the expected dimensions of length to the power of 9, the same as the connected term (trispectrum).

Numerical approach By taking the ensemble average it is possible to check that the following estimator is unbiased with respect to the final result of the analytical approach in equation B.22

$$\begin{aligned} \hat{\mathcal{T}}_{\text{u}}(k_1, k_2, k_3, k_4) &= \frac{V(2\pi)^{-9}}{N_{\text{q}}(k_1, k_2, k_3, k_4)} \int_{k_1} d\mathbf{q}_1^3 \int_{k_2} d\mathbf{q}_2^3 \delta_{\mathbf{q}_1} \delta_{\mathbf{q}_2} \delta^D(\mathbf{q}_{12}) \\ &\times \int_{k_3} d\mathbf{q}_3^3 \int_{k_4} d\mathbf{q}_4^3 \delta_{\mathbf{q}_3} \delta_{\mathbf{q}_4} \delta^D(\mathbf{q}_{34}) + 2 \text{ p. ,} \end{aligned} \quad (\text{B.23})$$

which we can pixelised analogously to what done for the connected part for each of the permutations:

$$\begin{aligned} \hat{\mathcal{T}}_{\text{u}}(k_1, k_2, k_3, k_4) &= V(2\pi)^3 k_{\text{f}}^9 \int d\mathbf{x}^3 I_{k_1}(\mathbf{x}) I_{k_2}(\mathbf{x}) \int d\mathbf{z}^3 I_{k_3}(\mathbf{z}) I_{k_4}(\mathbf{z}) \\ &\times \left[(2\pi)^{12} \int d\mathbf{y}^3 J_{k_1}(\mathbf{y}) J_{k_2}(\mathbf{y}) J_{k_3}(\mathbf{y}) J_{k_4}(\mathbf{y}) \right]^{-1} \\ &= V(2\pi)^{-9} k_{\text{f}}^9 \Delta V^2 \sum_{i=1}^{N^3} I_{k_1}(x_i) I_{k_2}(x_i) \sum_{\ell=1}^{N^3} I_{k_3}(z_\ell) I_{k_4}(z_\ell) \\ &\times \Delta V \left[\sum_{j=1}^{N^3} J_{k_1}(y_j) J_{k_2}(y_j) J_{k_3}(y_j) J_{k_4}(y_j) \right]^{-1} \\ &= \frac{1}{L^3 N^3} \sum_{i=1}^{N^3} I_{k_1}(x_i) I_{k_2}(x_i) \sum_{\ell=1}^{N^3} I_{k_3}(z_\ell) I_{k_4}(z_\ell) \left[\sum_{j=1}^{N^3} J_{k_1}(y_j) J_{k_2}(y_j) J_{k_3}(y_j) J_{k_4}(y_j) \right]^{-1}. \end{aligned} \quad (\text{B.24})$$

Once again, pixelising using equation B.10, we have that the i-trispectrum unconnected part estimator becomes

$$\begin{aligned} \hat{\mathcal{T}}_{\text{u}}(k_1, k_2, k_3, k_4) &= \frac{1}{L^3 N^3} \sum_{i=1}^{N^3} I_{k_1}(x_i) I_{k_2}(x_i) \sum_{\ell=1}^{N^3} I_{k_3}(z_\ell) I_{k_4}(z_\ell) \\ &\times \left[\sum_{j=1}^{N^3} J_{k_1}(y_j) J_{k_2}(y_j) J_{k_3}(y_j) J_{k_4}(y_j) \right]^{-1} \\ &\rightarrow \frac{L^9}{N^{15}} \sum_{i=1}^{N^3} I_{k_1}^D(x_i) I_{k_2}^D(x_i) \sum_{\ell=1}^{N^3} I_{k_3}^D(z_\ell) I_{k_4}^D(z_\ell) \left[\sum_{j=1}^{N^3} J_{k_1}^D(y_j) J_{k_2}^D(y_j) J_{k_3}^D(y_j) J_{k_4}^D(y_j) \right]^{-1}. \end{aligned} \quad (\text{B.25})$$

The above result for the pixelised estimator corresponds to the analytical model derived in equation B.22.

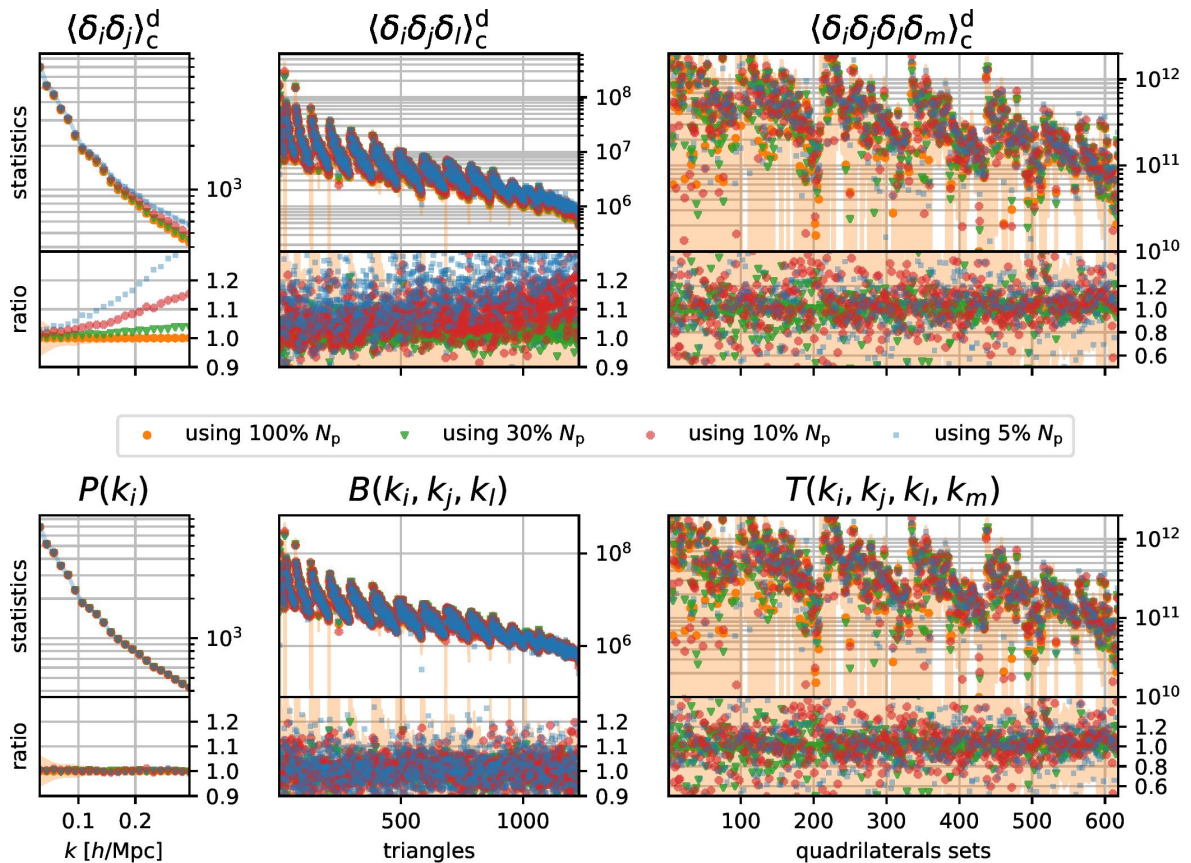


Figure 16. Comparison between measured connected discrete correlators (upper half, from equations 2.11, 2.13, 2.16) and the derived statistics obtained by subtracting the shot-noise estimated contributions (lower half, following equations C.1 and C.2) for different randomly selected fractions of the total number of dark matter particles present in the simulations. The results are shown for $z = 1$, and the shaded areas are centred around the 100% N_p case, which is used also as denominator in each ratio sub-plot. The green, red and blue points are respectively the cases considering 30%, 10% and 5% of the dark matter particles (randomly selected). While being significant in the cases of power spectrum and bispectrum especially at large k -values, for the i-trispectrum the shot-noise impact is not noticeable because of the large sample variance which is always dominant even when lowering the tracers density (at least up to the k_{\max} considered in this work).

C Shot-noise correction

If the observed field is a Poisson sample of a (possibly hypothetical) continuous underlying field, the measured correlations would be affected by a shot-noise contribution which acts as a noise bias. In order to subtract the shot-noise contribution from the measured signal, we implement the suitable estimators (combinations of power spectra, bispectra and average particles density number) necessary to reproduce the terms described in the appendix of [98] under the assumption of Poissonian shot-noise. The expressions for power spectrum and bispectrum are

$$\begin{aligned}
\langle \delta_i \delta_j \rangle_c^d &= (2\pi)^3 \delta^D(\mathbf{k}_{ij}) \left[P(k_i) + \frac{1}{\bar{n}} \right] \\
\langle \delta_i \delta_j \delta_l \rangle_c^d &= (2\pi)^3 \delta^D(\mathbf{k}_{ijl}) \left[B(k_i, k_j, k_l) + \frac{1}{\bar{n}} (P(k_i) + P(k_j) + P(k_l)) + \frac{1}{\bar{n}^2} \right],
\end{aligned} \tag{C.1}$$

where the index "d" and subscript "c" stand for "discrete" and "connected", respectively and \bar{n} denotes the number density of objects. Notice that in this section we use the word "discrete" to indicate that the considered statistics are measured from a set of objects and not a continuous field. For the i-trispectrum, given the fact that for each set of (k_i, k_j, k_l, k_m) there is an infinite number of possible quadrilateral shapes, the shot-noise expression from [98] needs to be modified. In particular for a given Δk used to bin the k -values in the measurement there is a finite number of possible values of the diagonal D ranging between a D_{\min} and a D_{\max} as defined in equation 2.5, $N_D = (D_{\max} - D_{\min})/\Delta k$. This of course is true in the case of the shot-noise correction being estimated directly from the data. Therefore, for each of the i-trispectrum configurations defined by a set of k -values (k_i, k_j, k_l, k_m) , the shot-noise expression becomes,

$$\begin{aligned}
&\langle \delta_i \delta_j \delta_l \delta_m \rangle_c^d \\
&= (2\pi)^3 \delta^D(\mathbf{k}_{ijklm}) \left\{ T(k_i, k_j, k_l, k_m) \right. \\
&+ \frac{1}{3} \sum_{\substack{k_1, k_2, k_3, k_4 \\ k_1, k_3, k_2, k_4 \\ k_1, k_2, k_4, k_3}} \left[\frac{1}{\bar{n}} \left(B(|\mathbf{k}_i + \mathbf{k}_j|, k_l, k_m) \Big|_{D_{\text{av.}}} + 5 \text{ perm.} \right) \right. \\
&+ \left. \left. \frac{1}{\bar{n}^2} \left(P(|\mathbf{k}_i + \mathbf{k}_j + \mathbf{k}_l|) \Big|_{D_{\text{av.}}} + 3 \text{ perm.} + 2P(|\mathbf{k}_i + \mathbf{k}_j|) \Big|_{D_{\text{av.}}} + 2 \text{ perm.} \right) \right] + \frac{1}{\bar{n}^3} \right\},
\end{aligned} \tag{C.2}$$

where we used the diagonal intermediate value of each configuration's possible range $D_{\text{av.}} = (D_{\min} + D_{\max})/2$ to compute the vectors sums appearing the bispectra and power spectra arguments. The terms proportional to powers of $1/\bar{n}$ constitute the shot-noise "bias" which should be subtracted from the measured signal. Therefore these terms are first measured from the simulations and directly subtracted afterwards from the total signal measured using the estimators in equations 2.11, 2.13 and 2.17. Equation C.2 is clearly an approximation, a more rigorous treatment would involve averaging the above terms over all the possible values of the diagonal D . We tested this and found no significant change. Most likely this is due to the fact the i-trispectrum measurement is dominated by statistical noise as it can be seen from figure 16. Notice that the term $P(|\mathbf{k}_i + \mathbf{k}_j + \mathbf{k}_l|) = P(k_m)$ for the closure condition, and therefore does not need to be averaged.

Figure 16 shows the increase in relevance of the shot-noise term as the number of tracers N_p decreases. For one realisation at $z = 1$, the dark matter particles present in the cubic box have been randomly sampled to include 5%, 10%, 30% and 100% of the total. In the upper half of the figure shows the corresponding discrete power spectrum, bispectrum and connected part of the i-trispectrum, measured using the estimators in equations 2.11, 2.13,

2.16. In the lower half the same cases have been shown for the statistics of interest obtained subtracting the shot-noise terms as described in equations C.1 and C.2.

Without shot-noise correction a significant bias would be induced in both power spectrum and bispectrum measurements, especially at large k -values. The relevance of this bias is given by its comparison with the error bars derived from the set of measurements on the simulations. For the i-trispectrum, even when decreasing the number of samples down to 5% of the original set, the induced shift in the statistics is still smaller than the error bars. The shot-noise correction does not have an impact as significative as in the case of power spectrum and bispectrum because of the dominant sample variance error. In other words, the large statistical error associated with measuring the i-trispectrum from a less dense catalogue of tracers dominates over the shot-noise effect, at least up to the k_{\max} considered in this work.

D I-trispectrum covariance: Gaussian term in redshift space

Using the estimator defined in equation 2.16, the covariance matrix for the tracer field (halo or galaxy) i-trispectrum in redshift space is given by:

$$\begin{aligned}
& C_G^{\mathcal{T}^{(0)}\mathcal{T}^{(0)}}(k_1, k_2, k_3, k_4; k_a, k_b, k_c, k_d) = \\
&= \frac{V^4}{(2\pi)^{18} N_{1234}^q N_{abcd}^q} \prod_{i=1,a}^{4,d} \int_{V_{\mathbf{q}_i}} \delta^D(\mathbf{q}_{1234}) \delta^D(\mathbf{q}_{abcd}) \\
&\times \langle \delta_h^s(\mathbf{q}_1) \delta_h^s(\mathbf{q}_2) \delta_h^s(\mathbf{q}_3) \delta_h^s(\mathbf{q}_4) \delta_h^s(\mathbf{q}_a) \delta_h^s(\mathbf{q}_b) \delta_h^s(\mathbf{q}_c) \delta_h^s(\mathbf{q}_d) \rangle \\
&= \frac{k_f^{-12}}{(2\pi)^6 k_f^{-18} V_{1234}^q V_{abcd}^q} \prod_{i=1,a}^{4,d} \int_{V_{\mathbf{q}_i}} \delta^D(\mathbf{q}_{1234}) \delta^D(\mathbf{q}_{abcd}) \\
&\times (2\pi)^{12} \delta^D(\mathbf{q}_{1a}) \delta^D(\mathbf{q}_{2b}) \delta^D(\mathbf{q}_{c3}) \delta^D(\mathbf{q}_{4d}) P_h^s(\mathbf{q}_1) P_h^s(\mathbf{q}_2) P_h^s(\mathbf{q}_3) P_h^s(\mathbf{q}_4) + 23 \text{ perm.} \\
&= \frac{k_f^3 (2\pi)^6}{V_{1234}^{q,2}} \delta_{1a}^K \delta_{2b}^K \delta_{3c}^K \delta_{4d}^K \prod_{i=1}^4 \int_{V_{\mathbf{q}_i}} \delta^D(\mathbf{q}_{1234}) P_h^s(\mathbf{q}_1) P_h^s(\mathbf{q}_2) P_h^s(\mathbf{q}_3) P_h^s(\mathbf{q}_4) + 23 \text{ perm.} \\
&\approx \frac{(2\pi)^9}{V_s V_{1234}^q} \frac{R_{1234}}{3} \sum_{\substack{k_1, k_2, k_3, k_4 \\ k_1, k_3, k_2, k_4 \\ k_1, k_2, k_4, k_3}} \frac{1}{8\pi^2 \Delta D} \int_{D_{\min}}^{D_{\max}} dD \int_{-1}^{+1} d\mu_D \int_0^{2\pi} d\phi_{12} \int_0^{2\pi} d\psi \\
&\times P_h^s(k_1, \mu_1) P_h^s(k_2, \mu_2) P_h^s(k_3, \mu_3) P_h^s(k_4, \mu_4), \tag{D.1}
\end{aligned}$$

where we used the approximation made in [47] that $\delta^{D^2} \approx \frac{V_s}{(2\pi)^3} \delta^D = k_f^{-3} \delta^D$; P_h^s denotes the redshift space tracer (halo or galaxy) power spectrum, V_s is the survey volume and k_f the fundamental frequency; R_{1234} is a symmetry factor that counts the number of possible combinations of equal sides between the two identical quadrilaterals sets. Depending on the number of equal sides, R_{1234} assumes the values:

$$\mathbf{R}_{1234} = \begin{cases} 1 & \text{for } (k_a, k_b, k_c, k_d) \\ 2 & \text{for } (k_a, k_a, k_c, k_d) \\ 4 & \text{for } (k_a, k_a, k_c, k_c) \\ 6 & \text{for } (k_a, k_a, k_a, k_d) \\ 24 & \text{for } (k_a, k_a, k_a, k_a) . \end{cases} \quad (\text{D.2})$$

E Primordial non-Gaussianity

We recap here the formalism presented in the appendix of Ref. [36] for both power spectrum and bispectrum and extend it to include the i-trispectrum for the matter field in real space (replace the SPT kernels with the redshift space ones in appendix A for the redshift space case).

For the three statistics (power spectrum, bispectrum and i-trispectrum) we compute the contribution due to the presence of a primordial non-Gaussian component of the local type in the potential field. The primordial (subscript p) potential (which in our work has units of $[c^2]$ in order for equation E.6 appearing later to be dimensionless) can be thus parametrised as:

$$\Phi_{\text{p}}(\mathbf{x}) = \phi(\mathbf{x}) + \frac{f_{\text{nl}}}{c^2} [\phi^2(\mathbf{x}) - \langle \phi^2(\mathbf{x}) \rangle] + \frac{g_{\text{nl}}}{c^4} [\phi^3(\mathbf{x}) - 3\phi(\mathbf{x})\langle \phi^2(\mathbf{x}) \rangle] + \dots \quad (\text{E.1})$$

where ϕ represents a Gaussian field. In Fourier space it translates to:

$$\Phi_{\text{p}}(\mathbf{k}) = \phi_k + \frac{f_{\text{nl}}}{c^2} \left[I_{ab}^k \phi_a \phi_b - \delta^D(\mathbf{k}) \langle \phi^2 \rangle \right] + \frac{g_{\text{nl}}}{c^4} \left[I_{abc}^k \phi_a \phi_b \phi_c - \frac{3}{(2\pi)^3} \phi_k \langle \phi^2 \rangle \right], \quad (\text{E.2})$$

where in Fourier space $\langle \phi^2 \rangle = \int d\mathbf{q}^3 P^\phi(\mathbf{q}) = (2\pi)^3 \sigma_\phi^2$, and ϕ_k denotes the Fourier transform of ϕ and P^ϕ denotes the power spectrum of the ϕ field. In order to write in a compact way we write for different quantities the argument as a subscript (e.g., $P^\phi(k) \rightarrow P_k^\phi$ or $F^{(2)}[\mathbf{k}_a, \mathbf{k}_b] \rightarrow F_{ab}^{(2)}$). For the same reason to express many integrals appearing in the perturbation expansion we have introduced the short notation:

$$I_{ab}^k = \int \frac{d\mathbf{q}_a^3 d\mathbf{q}_b^3}{(2\pi)^3} \delta^D(\mathbf{k} - \mathbf{q}_a - \mathbf{q}_b) \quad \text{and} \quad I_{abc}^k = \int \frac{d\mathbf{q}_a^3 d\mathbf{q}_b^3 d\mathbf{q}_c^3}{(2\pi)^6} \delta^D(\mathbf{k} - \mathbf{q}_a - \mathbf{q}_b - \mathbf{q}_c). \quad (\text{E.3})$$

Late-time and primordial potentials are related by:

$$\Phi_{\text{l.t.}}(k, a) = \mathcal{O}(\Phi_{\text{p}}(k)) \simeq \frac{9}{10} \frac{D_+(a)}{a} \mathbb{T}(k) \Phi_{\text{p}}, \quad (\text{E.4})$$

where the operator \mathcal{O} describing the full non-linear evolution of the primordial field has been linearised in the last step, $D_+(a)$ is the linear growth factor as a function of the scale factor

a and $\mathbb{T}(k)$ is the transfer function. At late-times the potential field is related to the density perturbation variable by the Poisson equation:

$$\nabla^2 \Phi_{1,t.}(\mathbf{x}, a) = \frac{3}{2} \frac{\Omega_m H_0^2}{a} \delta(\mathbf{x}, a). \quad (\text{E.5})$$

This allows us to link the primordial potential with the late-time matter density perturbation assuming, as normally done in the literature, that only the linearly evolved component of the primordial (potentially including non-Gaussianities) field Φ_p sources the late time gravitational potential $\Phi_{1,t.}$:

$$\delta_k = \frac{3}{5} \frac{D_+}{\Omega_m H_0^2} k^2 \mathbb{T}_k \Phi_p = w \mathcal{M}_k \Phi_p \quad \text{where} \quad \mathcal{M}_k = \frac{3}{5} \frac{D_+}{\Omega_m H_0^2} k^2 \mathbb{T}_k. \quad (\text{E.6})$$

In the rest of this appendix, to use a more compact notation, the wave-vector or wave-number in the argument is reported as a subscript index.

E.1 Power spectrum

As described in [36] up to order ϕ^4 for the matter power spectrum we have the terms:

$$\begin{aligned} \langle \delta \delta \rangle &= \langle \delta^{(1)} \delta^{(1)} \rangle + 2 \langle \delta^{(1)} \delta^{(2)} \rangle + \langle \delta^{(2)} \delta^{(2)} \rangle + 2 \langle \delta^{(1)} \delta^{(3)} \rangle \\ &\equiv P_{(11)} + P_{(12)} + P_{(22)} + P_{(13)}. \end{aligned} \quad (\text{E.7})$$

The first term $P_{(11)}$ is given by

$$\langle \delta^{(1)}(\mathbf{k}) \delta^{(1)}(\mathbf{q}) \rangle = F_k^{(1)} F_q^{(1)} \mathcal{M}_k \mathcal{M}_q (2\pi)^3 \delta^D(\mathbf{k} + \mathbf{q}) \left\{ P_k^\phi + \frac{2f_{\text{nl}}^2}{c^4} \int \frac{d\mathbf{p}_a^3}{(2\pi)^3} P_a^\phi P_{|\mathbf{k}-\mathbf{p}_a|}^\phi \right\}. \quad (\text{E.8})$$

where $F^{(1)} = 1$ and we include it to simplify the transformation to the matter redshift space expressions, where $F^{(1)} \rightarrow Z^{(1)}$. Notice that the integral in the second term proportional to f_{nl}^2 is divergent for $k \rightarrow 0$. However these integrals should be performed for a k_{min} corresponding to the size of the causally connected patch of the Universe and therefore it is effectively a finite quantity.

The second term, $P_{(12)}$, reads

$$\begin{aligned} 2 \langle \delta^{(1)}(\mathbf{k}) \delta^{(2)}(\mathbf{q}) \rangle &= (2\pi)^3 \delta^D(\mathbf{k} + \mathbf{q}) \frac{4f_{\text{nl}}}{c^2} F_k^{(1)} \mathcal{M}_k \\ &\times \int \frac{d\mathbf{p}_a^3}{(2\pi)^3} \mathcal{M}_{p_a} \mathcal{M}_{|\mathbf{k}-\mathbf{p}_a|} F_{a,-\mathbf{k}-\mathbf{p}_a}^{(2)} P_{|\mathbf{k}-\mathbf{p}_a|}^\phi \left[P_a^\phi + 2P_k^\phi \right]. \end{aligned} \quad (\text{E.9})$$

The other terms in the power spectrum expansion, $P_{(22)}$ and $P_{(13)}$, are at first order already proportional to ϕ^4 and therefore in our case they just return the standard terms for the Gaussian initial conditions.

E.2 Bispectrum

Limiting the expansion in terms of the Gaussian primordial potential up to order ϕ^4 , as described in [36]'s appendix, for the bispectrum there is only a primordial term $B_{(111)}$ together with the standard one $B_{(112)}$ due to gravitational collapse. The expression for $B_{(111)}$ is given by

$$\begin{aligned}\langle \delta^{(1)} \delta^{(1)} \delta^{(1)} \rangle &= (2\pi)^3 F_{k_1}^{(1)} F_{k_2}^{(1)} F_{k_3}^{(1)} \mathcal{M}_{k_1} \mathcal{M}_{k_2} \mathcal{M}_{k_3} \frac{2f_{\text{nl}}}{c^2} \delta^D(\mathbf{k}_1 + \mathbf{k}_2 + \mathbf{k}_3) P_{k_2}^\phi P_{k_3}^\phi + \text{cyc.} \\ &= (2\pi)^3 \delta^D(\mathbf{k}_1 + \mathbf{k}_2 + \mathbf{k}_3) F_{k_1}^{(1)} F_{k_2}^{(1)} F_{k_3}^{(1)} \frac{\mathcal{M}_{k_1}}{\mathcal{M}_{k_2} \mathcal{M}_{k_3}} \frac{2f_{\text{nl}}}{c^2} P_{k_2}^{\text{m}} P_{k_3}^{\text{m}} + \text{cyc.},\end{aligned}\tag{E.10}$$

where in the last line the primordial power spectrum was converted into the late-time matter power spectrum.

E.3 Trispectrum

The terms we report here were presented (in a less pedagogical way) in [46] and [79]. In this subsection, for clarity and self-consistency, we also report them using a notation consistent with the rest of the paper. In the case of i-trispectrum, primordial corrections appear at order ϕ^6 at the lowest order in ϕ . By converting ϕ into the late time matter perturbation density variable δ , it can be noticed that this is the same order of the standard gravitational term for Gaussian initial conditions. It is indeed the lowest order at which the connected part of the four-point correlation function in Fourier Space appears. Therefore we will consider only terms of order ϕ^6 . Proceeding as before:

$$\begin{aligned}\langle \delta \delta \delta \delta \rangle &= \langle (\delta^{(1)} + \delta^{(2)} + \delta^{(3)} + O(\delta^{(4)})) (\delta^{(1)} + \delta^{(2)} + \delta^{(3)} + O(\delta^{(4)})) \\ &\quad \times (\delta^{(1)} + \delta^{(2)} + \delta^{(3)} + O(\delta^{(4)})) (\delta^{(1)} + \delta^{(2)} + \delta^{(3)} + O(\delta^{(4)})) \rangle \\ &= \langle \delta^{(1)} \delta^{(1)} \delta^{(1)} \delta^{(1)} \rangle + 4 \langle \delta^{(1)} \delta^{(1)} \delta^{(1)} \delta^{(2)} \rangle + 6 \langle \delta^{(1)} \delta^{(1)} \delta^{(2)} \delta^{(2)} \rangle + 4 \langle \delta^{(1)} \delta^{(1)} \delta^{(1)} \delta^{(3)} \rangle \\ &\equiv T_{(1111)} + T_{(1112)} + T_{(1122)} + T_{(1113)}.\end{aligned}\tag{E.11}$$

The i-trispectrum corresponding to Gaussian initial conditions is given by terms $T_{(1122)}$ and $T_{(1113)}$. Without PNG, $T_{(1111)}$ would represent the unconnected part of the four-point correlator in Fourier space. However expanding in terms of PNG results in non-trivial terms proportional to both f_{nl}^2 and g_{nl} . Finally $T_{(1112)}$ would be zero for Gaussian initial conditions since it is an odd moment. However with PNG, up to order ϕ^6 it will produce at least one term proportional to f_{nl} .

We will follow the approach of first expanding each expression in terms of late-time density perturbation variables δ_k and then express each of these in terms of early time potential field Φ_{p} using equation E.6. Finally we will convert Φ_{p} to its expansion in terms of the early-time Gaussian potential ϕ using equation E.2.

E.3.1 $T_{(1111)}$

$$\begin{aligned}
& \langle \delta^{(1)} \delta^{(1)} \delta^{(1)} \delta^{(1)} \rangle \\
& \propto \left\langle \left\{ \phi_{k_1} + \frac{f_{\text{nl}}}{c^2} \left[I_{ab}^{k_1} \phi_a \phi_b - \delta^D(\mathbf{k}_1) \langle \phi^2 \rangle \right] + \frac{g_{\text{nl}}}{c^4} \left[I_{cde}^{k_1} \phi_c \phi_d \phi_e - \frac{3}{(2\pi)^3} \phi_{k_1} \langle \phi^2 \rangle \right] \right\} \right. \\
& \times \left\{ \phi_{k_2} + \frac{f_{\text{nl}}}{c^2} \left[I_{fg}^{k_2} \phi_f \phi_g - \delta^D(\mathbf{k}_2) \langle \phi^2 \rangle \right] + \frac{g_{\text{nl}}}{c^4} \left[I_{hil}^{k_2} \phi_h \phi_i \phi_l - \frac{3}{(2\pi)^3} \phi_{k_2} \langle \phi^2 \rangle \right] \right\} \\
& \times \left\{ \phi_{k_3} + \frac{f_{\text{nl}}}{c^2} \left[I_{mn}^{k_3} \phi_m \phi_n - \delta^D(\mathbf{k}_3) \langle \phi^2 \rangle \right] + \frac{g_{\text{nl}}}{c^4} \left[I_{oqr}^{k_3} \phi_o \phi_q \phi_r - \frac{3}{(2\pi)^3} \phi_{k_3} \langle \phi^2 \rangle \right] \right\} \\
& \times \left. \left\{ \phi_{k_4} + \frac{f_{\text{nl}}}{c^2} \left[I_{st}^{k_4} \phi_s \phi_t - \delta^D(\mathbf{k}_4) \langle \phi^2 \rangle \right] + \frac{g_{\text{nl}}}{c^4} \left[I_{uvz}^{k_4} \phi_u \phi_v \phi_z - \frac{3}{(2\pi)^3} \phi_{k_4} \langle \phi^2 \rangle \right] \right\} \right\rangle
\end{aligned} \tag{E.12}$$

We then have two kind of PNG-dependent terms, one proportional to f_{nl}^2 and one to g_{nl} :

$$\begin{aligned}
& \langle \delta^{(1)} \delta^{(1)} \delta^{(1)} \delta^{(1)} \rangle = F_{k_1}^{(1)} F_{k_2}^{(1)} F_{k_3}^{(1)} F_{k_4}^{(1)} \mathcal{M}_{k_1} \mathcal{M}_{k_2} \mathcal{M}_{k_3} \mathcal{M}_{k_4} \\
& \times \left\{ \frac{f_{\text{nl}}^2}{c^4} \left[I_{mn}^{k_3} I_{st}^{k_4} \langle \phi_{k_1} \phi_{k_2} \phi_m \phi_n \phi_s \phi_t \rangle - I_{mn}^{k_3} \langle \phi_{k_1} \phi_{k_2} \phi_m \phi_n \rangle \delta^D(\mathbf{k}_4) \langle \phi^2 \rangle \right. \right. \\
& \left. \left. - I_{st}^{k_4} \langle \phi_{k_1} \phi_{k_2} \phi_s \phi_t \rangle \delta^D(\mathbf{k}_3) \langle \phi^2 \rangle + \langle \phi_{k_1} \phi_{k_2} \rangle \delta^D(\mathbf{k}_3) \delta^D(\mathbf{k}_4) \langle \phi^2 \rangle^2 \right] + 5 \text{ p.} \right. \\
& \left. + \frac{g_{\text{nl}}}{c^4} \left[I_{uvz}^{k_4} \langle \phi_{k_1} \phi_{k_2} \phi_{k_3} \phi_u \phi_v \phi_z \rangle - 3 \langle \phi_{k_1} \phi_{k_2} \phi_{k_3} \phi_{k_4} \rangle \langle \phi^2 \rangle \right] + 3 \text{ p.} \right\}.
\end{aligned} \tag{E.13}$$

Given the several permutations let us split this computation in two terms proportional to the two PNG parameters. Proceeding with the first, $T_{(1111)}^{f_{\text{nl}}^2}$, we can see that the six-point correlator can be decomposed in the following terms:

$$T_{(1111)}^{f_{\text{nl}}^2} \propto \begin{cases} \langle \phi_{k_1} \phi_{k_2} \rangle \langle \phi_m \phi_n \rangle \langle \phi_s \phi_t \rangle \\ \langle \phi_{k_1} \phi_{k_2} \rangle \langle \phi_m \phi_s \rangle \langle \phi_n \phi_t \rangle \times 2 \\ (\langle \phi_{k_1} \phi_{k_m} \rangle \langle \phi_2 \phi_n \rangle \langle \phi_s \phi_t \rangle + \langle \phi_{k_1} \phi_{k_s} \rangle \langle \phi_2 \phi_t \rangle \langle \phi_m \phi_n \rangle) \times 2 \\ \langle \phi_{k_1} \phi_{k_m} \rangle \langle \phi_2 \phi_s \rangle \langle \phi_n \phi_t \rangle \times 4 + 1 \text{ p. } (k_1 \longleftrightarrow k_2) \end{cases} \tag{E.14}$$

The symmetry factors are due to permutations over the auxiliary variables. Only the last term is fully connected, therefore we expect the others to be cancelled out by the other three terms appearing in the expression for $T_{(1111)}^{f_{\text{nl}}^2}$. Let us find out:

$$\begin{aligned}
T_{(1111)}^{f_{nl}^2} &\propto \left\{ I_{mn}^{k_3} I_{st}^{k_4} \langle \phi_{k_1} \phi_{k_2} \rangle \langle \phi_m \phi_n \rangle \langle \phi_s \phi_t \rangle + 2 I_{mn}^{k_3} I_{st}^{k_4} \langle \phi_{k_1} \phi_{k_2} \rangle \langle \phi_m \phi_s \rangle \langle \phi_n \phi_t \rangle \right. \\
&+ 2 I_{mn}^{k_3} I_{st}^{k_4} [\langle \phi_{k_1} \phi_{k_m} \rangle \langle \phi_{k_2} \phi_n \rangle \langle \phi_s \phi_t \rangle + \langle \phi_{k_1} \phi_{k_s} \rangle \langle \phi_{k_2} \phi_t \rangle \langle \phi_m \phi_n \rangle] \\
&+ 4 I_{mn}^{k_3} I_{st}^{k_4} [\langle \phi_{k_1} \phi_{k_m} \rangle \langle \phi_{k_2} \phi_s \rangle \langle \phi_n \phi_t \rangle + \langle \phi_{k_1} \phi_{k_s} \rangle \langle \phi_{k_2} \phi_m \rangle \langle \phi_n \phi_t \rangle] \\
&- I_{mn}^{k_3} \delta^D(\mathbf{k}_4) [\langle \phi_{k_1} \phi_{k_2} \rangle \langle \phi_m \phi_n \rangle \langle \phi^2 \rangle + 2 \langle \phi_{k_1} \phi_m \rangle \langle \phi_{k_2} \phi_n \rangle \langle \phi^2 \rangle] \\
&\left. - I_{st}^{k_4} \delta^D(\mathbf{k}_3) [\langle \phi_{k_1} \phi_{k_2} \rangle \langle \phi_s \phi_t \rangle \langle \phi^2 \rangle + 2 \langle \phi_{k_1} \phi_s \rangle \langle \phi_{k_2} \phi_t \rangle \langle \phi^2 \rangle] + \delta^D(\mathbf{k}_3) \delta^D(\mathbf{k}_4) \langle \phi_{k_1} \phi_{k_2} \rangle \langle \phi^2 \rangle^2 \right\} \\
&= \cancel{(2\pi)^3 \delta^D(\mathbf{k}_{12}) P_{k_1}^\phi \delta^D(\mathbf{k}_3) \delta^D(\mathbf{k}_4) \langle \phi^2 \rangle^2} + 2(2\pi)^3 \delta^D(\mathbf{k}_{12}) \delta^D(\mathbf{k}_{34}) P_{k_1}^\phi \int d\mathbf{p}_m^3 P_m^\phi P_{|\mathbf{k}_4+\mathbf{p}_m|}^\phi \\
&+ 2(2\pi)^3 P_{k_1}^\phi P_{k_2}^\phi \langle \phi^2 \rangle \left[\delta^D(\mathbf{k}_{123}) \delta^D(\mathbf{k}_4) + \delta^D(\mathbf{k}_{124}) \delta^D(\mathbf{k}_3) \right] \\
&+ 4(2\pi)^3 \delta^D(\mathbf{k}_{1234}) P_{k_1}^\phi P_{k_2}^\phi \left[P_{|\mathbf{k}_1+\mathbf{k}_3|}^\phi + P_{|\mathbf{k}_1+\mathbf{k}_4|}^\phi \right] \\
&- (2\pi)^3 \left[\cancel{\delta^D(\mathbf{k}_{12}) \delta^D(\mathbf{k}_3) \delta^D(\mathbf{k}_4) P_{k_1}^\phi \langle \phi^2 \rangle^2} + 2 \delta^D(\mathbf{k}_{123}) \delta^D(\mathbf{k}_4) P_{k_1}^\phi P_{k_2}^\phi \langle \phi^2 \rangle \right] \\
&- (2\pi)^3 \left[\cancel{\delta^D(\mathbf{k}_{12}) \delta^D(\mathbf{k}_4) \delta^D(\mathbf{k}_3) P_{k_1}^\phi \langle \phi^2 \rangle^2} + 2 \delta^D(\mathbf{k}_{124}) \delta^D(\mathbf{k}_3) P_{k_1}^\phi P_{k_2}^\phi \langle \phi^2 \rangle \right] \\
&+ \cancel{(2\pi)^3 \delta^D(\mathbf{k}_{12}) \delta^D(\mathbf{k}_3) \delta^D(\mathbf{k}_4) P_{k_1}^\phi \langle \phi^2 \rangle^2} \\
&= 2(2\pi)^3 \delta^D(\mathbf{k}_{12}) \delta^D(\mathbf{k}_{34}) P_{k_1}^\phi \int d\mathbf{p}_m^3 P_m^\phi P_{|\mathbf{k}_4+\mathbf{p}_m|}^\phi + 4(2\pi)^3 \delta^D(\mathbf{k}_{1234}) P_{k_1}^\phi P_{k_2}^\phi \left[P_{|\mathbf{k}_1+\mathbf{k}_3|}^\phi + P_{|\mathbf{k}_1+\mathbf{k}_4|}^\phi \right]
\end{aligned} \tag{E.15}$$

From the last line we can see that one term did not cancel out (first one). However this represents (as it can be seen from the Dirac's deltas) an unconnected part of the four-point correlation function. It is indeed the primordial contribution to the power spectrum reported in equation E.8.

From the Dirac deltas appearing in the above computation we also notice that for first part of the connected term $\mathbf{k}_m = -\mathbf{k}_1$, $\mathbf{k}_s = -\mathbf{k}_2$, $\mathbf{k}_n = \mathbf{k}_1 + \mathbf{k}_3$ and $\mathbf{k}_t = \mathbf{k}_2 + \mathbf{k}_4$. For the second one we have the relations $\mathbf{k}_s = -\mathbf{k}_1$, $\mathbf{k}_m = -\mathbf{k}_2$, $\mathbf{k}_n = \mathbf{k}_1 + \mathbf{k}_4$ and $\mathbf{k}_t = \mathbf{k}_2 + \mathbf{k}_3$.

We can now focus on the other term, $T_{(1111)}^{g_{nl}}$:

$$T_{(1111)}^{g_{nl}} \propto \left\{ (\langle \phi_{k_1} \phi_{k_2} \rangle \langle \phi_{k_3} \phi_u \rangle \langle \phi_v \phi_z \rangle + 2 \text{p.}) \times 3 \right. \tag{E.16}$$

$$\left. \langle \phi_{k_1} \phi_u \rangle \langle \phi_{k_2} \phi_v \rangle \langle \phi_{k_3} \phi_z \rangle \times 6 \right.$$

The first term can be easily spotted to be unconnected and should cancel out:

$$\begin{aligned}
T_{(1111)}^{g_{\text{nl}}} &\propto \left\{ I_{uvz}^{k_4} [3 (\langle \phi_{k_1} \phi_{k_2} \rangle \langle \phi_{k_3} \phi_u \rangle \langle \phi_v \phi_z \rangle + 2 \text{p.}) + 6 \langle \phi_{k_1} \phi_u \rangle \langle \phi_{k_2} \phi_v \rangle \langle \phi_{k_3} \phi_z \rangle] \right. \\
&\quad \left. - \frac{3}{(2\pi)^3} [\langle \phi_{k_1} \phi_{k_2} \rangle \langle \phi_{k_3} \phi_{k_4} \rangle \langle \phi^2 \rangle + 2 \text{p.}] \right\} \\
&= 3 \left[\delta^D(\mathbf{k}_{12}) \delta^D(\mathbf{k}_{34}) (2\pi)^3 P_{k_1}^\phi P_{k_3}^\phi \int d\mathbf{p}_v^3 P_v^\phi + 2 \text{p.} \right] + 6(2\pi)^3 \delta^D(\mathbf{k}_{1234}) P_{k_1}^\phi P_{k_2}^\phi P_{k_3}^\phi \\
&\quad - \frac{3}{(2\pi)^3} \left[(2\pi)^6 \delta^D(\mathbf{k}_{12}) \delta^D(\mathbf{k}_{34}) (2\pi)^3 P_{k_1}^\phi P_{k_3}^\phi \langle \phi^2 \rangle + 2 \text{p.} \right] \\
&= 6(2\pi)^3 \delta^D(\mathbf{k}_{1234}) P_{k_1}^\phi P_{k_2}^\phi P_{k_3}^\phi . \tag{E.17}
\end{aligned}$$

From the Dirac deltas appearing in the above computation we also notice that for the connected term $\mathbf{k}_u = -\mathbf{k}_1$, $\mathbf{k}_v = -\mathbf{k}_2$ and $\mathbf{k}_z = -\mathbf{k}_3$.

We can plug the results of equations E.15 and E.17 into the full expression of equation E.13:

$$\begin{aligned}
T_{(1111)} &= F_{k_1}^{(1)} F_{k_2}^{(1)} F_{k_3}^{(1)} F_{k_4}^{(1)} \mathcal{M}_{k_1} \mathcal{M}_{k_2} \mathcal{M}_{k_3} \mathcal{M}_{k_4} \\
&\times \left\{ \frac{f_{\text{nl}}^2}{c^4} 4 P_{k_1}^\phi P_{k_2}^\phi \left[P_{|\mathbf{k}_1+\mathbf{k}_3|}^\phi + P_{|\mathbf{k}_1+\mathbf{k}_4|}^\phi \right] + 5 \text{p.} + \frac{g_{\text{nl}}}{c^4} \left[6 P_{k_1}^\phi P_{k_2}^\phi P_{k_3}^\phi + 3 \text{p.} \right] \right\}. \tag{E.18}
\end{aligned}$$

Basically the PNG terms $T_{(1111)}^{f_{\text{nl}}}$ and $T_{(1111)}^{g_{\text{nl}}}$ are respectively the equivalent of the terms $T_{(1122)}$ and $T_{(1113)}$ for the Gaussian initial condition due to gravitational non-linear evolution.

As last step we express the above result in terms of the late-time matter power spectrum using equation E.6.

$$\begin{aligned}
T_{(1111)} &= F_{k_1}^{(1)} F_{k_2}^{(1)} F_{k_3}^{(1)} F_{k_4}^{(1)} \mathcal{M}_{k_1} \mathcal{M}_{k_2} \mathcal{M}_{k_3} \mathcal{M}_{k_4} \\
&\times \left\{ \frac{f_{\text{nl}}^2}{c^4} 4 P_{k_1}^\phi P_{k_2}^\phi \left[P_{|\mathbf{k}_1+\mathbf{k}_3|}^\phi + P_{|\mathbf{k}_1+\mathbf{k}_4|}^\phi \right] + 5 \text{ p.} + \frac{g_{\text{nl}}}{c^4} \left[6 P_{k_1}^\phi P_{k_2}^\phi P_{k_3}^\phi + 3 \text{ p.} \right] \right\} \\
&= F_{k_1}^{(1)} F_{k_2}^{(1)} F_{k_3}^{(1)} F_{k_4}^{(1)} \mathcal{M}_{k_1} \mathcal{M}_{k_2} \mathcal{M}_{k_3} \mathcal{M}_{k_4} \\
&\times \left\{ \frac{f_{\text{nl}}^2}{c^4} 4 \frac{P_{k_1}^m P_{k_2}^m}{\mathcal{M}_{k_1}^2 \mathcal{M}_{k_2}^2} \left[\frac{P_{|\mathbf{k}_1+\mathbf{k}_3|}^m}{\mathcal{M}_{|\mathbf{k}_1+\mathbf{k}_3|}^2} + \frac{P_{|\mathbf{k}_1+\mathbf{k}_4|}^m}{\mathcal{M}_{|\mathbf{k}_1+\mathbf{k}_4|}^2} \right] + 5 \text{ p.} + \frac{g_{\text{nl}}}{c^4} \left[6 \frac{P_{k_1}^m P_{k_2}^m P_{k_3}^m}{\mathcal{M}_{k_1}^2 \mathcal{M}_{k_2}^2 \mathcal{M}_{k_3}^2} + 3 \text{ p.} \right] \right\} \\
&= F_{k_1}^{(1)} F_{k_2}^{(1)} F_{k_3}^{(1)} F_{k_4}^{(1)} \\
&\times \left\{ \frac{f_{\text{nl}}^2}{c^4} 4 \frac{\mathcal{M}_{k_3} \mathcal{M}_{k_4}}{\mathcal{M}_{k_1} \mathcal{M}_{k_2}} P_{k_1}^m P_{k_2}^m \left[\frac{P_{|\mathbf{k}_1+\mathbf{k}_3|}^m}{\mathcal{M}_{|\mathbf{k}_1+\mathbf{k}_3|}^2} + \frac{P_{|\mathbf{k}_1+\mathbf{k}_4|}^m}{\mathcal{M}_{|\mathbf{k}_1+\mathbf{k}_4|}^2} \right] + 5 \text{ p.} + \frac{g_{\text{nl}}}{c^4} \left[6 \mathcal{M}_{k_4} \frac{P_{k_1}^m P_{k_2}^m P_{k_3}^m}{\mathcal{M}_{k_1} \mathcal{M}_{k_2} \mathcal{M}_{k_3}} + 3 \text{ p.} \right] \right\}.
\end{aligned} \tag{E.19}$$

E.3.2 $T_{(1112)}$

This is perhaps the most interesting PNG term of the i-trispectrum, since, as $B_{(111)}$ for the bispectrum, it comes from a correlator that would be null for Gaussian initial conditions.

$$\begin{aligned}
\langle \delta^{(1)} \delta^{(1)} \delta^{(1)} \delta^{(2)} \rangle &= \langle F_{k_1}^{(1)} F_{k_2}^{(1)} F_{k_3}^{(1)} \mathcal{M}_{k_1} \mathcal{M}_{k_2} \mathcal{M}_{k_3} \mathcal{M}_{k_x} \mathcal{M}_{k_y} I_{xy}^{k_4} F_{xy}^{(2)} \rangle \\
&\times \left\{ \phi_{k_1} + \frac{f_{\text{nl}}}{c^2} \left[I_{ab}^{k_1} \phi_a \phi_b - \delta^D(\mathbf{k}_1) \langle \phi^2 \rangle \right] + \frac{g_{\text{nl}}}{c^4} \left[I_{cde}^{k_1} \phi_c \phi_d \phi_e - \frac{3}{(2\pi)^3} \phi_{k_1} \langle \phi^2 \rangle \right] \right\} \\
&\times \left\{ \phi_{k_2} + \frac{f_{\text{nl}}}{c^2} \left[I_{fg}^{k_2} \phi_f \phi_g - \delta^D(\mathbf{k}_2) \langle \phi^2 \rangle \right] + \frac{g_{\text{nl}}}{c^4} \left[I_{hil}^{k_2} \phi_h \phi_i \phi_l - \frac{3}{(2\pi)^3} \phi_{k_2} \langle \phi^2 \rangle \right] \right\} \\
&\times \left\{ \phi_{k_3} + \frac{f_{\text{nl}}}{c^2} \left[I_{mn}^{k_3} \phi_m \phi_n - \delta^D(\mathbf{k}_3) \langle \phi^2 \rangle \right] + \frac{g_{\text{nl}}}{c^4} \left[I_{oqr}^{k_3} \phi_o \phi_q \phi_r - \frac{3}{(2\pi)^3} \phi_{k_3} \langle \phi^2 \rangle \right] \right\} \\
&\times \left\{ \phi_x + \frac{f_{\text{nl}}}{c^2} \left[I_{st}^x \phi_s \phi_t - \delta^D(\mathbf{p}_x) \langle \phi^2 \rangle \right] + \frac{g_{\text{nl}}}{c^4} \left[I_{uvz}^x \phi_u \phi_v \phi_z - \frac{3}{(2\pi)^3} \phi_x \langle \phi^2 \rangle \right] \right\} \\
&\times \left\{ \phi_y + \frac{f_{\text{nl}}}{c^2} \left[I_{\epsilon\zeta}^y \phi_\epsilon \phi_\zeta - \delta^D(\mathbf{p}_y) \langle \phi^2 \rangle \right] + \frac{g_{\text{nl}}}{c^4} \left[I_{\eta\lambda\tau}^y \phi_\eta \phi_\lambda \phi_\tau - \frac{3}{(2\pi)^3} \phi_y \langle \phi^2 \rangle \right] \right\} \\
&+ 3 \text{ p.}
\end{aligned} \tag{E.20}$$

There are two possible terms proportional to f_{nl} from the above expansion. The first corresponds to the f_{nl} associated to a $\delta^{(1)}$, the second to that associated to $\delta^{(2)}$.

$$\begin{aligned}
T_{(1112)} &= F_{k_1}^{(1)} F_{k_2}^{(1)} F_{k_3}^{(1)} \mathcal{M}_{k_1} \mathcal{M}_{k_2} \mathcal{M}_{k_3} \mathcal{M}_{k_x} \mathcal{M}_{k_y} I_{xy}^{k_4} F_{xy}^{(2)} \frac{f_{nl}}{c^2} \\
&\times \left\{ \left[I_{ab}^{k_1} \langle \phi_a \phi_b \phi_{k_2} \phi_{k_3} \phi_x \phi_y \rangle - \delta^D(\mathbf{k}_1) \langle \phi_{k_2} \phi_{k_3} \phi_x \phi_y \rangle \langle \phi^2 \rangle + 2 \text{p.} \right] \right. \\
&\left. + 2 \left[I_{st}^x \langle \phi_{k_1} \phi_{k_2} \phi_{k_3} \phi_s \phi_t \phi_y \rangle - \delta^D(\mathbf{p}_x) \langle \phi_{k_1} \phi_{k_2} \phi_{k_3} \phi_y \rangle \langle \phi^2 \rangle \right] \right\}, \tag{E.21}
\end{aligned}$$

where the two permutations in the second line correspond to expanding \mathbf{k}_2 or \mathbf{k}_3 instead of \mathbf{k}_1 . Proceed step by step we now analyse the two terms separately, namely $T_{(1112)}^a$ and $T_{(1112)}^b$. Starting from the first:

$$T_{(1112)}^a \propto \begin{cases} \langle \phi_a \phi_b \rangle \langle \phi_{k_2} \phi_{k_3} \rangle \langle \phi_x \phi_y \rangle \\ \langle \phi_a \phi_{k_2} \rangle \langle \phi_b \phi_{k_3} \rangle \langle \phi_x \phi_y \rangle \times 2 \\ \langle \phi_a \phi_b \rangle \langle \phi_{k_2} \phi_x \rangle \langle \phi_{k_3} \phi_y \rangle \times 2 \\ \langle \phi_a \phi_x \rangle \langle \phi_{k_2} \phi_{k_3} \rangle \langle \phi_b \phi_y \rangle \times 2 \\ \langle \phi_a \phi_{k_2} \rangle \langle \phi_x \phi_{k_3} \rangle \langle \phi_b \phi_y \rangle \times 4 + 1 \text{p. } (k_2 \longleftrightarrow k_3) \end{cases} \tag{E.22}$$

In order to proceed as generally as possible, we need to separately treat the combinations arising from the mixing between original wave vectors \mathbf{k}_i with auxiliary ones \mathbf{p}_j originating from different sources (equation E.20).

$$\begin{aligned}
T_{(1112)}^a &\propto \left\{ I_{xy}^{k_4} I_{ab}^{k_1} F_{xy}^{(2)} \langle \phi_a \phi_b \rangle \langle \phi_{k_2} \phi_{k_3} \rangle \langle \phi_x \phi_y \rangle + 2 I_{xy}^{k_4} I_{ab}^{k_1} F_{xy}^{(2)} \langle \phi_a \phi_{k_2} \rangle \langle \phi_b \phi_{k_3} \rangle \langle \phi_x \phi_y \rangle \right. \\
&+ 2 I_{xy}^{k_4} I_{ab}^{k_1} F_{xy}^{(2)} \langle \phi_a \phi_b \rangle \langle \phi_{k_2} \phi_x \rangle \langle \phi_{k_3} \phi_y \rangle + 2 I_{xy}^{k_4} I_{ab}^{k_1} F_{xy}^{(2)} \langle \phi_a \phi_x \rangle \langle \phi_{k_2} \phi_{k_3} \rangle \langle \phi_b \phi_y \rangle \\
&+ \left[4 I_{xy}^{k_4} I_{ab}^{k_1} F_{xy}^{(2)} \langle \phi_a \phi_{k_2} \rangle \langle \phi_x \phi_{k_3} \rangle \langle \phi_b \phi_y \rangle + k_2 \longleftrightarrow k_3 \right] \\
&\left. - \delta^D(\mathbf{k}_1) \langle \phi^2 \rangle I_{xy}^{k_4} F_{xy}^{(2)} [\langle \phi_{k_2} \phi_{k_3} \rangle \langle \phi_x \phi_y \rangle + 2 \langle \phi_{k_2} \phi_x \rangle \langle \phi_{k_3} \phi_y \rangle] \right\} + 2 \text{ p.} \\
&= (2\pi)^3 \delta^D(\mathbf{k}_{23}) \delta^D(\mathbf{k}_1) \delta^D(\mathbf{k}_4) P_{k_2}^\phi \langle \phi^2 \rangle^2 C_b + 2(2\pi)^3 \delta^D(\mathbf{k}_{123}) \delta^D(\mathbf{k}_4) P_{k_2}^\phi P_{k_3}^\phi \langle \phi^2 \rangle C_b \\
&+ 2(2\pi)^3 \delta^D(\mathbf{k}_{234}) \delta^D(\mathbf{k}_1) P_{k_2}^\phi P_{k_3}^\phi F_{k_2 k_3}^{(2)} \langle \phi^2 \rangle \\
&+ 2(2\pi)^3 \delta^D(\mathbf{k}_{23}) \delta^D(\mathbf{k}_{14}) P_{k_2}^\phi \int d\mathbf{p}_x^3 P_x^\phi P_{|\mathbf{k}_4 - \mathbf{p}_x|}^\phi F^{(2)}[\mathbf{p}_x, \mathbf{k}_4 - \mathbf{p}_x] \\
&+ 4(2\pi)^3 \delta^D(\mathbf{k}_{1234}) P_{k_2}^\phi P_{k_3}^\phi P_{|\mathbf{k}_3 + \mathbf{k}_4|}^\phi F^{(2)}[-\mathbf{k}_3, \mathbf{k}_3 + \mathbf{k}_4] + k_2 \longleftrightarrow k_3 \\
&- \delta^D(\mathbf{k}_1) \langle \phi^2 \rangle (2\pi)^3 \left[\delta^D(\mathbf{k}_{23}) P_{k_2}^\phi \delta^D(\mathbf{k}_4) \langle \phi^2 \rangle C_b + 2(2\pi)^3 \delta^D(\mathbf{k}_{234}) F_{k_2 k_3}^{(2)} P_{k_2}^\phi P_{k_3}^\phi \langle \phi^2 \rangle \right] + 2 \text{ p.} \\
&= \left\{ 2(2\pi)^3 \left[\delta^D(\mathbf{k}_{123}) \delta^D(\mathbf{k}_4) P_{k_2}^\phi P_{k_3}^\phi \langle \phi^2 \rangle C_b + \delta^D(\mathbf{k}_{23}) \delta^D(\mathbf{k}_{14}) P_{k_2}^\phi \int d\mathbf{p}_x^3 P_x^\phi P_{|\mathbf{k}_4 - \mathbf{p}_x|}^\phi F^{(2)}[\mathbf{p}_x, \mathbf{k}_4 - \mathbf{p}_x] \right] \right. \\
&\left. + 4(2\pi)^3 \delta^D(\mathbf{k}_{1234}) P_{k_2}^\phi P_{k_3}^\phi P_{|\mathbf{k}_3 + \mathbf{k}_4|}^\phi F^{(2)}[-\mathbf{k}_3, \mathbf{k}_3 + \mathbf{k}_4] + k_2 \longleftrightarrow k_3 \right\} + 2 \text{ p.}
\end{aligned} \tag{E.23}$$

The constant $C_b = F^{(2)}[\mathbf{q}, -\mathbf{q}] = b_2/2 + b_{s^2}/3$ derives from the second order kernel including redshift space distortions in the case of opposite k -vectors. Only the term in the second line represents a connected part of the initial four-point correlator. From the Dirac deltas resulting in the connected part we can notice that $\mathbf{k}_x = -\mathbf{k}_3$ and $\mathbf{k}_y = \mathbf{k}_3 + \mathbf{k}_4$. This is a clear example of mode coupling between non-linear evolution and primordial non-Gaussian initial conditions. Moving to the second term $T_{(1112)}^b$:

$$T_{(1112)}^b \propto \begin{cases} \langle \phi_{k_1} \phi_{k_2} \rangle \langle \phi_{k_3} \phi_y \rangle \langle \phi_s \phi_t \rangle + 2 \text{ p.} \\ \langle \phi_{k_1} \phi_{k_2} \rangle \langle \phi_t \phi_{k_3} \rangle \langle \phi_s \phi_y \rangle \times 2 + 2 \text{ p.} \\ \langle \phi_{k_1} \phi_s \rangle \langle \phi_{k_2} \phi_t \rangle \langle \phi_{k_3} \phi_y \rangle \times 2 + 2 \text{ p.} \end{cases} \tag{E.24}$$

Which then expanded becomes:

$$\begin{aligned}
T_{(1112)}^b &\propto \left\{ \left[I_{xy}^{k_4} I_{st}^x F_{xy}^{(2)} \langle \phi_{k_1} \phi_{k_2} \rangle \langle \phi_{k_3} \phi_y \rangle \langle \phi_s \phi_t \rangle + 2 \text{p.} \right] \right. \\
&+ \left[2 I_{xy}^{k_4} I_{st}^x F_{xy}^{(2)} \langle \phi_{k_1} \phi_{k_2} \rangle \langle \phi_t \phi_{k_3} \rangle \langle \phi_s \phi_y \rangle + 2 \text{p.} \right] + \left[2 I_{xy}^{k_4} I_{st}^x F_{xy}^{(2)} \langle \phi_{k_1} \phi_s \rangle \langle \phi_{k_2} \phi_t \rangle \langle \phi_{k_3} \phi_y \rangle + 2 \text{p.} \right] \\
&\left. - \left[\delta^D(\mathbf{p}_x) I_{xy}^{k_4} F_{xy}^{(2)} \langle \phi_{k_1} \phi_{k_2} \rangle \langle \phi_{k_3} \phi_y \rangle \langle \phi^2 \rangle + 2 \text{p.} \right] \right\} \\
&= \left[(2\pi)^3 \delta^D(\mathbf{k}_{12}) \delta^D(\mathbf{k}_{34}) P_{k_2}^\phi P_{k_3}^\phi F^{(2)}[\mathbf{k}_4 + \mathbf{k}_3, -\mathbf{k}_3] \langle \phi^2 \rangle + 2 \text{p.} \right] \\
&+ \left[(2\pi)^3 \delta^D(\mathbf{k}_{12}) \delta^D(\mathbf{k}_{34}) P_{k_2}^\phi P_{k_3}^\phi \int d\mathbf{p}_y^3 F^{(2)}[\mathbf{k}_4 - \mathbf{p}_y, \mathbf{p}_y] P_y^\phi + 2 \text{p.} \right] \times 2 \\
&+ \left[(2\pi)^3 P_{k_1}^\phi P_{k_2}^\phi P_{k_3}^\phi \delta^D(\mathbf{k}_{1234}) F^{(2)}[\mathbf{k}_3 + \mathbf{k}_4, -\mathbf{k}_3] + 2 \text{p.} \right] \times 2 \\
&- \left[(2\pi)^3 P_{k_2}^\phi P_{k_3}^\phi \delta^D(\mathbf{k}_{12}) \delta^D(\mathbf{k}_{34}) F^{(2)}[\mathbf{k}_3 + \mathbf{k}_4, -\mathbf{k}_3] \langle \phi^2 \rangle + 2 \text{p.} \right] \\
&= \left[(2\pi)^3 \delta^D(\mathbf{k}_{12}) \delta^D(\mathbf{k}_{34}) P_{k_2}^\phi P_{k_3}^\phi \int d\mathbf{p}_y^3 F^{(2)}[\mathbf{k}_4 - \mathbf{p}_y, \mathbf{p}_y] P_y^\phi + 2 \text{p.} \right] \times 2 \\
&+ \left[(2\pi)^3 P_{k_1}^\phi P_{k_2}^\phi P_{k_3}^\phi \delta^D(\mathbf{k}_{1234}) F^{(2)}[\mathbf{k}_3 + \mathbf{k}_4, -\mathbf{k}_3] + 2 \text{p.} \right] \times 2,
\end{aligned} \tag{E.25}$$

where all the permutations above consist in changing \mathbf{k}_3 with either \mathbf{k}_1 or \mathbf{k}_2 . Only the second term represents a connected part of the initial four-point correlator. From the Dirac deltas resulting in the connected part we can notice that $\mathbf{k}_y = -\mathbf{k}_3$ and $\mathbf{k}_x = \mathbf{k}_3 + \mathbf{k}_4$. We can now proceed with equation E.21, using only the connected terms from $T_{(1112)}^a$ and $T_{(1112)}^b$:

$$\begin{aligned}
T_{(1112)} &= 2F_{k_1}^{(1)} F_{k_2}^{(1)} F_{k_3}^{(1)} \mathcal{M}_{k_1} \mathcal{M}_{k_2} \mathcal{M}_{k_3} \frac{f_{\text{nl}}}{c^2} \\
&\times \left\{ \left[2\mathcal{M}_{k_3} \mathcal{M}_{|\mathbf{k}_3+\mathbf{k}_4|} P_{k_2}^\phi P_{k_3}^\phi P_{|\mathbf{k}_3+\mathbf{k}_4|}^\phi F^{(2)} [-\mathbf{k}_3, \mathbf{k}_3 + \mathbf{k}_4] + k_2 \longleftrightarrow k_3 \right] + 2 \text{ p.} \right. \\
&+ \left. \left[\mathcal{M}_{k_3} \mathcal{M}_{|\mathbf{k}_3+\mathbf{k}_4|} P_{k_1}^\phi P_{k_2}^\phi P_{k_3}^\phi F^{(2)} [\mathbf{k}_3 + \mathbf{k}_4, -\mathbf{k}_3] + 2 \text{ p.} \right] \right\} + 3 \text{ p.} \\
&= 2F_{k_1}^{(1)} F_{k_2}^{(1)} F_{k_3}^{(1)} \mathcal{M}_{k_1} \mathcal{M}_{k_2} \mathcal{M}_{k_3} \frac{f_{\text{nl}}}{c^2} \\
&\times \left\{ \left[2\mathcal{M}_{k_3} \mathcal{M}_{|\mathbf{k}_3+\mathbf{k}_4|} P_{k_2}^\phi P_{k_3}^\phi P_{|\mathbf{k}_3+\mathbf{k}_4|}^\phi F^{(2)} [-\mathbf{k}_3, \mathbf{k}_3 + \mathbf{k}_4] + 5 \text{ p.} \right] \right. \\
&+ \left. \left[\mathcal{M}_{k_3} \mathcal{M}_{|\mathbf{k}_3+\mathbf{k}_4|} P_{k_1}^\phi P_{k_2}^\phi P_{k_3}^\phi F^{(2)} [\mathbf{k}_3 + \mathbf{k}_4, -\mathbf{k}_3] + 2 \text{ p.} \right] \right\} + 3 \text{ p.} .
\end{aligned} \tag{E.26}$$

As a final step we can convert the above result into an expression in terms of the late-time matter power spectrum using equation E.6

$$\begin{aligned}
T_{(1112)} &= \frac{f_{\text{nl}}}{c^2} F_{k_1}^{(1)} F_{k_2}^{(1)} F_{k_3}^{(1)} \\
&\times \left\{ \left[\mathcal{M}_{k_1} \mathcal{M}_{k_2} \mathcal{M}_{k_3}^2 \mathcal{M}_{|\mathbf{k}_3+\mathbf{k}_4|} P_{k_2}^\phi P_{k_3}^\phi P_{|\mathbf{k}_3+\mathbf{k}_4|}^\phi F^{(2)} [-\mathbf{k}_3, \mathbf{k}_3 + \mathbf{k}_4] + 5 \text{ p.} \right] \right. \\
&+ \left. \left[2\mathcal{M}_{k_1} \mathcal{M}_{k_2} \mathcal{M}_{k_3}^2 \mathcal{M}_{|\mathbf{k}_3+\mathbf{k}_4|} P_{k_1}^\phi P_{k_2}^\phi P_{k_3}^\phi F^{(2)} [\mathbf{k}_3 + \mathbf{k}_4, -\mathbf{k}_3] + 2 \text{ p.} \right] \right\} + 3 \text{ p.} \\
&= \frac{f_{\text{nl}}}{c^2} F_{k_1}^{(1)} F_{k_2}^{(1)} F_{k_3}^{(1)} \\
&\times \left\{ \left[4 \frac{\mathcal{M}_{k_1}}{\mathcal{M}_{k_2}} P_{k_2}^m P_{k_3}^m \frac{P_{|\mathbf{k}_3+\mathbf{k}_4|}^m}{\mathcal{M}_{|\mathbf{k}_3+\mathbf{k}_4|}} F^{(2)} [-\mathbf{k}_3, \mathbf{k}_3 + \mathbf{k}_4] + 5 \text{ p.} \right] \right. \\
&+ \left. \left[2 \frac{\mathcal{M}_{|\mathbf{k}_3+\mathbf{k}_4|}}{\mathcal{M}_{k_1} \mathcal{M}_{k_2}} P_{k_1}^m P_{k_2}^m P_{k_3}^m F^{(2)} [\mathbf{k}_3 + \mathbf{k}_4, -\mathbf{k}_3] + 2 \text{ p.} \right] \right\} + 3 \text{ p.} .
\end{aligned} \tag{E.27}$$

It is better to not further regroup together the two terms since the number of possible permutations is different.

We conclude this i-trispectrum calculation by recalling that up to order ϕ^6 the two remaining terms $T_{(1122)}$ and $T_{(1113)}$ return only the standard expression.

E.4 Recap: all PNG terms

Power Spectrum

$$\begin{aligned}
P^{\text{PNG}}(\mathbf{k}) &= P_{11} + P_{12} \\
&= F_k^{(1)} F_q^{(1)} \mathcal{M}_k^2 \frac{2f_{\text{nl}}^2}{c^4} \int \frac{d\mathbf{p}_a^3}{(2\pi)^3} P_a^\phi P_{|\mathbf{k}-\mathbf{p}_a|}^\phi \\
&\quad + \frac{4f_{\text{nl}}}{c^2} F_k^{(1)} \mathcal{M}_k \int \frac{d\mathbf{p}_a^3}{(2\pi)^3} \mathcal{M}_{p_a} \mathcal{M}_{|\mathbf{k}-\mathbf{p}_a|} F_{a,-\mathbf{k}-\mathbf{p}_a}^{(2)} P_{|\mathbf{k}-\mathbf{p}_a|}^\phi \left[P_a^\phi + 2P_k^\phi \right].
\end{aligned} \tag{E.28}$$

Bispectrum

$$B^{\text{PNG}}(\mathbf{k}_1, \mathbf{k}_2, \mathbf{k}_3) = B_{(111)} = F_{k_1}^{(1)} F_{k_2}^{(1)} F_{k_3}^{(1)} \frac{\mathcal{M}_{k_1}}{\mathcal{M}_{k_2} \mathcal{M}_{k_3}} \frac{2f_{\text{nl}}}{c^2} P_{k_2}^m P_{k_3}^m + \text{cyc.} \tag{E.29}$$

Trispectrum

$$\begin{aligned}
T^{\text{PNG}}(\mathbf{k}_1, \mathbf{k}_2, \mathbf{k}_3, \mathbf{k}_4) &= T_{(1111)} + T_{(1112)} \\
&= F_{k_1}^{(1)} F_{k_2}^{(1)} F_{k_3}^{(1)} F_{k_4}^{(1)} \\
&\quad \times \left\{ \frac{f_{\text{nl}}^2}{c^4} 4 \frac{\mathcal{M}_{k_3} \mathcal{M}_{k_4}}{\mathcal{M}_{k_1} \mathcal{M}_{k_2}} P_{k_1}^m P_{k_2}^m \left[\frac{P_{|\mathbf{k}_1+\mathbf{k}_3|}^m}{\mathcal{M}_{|\mathbf{k}_1+\mathbf{k}_3|}^2} + \frac{P_{|\mathbf{k}_1+\mathbf{k}_4|}^m}{\mathcal{M}_{|\mathbf{k}_1+\mathbf{k}_4|}^2} \right] + 5 \text{ p.} + \frac{g_{\text{nl}}}{c^4} \left[6 \mathcal{M}_{k_4} \frac{P_{k_1}^m P_{k_2}^m P_{k_3}^m}{\mathcal{M}_{k_1} \mathcal{M}_{k_2} \mathcal{M}_{k_3}} + 3 \text{ p.} \right] \right\} \\
&\quad + \frac{f_{\text{nl}}}{c^2} F_{k_1}^{(1)} F_{k_2}^{(1)} F_{k_3}^{(1)} \\
&\quad \times \left\{ \left[4 \frac{\mathcal{M}_{k_1}}{\mathcal{M}_{k_2}} P_{k_2}^m P_{k_3}^m \frac{P_{|\mathbf{k}_3+\mathbf{k}_4|}^m}{\mathcal{M}_{|\mathbf{k}_3+\mathbf{k}_4|}} F^{(2)}[-\mathbf{k}_3, \mathbf{k}_3 + \mathbf{k}_4] + 5 \text{ p.} \right] \right. \\
&\quad \left. + \left[2 \frac{\mathcal{M}_{|\mathbf{k}_3+\mathbf{k}_4|}}{\mathcal{M}_{k_1} \mathcal{M}_{k_2}} P_{k_1}^m P_{k_2}^m P_{k_3}^m F^{(2)}[\mathbf{k}_3 + \mathbf{k}_4, -\mathbf{k}_3] + 2 \text{ p.} \right] \right\} + 3 \text{ p.}
\end{aligned} \tag{E.30}$$

Acknowledgments

D.G. and L.V. thank Francisco Villaescusa-Navarro for invaluable help with the extensive use of the QUIJOTE simulations. D.G. is grateful to Nicola Bellomo and Alex Mead for useful discussions. All authors wish to thank the anonymous referee for the very constructive referee report which improved the paper's presentation.

The measurements from the simulations were performed in the TigerCPU cluster at Princeton. L.V. and D.G. acknowledge support of European Unions Horizon 2020 research and innovation

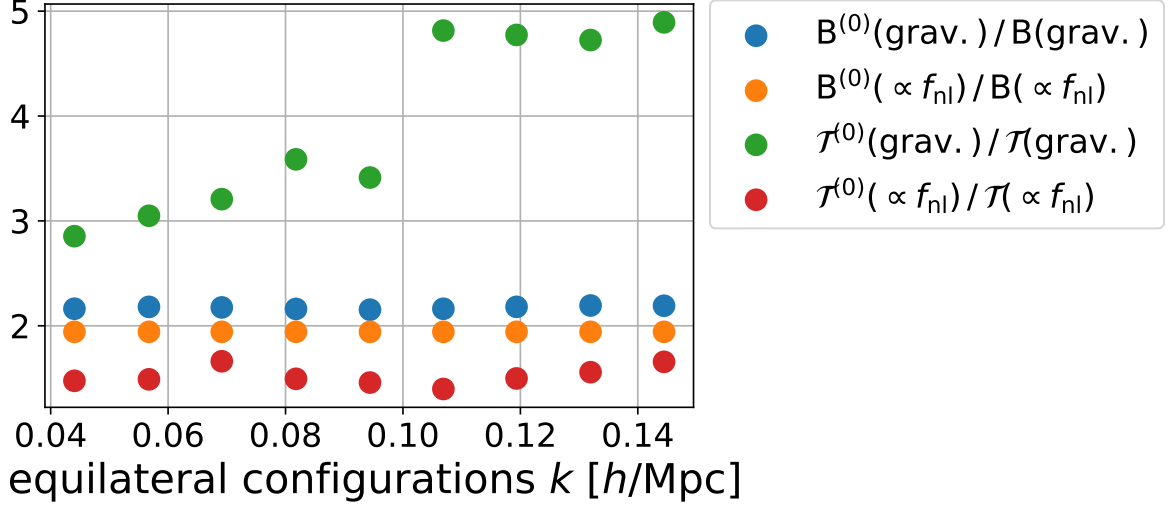


Figure 17. Kaiser boost effect on gravitational and PNG components of the bispectrum and i-trispectrum signals at $z = 0.5$. For clarity only the signal relative to equilateral configurations has been displayed.

programme ERC (BePreSySe, grant agreement 725327). Funding for this work was partially provided by the Spanish MINECO under projects PGC2018-098866-B-I00 FEDER-EU. HGM acknowledges the support from ‘la Caixa’ Foundation (ID100010434) with code LCF/BQ/PI18/11630024.

References

- [1] Paul A. Abell et al. LSST Science Book, Version 2.0. 2009.
- [2] Muntazir Mehdi Abidi and Tobias Baldauf. Cubic Halo Bias in Eulerian and Lagrangian Space. *JCAP*, 07:029, 2018.
- [3] Nishant Agarwal, Vincent Desjacques, Donghui Jeong, and Fabian Schmidt. Information content in the redshift-space galaxy power spectrum and bispectrum. 7 2020.
- [4] Y. Akrami et al. Planck 2018 results. IX. Constraints on primordial non-Gaussianity. 2019.
- [5] Justin Alsing, Tom Charnock, Stephen Feeney, and Benjamin Wand elt. Fast likelihood-free cosmology with neural density estimators and active learning. *MNRAS*, 488(3):4440–4458, September 2019.
- [6] David J. Bacon et al. Cosmology with Phase 1 of the Square Kilometre Array: Red Book 2018: Technical specifications and performance forecasts. *Submitted to: Publ. Astron. Soc. Austral.*, 2018.
- [7] Tobias Baldauf, Uros Seljak, and Leonardo Senatore. Primordial non-Gaussianity in the Bispectrum of the Halo Density Field. *JCAP*, 1104:006, 2011.
- [8] James M. Bardeen. Gauge Invariant Cosmological Perturbations. *Phys. Rev.*, D22:1882–1905, 1980.
- [9] Alexandre Barreira. On the impact of galaxy bias uncertainties on primordial non-Gaussianity constraints. 9 2020.
- [10] N. Bartolo, E. Komatsu, Sabino Matarrese, and A. Riotto. Non-Gaussianity from inflation: Theory and observations. *Phys. Rept.*, 402:103–266, 2004.

- [11] Nicola Bellomo, Nicola Bartolo, Raul Jimenez, Sabino Matarrese, and Licia Verde. Measuring the Energy Scale of Inflation with Large Scale Structures. *JCAP*, 11:043, 2018.
- [12] Daniele Bertolini, Katelin Schutz, Mikhail P. Solon, and Kathryn M. Zurek. The Trispectrum in the Effective Field Theory of Large Scale Structure. *JCAP*, 06:052, 2016.
- [13] Simeon Bird, Matteo Viel, and Martin G. Haehnelt. Massive Neutrinos and the Non-linear Matter Power Spectrum. *Mon. Not. Roy. Astron. Soc.*, 420:2551–2561, 2012.
- [14] Julien Carron. On the assumption of Gaussianity for cosmological two-point statistics and parameter dependent covariance matrices. *Astron. Astrophys.*, 551:A88, 2013.
- [15] Emanuele Castorina et al. Redshift-weighted constraints on primordial non-Gaussianity from the clustering of the eBOSS DR14 quasars in Fourier space. *JCAP*, 09:010, 2019.
- [16] Kwan Chuen Chan and Linda Blot. Assessment of the Information Content of the Power Spectrum and Bispectrum. *Phys. Rev. D*, 96(2):023528, 2017.
- [17] Planck Collaboration, N. Aghanim, Y. Akrami, M. Ashdown, J. Aumont, C. Baccigalupi, M. Ballardini, A. J. Banday, R. B. Barreiro, N. Bartolo, S. Basak, R. Battye, K. Benabed, J. P. Bernard, M. Bersanelli, P. Bielewicz, J. J. Bock, J. R. Bond, J. Borrill, F. R. Bouchet, F. Boulanger, M. Bucher, C. Burigana, R. C. Butler, E. Calabrese, J. F. Cardoso, J. Carron, A. Challinor, H. C. Chiang, J. Chluba, L. P. L. Colombo, C. Combet, D. Contreras, B. P. Crill, F. Cuttaia, P. de Bernardis, G. de Zotti, J. Delabrouille, J. M. Delouis, E. Di Valentino, J. M. Diego, O. Doré, M. Douspis, A. Ducout, X. Dupac, S. Dusini, G. Efstathiou, F. Elsner, T. A. Enßlin, H. K. Eriksen, Y. Fantaye, M. Farhang, J. Fergusson, R. Fernandez-Cobos, F. Finelli, F. Forastieri, M. Frailis, A. A. Fraisse, E. Franceschi, A. Frolov, S. Galeotta, S. Galli, K. Ganga, R. T. Génova-Santos, M. Gerbino, T. Ghosh, J. González-Nuevo, K. M. Górski, S. Gratton, A. Gruppuso, J. E. Gudmundsson, J. Hamann, W. Handley, F. K. Hansen, D. Herranz, S. R. Hildebrandt, E. Hivon, Z. Huang, A. H. Jaffe, W. C. Jones, A. Karacik, E. Keihänen, R. Keskitalo, K. Kiiveri, J. Kim, T. S. Kisner, L. Knox, N. Krachmalnicoff, M. Kunz, H. Kurki-Suonio, G. Lagache, J. M. Lamarre, A. Lasenby, M. Lattanzi, C. R. Lawrence, M. Le Jeune, P. Lemos, J. Lesgourgues, F. Levrier, A. Lewis, M. Liguori, P. B. Lilje, M. Lilley, V. Lindholm, M. López-Cañiego, P. M. Lubin, Y. Z. Ma, J. F. Macías-Pérez, G. Maggio, D. Maino, N. Mandolesi, A. Mangilli, A. Marcos-Caballero, M. Maris, P. G. Martin, M. Martinelli, E. Martínez-González, S. Matarrese, N. Mauri, J. D. McEwen, P. R. Meinhold, A. Melchiorri, A. Mennella, M. Migliaccio, M. Millea, S. Mitra, M. A. Miville-Deschênes, D. Molinari, L. Montier, G. Morgante, A. Moss, P. Natoli, H. U. Nørgaard-Nielsen, L. Pagano, D. Paoletti, B. Partridge, G. Patanchon, H. V. Peiris, F. Perrotta, V. Pettorino, F. Piacentini, L. Polastri, G. Polenta, J. L. Puget, J. P. Rachen, M. Reinecke, M. Remazeilles, A. Renzi, G. Rocha, C. Rosset, G. Roudier, J. A. Rubiño-Martín, B. Ruiz-Granados, L. Salvati, M. Sandri, M. Savelainen, D. Scott, E. P. S. Shellard, C. Sirignano, G. Sirri, L. D. Spencer, R. Sunyaev, A. S. Suur-Uski, J. A. Tauber, D. Tavagnacco, M. Tenti, L. Toffolatti, M. Tomasi, T. Trombetti, L. Valenziano, J. Valiviita, B. Van Tent, L. Vibert, P. Vielva, F. Villa, N. Vittorio, B. D. Wandelt, I. K. Wehus, M. White, S. D. M. White, A. Zacchei, and A. Zonca. Planck 2018 results. vi. cosmological parameters, 2018.
- [18] Asantha Cooray, Chao Li, and Alessandro Melchiorri. The trispectrum of 21-cm background anisotropies as a probe of primordial non-Gaussianity. *Phys. Rev. D*, 77:103506, 2008.
- [19] Paolo Creminelli and Matias Zaldarriaga. Single field consistency relation for the 3-point function. *JCAP*, 10:006, 2004.
- [20] M. Crocce, S. Pueblas, and R. Scoccimarro. Transients from Initial Conditions in Cosmological Simulations. *Mon. Not. Roy. Astron. Soc.*, 373:369–381, 2006.
- [21] Neal Dalal, Olivier Dore, Dragan Huterer, and Alexander Shirokov. The imprints of

primordial non-gaussianities on large-scale structure: scale dependent bias and abundance of virialized objects. *Phys. Rev. D*, 77:123514, 2008.

- [22] G. de Troia, P. A. R. Ade, J. J. Bock, J. R. Bond, A. Boscaleri, C. R. Contaldi, B. P. Crill, P. de Bernardis, P. G. Ferreira, M. Giacometti, E. Hivon, V. V. Hristov, M. Kunz, A. E. Lange, S. Masi, P. D. Mauskopf, T. Montroy, P. Natoli, C. B. Netterfield, E. Pascale, F. Piacentini, G. Polenta, G. Romeo, and J. E. Ruhl. The trispectrum of the cosmic microwave background on subdegree angular scales: an analysis of the BOOMERanG data. *Monthly Notices of the Royal Astronomical Society*, 343(1):284–292, 07 2003.
- [23] Richard Ellis et al. Extragalactic science, cosmology, and Galactic archaeology with the Subaru Prime Focus Spectrograph. *Publ. Astron. Soc. Jap.*, 66(1):R1, 2014.
- [24] Chang Feng, Asantha Cooray, Joseph Smidt, Jon O’Bryan, Brian Keating, and Donough Regan. Planck Trispectrum Constraints on Primordial Non-Gaussianity at Cubic Order. *Phys. Rev. D*, 92(4):043509, 2015.
- [25] J.R. Fergusson, D.M. Regan, and E.P.S. Shellard. Optimal Trispectrum Estimators and WMAP Constraints. 12 2010.
- [26] Matteo Frigo and Steven G. Johnson. The Design and Implementation of {FFTW3}. *Proceedings of the IEEE*, 93(2):216–231, 2005.
- [27] J. N. Fry and P. J. E. Peebles. Statistical analysis of catalogs of extragalactic objects. IX. The four-point galaxy correlation function. *ApJ*, 221:19–33, April 1978.
- [28] James N. Fry. The Galaxy correlation hierarchy in perturbation theory. *Astrophys. J.*, 279:499–510, 1984.
- [29] W. M. Gentleman and G. Sande. Fast fourier transforms: For fun and profit. In *Proceedings of the November 7-10, 1966, Fall Joint Computer Conference*, AFIPS ’66 (Fall), page 563–578, New York, NY, USA, 1966. Association for Computing Machinery.
- [30] Tommaso Giannantonio and Cristiano Porciani. Structure formation from non-Gaussian initial conditions: multivariate biasing, statistics, and comparison with N-body simulations. *Phys. Rev. D*, 81:063530, 2010.
- [31] Hector Gil-Marín, Christian Wagner, Frantzeska Fragkoudi, Raul Jimenez, and Licia Verde. An improved fitting formula for the dark matter bispectrum. *JCAP*, 02:047, 2012.
- [32] Héctor Gil-Marín, Jorge Noreña, Licia Verde, Will J. Percival, Christian Wagner, Marc Manera, and Donald P. Schneider. The power spectrum and bispectrum of SDSS DR11 BOSS galaxies – I. Bias and gravity. *Mon. Not. Roy. Astron. Soc.*, 451(1):539–580, 2015.
- [33] Héctor Gil-Marín, Will J. Percival, Licia Verde, Joel R. Brownstein, Chia-Hsun Chuang, Francisco-Shu Kitaura, Sergio A. Rodríguez-Torres, and Matthew D. Olmstead. The clustering of galaxies in the SDSS-III Baryon Oscillation Spectroscopic Survey: RSD measurement from the power spectrum and bispectrum of the DR12 BOSS galaxies. *Mon. Not. Roy. Astron. Soc.*, 465(2):1757–1788, 2017.
- [34] Héctor Gil-Marín, Christian Wagner, Jorge Noreña, Licia Verde, and Will Percival. Dark matter and halo bispectrum in redshift space: theory and applications. *JCAP*, 12:029, 2014.
- [35] J. Green et al. Wide-Field InfraRed Survey Telescope (WFIRST) Final Report. 8 2012.
- [36] Davide Gualdi, Héctor Gil-Marín, Marc Manera, Benjamin Joachimi, and Ofer Lahav. GEOMAX: beyond linear compression for 3pt galaxy clustering statistics. 12 2019.
- [37] Davide Gualdi, Héctor Gil-Marín, Robert L. Schuhmann, Marc Manera, Benjamin Joachimi, and Ofer Lahav. Enhancing BOSS bispectrum cosmological constraints with maximal compression. *Mon. Not. Roy. Astron. Soc.*, 484(3):3713–3730, 2019.

- [38] Davide Gualdi, Marc Manera, Benjamin Joachimi, and Ofer Lahav. Maximal compression of the redshift space galaxy power spectrum and bispectrum. *Mon. Not. Roy. Astron. Soc.*, 476(3):4045–4070, 2018.
- [39] Davide Gualdi and Licia Verde. Galaxy redshift-space bispectrum: the Importance of Being Anisotropic. *JCAP*, 06:041, 2020.
- [40] ChangHoon Hahn, Francisco Villaescusa-Navarro, Emanuele Castorina, and Roman Scoccimarro. Constraining M_ν with the bispectrum. Part I. Breaking parameter degeneracies. *JCAP*, 03:040, 2020.
- [41] A. J. S. Hamilton. Linear redshift distortions: A Review. In *Ringberg Workshop on Large Scale Structure Ringberg, Germany, September 23-28, 1996*, 1997.
- [42] J. Hartlap, Patrick Simon, and P. Schneider. Why your model parameter confidences might be too optimistic: Unbiased estimation of the inverse covariance matrix. *Astron. Astrophys.*, 464:399, 2007.
- [43] Keisuke Izumi, Shuntaro Mizuno, and Kazuya Koyama. Trispectrum estimation in various models of equilateral type non-Gaussianity. *Phys. Rev. D*, 85:023521, 2012.
- [44] J. C. Jackson. Fingers of God: A critique of Rees’ theory of primordial gravitational radiation. *Mon. Not. Roy. Astron. Soc.*, 156:1P–5P, 1972.
- [45] Donghui Jeong. *Cosmology with high ($z > 1$) redshift galaxy surveys*. PhD thesis, University of Texas at Austin, August 2010.
- [46] Donghui Jeong and Eiichiro Komatsu. Primordial non-Gaussianity, scale-dependent bias, and the bispectrum of galaxies. *Astrophys. J.*, 703:1230–1248, 2009.
- [47] B. Joachimi, X. Shi, and P. Schneider. Bispectrum covariance in the flat-sky limit. *Astron. Astrophys.*, 508:1193, 2009.
- [48] N. Kaiser. Clustering in real space and in redshift space. *Mon. Not. Roy. Astron. Soc.*, 227:1–27, 1987.
- [49] B. Kalus, W.J. Percival, and L. Samushia. Cosmological parameter inference from galaxy clustering: The effect of the posterior distribution of the power spectrum. *Mon. Not. Roy. Astron. Soc.*, 455(3):2573–2581, 2016.
- [50] Marc Kamionkowski, Tristan L. Smith, and Alan Heavens. The CMB Bispectrum, Trispectrum, non-Gaussianity, and the Cramer-Rao Bound. *Phys. Rev. D*, 83:023007, 2011.
- [51] Dionysios Karagiannis, Andrei Lazanu, Michele Liguori, Alvis Raccanelli, Nicola Bartolo, and Licia Verde. Constraining primordial non-Gaussianity with bispectrum and power spectrum from upcoming optical and radio surveys. *Mon. Not. Roy. Astron. Soc.*, 478(1):1341–1376, 2018.
- [52] Eiichiro Komatsu. *The pursuit of non-gaussian fluctuations in the cosmic microwave background*. PhD thesis, Tohoku U., 2001.
- [53] Eiichiro Komatsu and David N. Spergel. Acoustic signatures in the primary microwave background bispectrum. *Phys. Rev.*, D63:063002, 2001.
- [54] M. Kunz, A. J. Banday, P. G. Castro, P. G. Ferreira, and K. M. Górski. The Trispectrum of the 4 Year COBE DMR Data. *ApJ*, 563(2):L99–L102, December 2001.
- [55] R. Laureijs et al. Euclid Definition Study Report. 2011.
- [56] Titouan Lazeyras, Marcello Musso, and Vincent Desjacques. Lagrangian bias of generic large-scale structure tracers. *Phys. Rev. D*, 93(6):063007, 2016.
- [57] Titouan Lazeyras and Fabian Schmidt. Beyond LIMD bias: a measurement of the complete set of third-order halo bias parameters. *JCAP*, 09:008, 2018.

- [58] Hayden Lee and Cora Dvorkin. Cosmological Angular Trispectra and Non-Gaussian Covariance. *JCAP*, 05:044, 2020.
- [59] Julien Lesgourgues. The Cosmic Linear Anisotropy Solving System (CLASS) I: Overview. 4 2011.
- [60] M. Levi, C. Bebek, T. Beers, R. Blum, R. Cahn, D. Eisenstein, B. Flaugher, K. Honscheid, R. Kron, O. Lahav, P. McDonald, N. Roe, D. Schlegel, and representing the DESI collaboration. The DESI Experiment, a whitepaper for Snowmass 2013. *ArXiv e-prints*, August 2013.
- [61] Juan Martin Maldacena. Non-Gaussian features of primordial fluctuations in single field inflationary models. *JHEP*, 05:013, 2003.
- [62] Sabino Matarrese and Licia Verde. The effect of primordial non-Gaussianity on halo bias. *Astrophys. J. Lett.*, 677:L77–L80, 2008.
- [63] Alexander Mead, Catherine Heymans, Lucas Lombriser, John Peacock, Olivia Steele, and Hans Winther. Accurate halo-model matter power spectra with dark energy, massive neutrinos and modified gravitational forces. *Mon. Not. Roy. Astron. Soc.*, 459(2):1468–1488, 2016.
- [64] Shuntaro Mizuno and Kazuya Koyama. Trispectrum estimator in equilateral type non-Gaussian models. *JCAP*, 10:002, 2010.
- [65] Irshad Mohammed, Uros Seljak, and Zvonimir Vlah. Perturbative approach to covariance matrix of the matter power spectrum. *Mon. Not. Roy. Astron. Soc.*, 466(1):780–797, 2017.
- [66] Dipak Munshi, Alan Heavens, Asantha Cooray, Joseph Smidt, Peter Coles, and Paolo Serra. New Optimised Estimators for the Primordial Trispectrum. *Mon. Not. Roy. Astron. Soc.*, 412:1993, 2011.
- [67] Toshiya Namikawa. Constraints on Patchy Reionization from Planck CMB Temperature Trispectrum. *Phys. Rev. D*, 97(6):063505, 2018.
- [68] Toshiya Namikawa. Constraints on patchy reionization from Planck CMB temperature trispectrum. *Phys. Rev. D*, 97(6):063505, March 2018.
- [69] P. J. E. Peebles. *The large-scale structure of the universe*. 1980.
- [70] J. Pielorz, J. Rödiger, I. Tereno, and P. Schneider. A fitting formula for the non-Gaussian contribution to the lensing power spectrum covariance. *A&A*, 514:A79, May 2010.
- [71] Doogesh Kodi Ramanah, Guilhem Lavaux, Jens Jasche, and Benjamin D. Wand elt. Cosmological inference from Bayesian forward modelling of deep galaxy redshift surveys. *A&A*, 621:A69, January 2019.
- [72] Donough Regan, Mateja Gosenca, and David Seery. Constraining the WMAP9 bispectrum and trispectrum with needlets. *Journal of Cosmology and Astroparticle Physics*, 2015(01):013–013, jan 2015.
- [73] Cristiano G. Sabiu, Ben Hoyle, Juhan Kim, and Xiao-Dong Li. Graph Database Solution for Higher Order Spatial Statistics in the Era of Big Data. *Astrophys. J. Suppl.*, 242(2):29, 2019.
- [74] Roman Scoccimarro. The bispectrum: from theory to observations. *Astrophys. J.*, 544:597, 2000.
- [75] Roman Scoccimarro. Fast Estimators for Redshift-Space Clustering. *Phys. Rev. D*, 92(8):083532, 2015.
- [76] Román Scoccimarro, Hume A. Feldman, J. N. Fry, and Joshua A. Frieman. The Bispectrum of IRAS Redshift Catalogs. *ApJ*, 546(2):652–664, January 2001.
- [77] Roman Scoccimarro, Lam Hui, Marc Manera, and Kwan Chuen Chan. Large-scale Bias and Efficient Generation of Initial Conditions for Non-Local Primordial Non-Gaussianity. *Phys. Rev. D*, 85:083002, 2012.

- [78] Roman Scoccimarro, Emiliano Sefusatti, and Matias Zaldarriaga. Probing primordial non-Gaussianity with large - scale structure. *Phys. Rev.*, D69:103513, 2004.
- [79] Emiliano Sefusatti. 1-loop Perturbative Corrections to the Matter and Galaxy Bispectrum with non-Gaussian Initial Conditions. *Phys. Rev. D*, 80:123002, 2009.
- [80] Emiliano Sefusatti, Martin Crocce, and Vincent Desjacques. The Halo Bispectrum in N-body Simulations with non-Gaussian Initial Conditions. *Mon. Not. Roy. Astron. Soc.*, 425:2903, 2012.
- [81] Emiliano Sefusatti, Martin Crocce, Sebastian Pueblas, and Roman Scoccimarro. Cosmology and the Bispectrum. *Phys. Rev. D*, 74:023522, 2006.
- [82] Emiliano Sefusatti, Martin Crocce, Roman Scoccimarro, and Hugh Couchman. Accurate Estimators of Correlation Functions in Fourier Space. *Mon. Not. Roy. Astron. Soc.*, 460(4):3624–3636, 2016.
- [83] Emiliano Sefusatti and Roman Scoccimarro. Galaxy bias and halo-occupation numbers from large-scale clustering. *Phys. Rev. D*, 71:063001, 2005.
- [84] Elena Sellentin and Alan F. Heavens. Parameter inference with estimated covariance matrices. *Mon. Not. Roy. Astron. Soc.*, 456(1):L132–L136, 2016.
- [85] Kendrick M. Smith, Leonardo Senatore, and Matias Zaldarriaga. Optimal analysis of the CMB trispectrum. 2 2015.
- [86] R.E. Smith, J.A. Peacock, A. Jenkins, S.D.M. White, C.S. Frenk, F.R. Pearce, P.A. Thomas, G. Efstathiou, and H.M.P. Couchmann. Stable clustering, the halo model and nonlinear cosmological power spectra. *Mon. Not. Roy. Astron. Soc.*, 341:1311, 2003.
- [87] Volker Springel and Lars Hernquist. Cosmological SPH simulations: A Hybrid multi-phase model for star formation. *Mon. Not. Roy. Astron. Soc.*, 339:289, 2003.
- [88] Naonori S. Sugiyama, Shun Saito, Florian Beutler, and Hee-Jong Seo. A complete FFT-based decomposition formalism for the redshift-space bispectrum. *Mon. Not. Roy. Astron. Soc.*, 484(1):364–384, 2019.
- [89] Naonori S. Sugiyama, Shun Saito, Florian Beutler, and Hee-Jong Seo. Perturbation theory approach to predict the covariance matrices of the galaxy power spectrum and bispectrum in redshift space. 8 2019.
- [90] Yasushi Suto and Takahiko Matsubara. Departure from hierarchical clustering relations for two, three, and four point correlation functions: Analysis of cosmological N body simulations. 3 1993.
- [91] Ryuichi Takahashi, Masanori Sato, Takahiro Nishimichi, Atsushi Taruya, and Masamune Oguri. Revising the Halofit Model for the Nonlinear Matter Power Spectrum. *Astrophys. J.*, 761:152, 2012.
- [92] Atsushi Taruya, Takahiro Nishimichi, and Donghui Jeong. The covariance of the matter power spectrum including the survey window function effect: N-body simulations vs. fifth-order perturbation theory on grid. 7 2020.
- [93] Peter L. Taylor, Thomas D. Kitching, Justing Alsing, Benjamin D. Wandelt, Stephen M. Feeney, and Jason D. McEwen. Cosmic shear: Inference from forward models. *Phys. Rev. D*, 100(2):023519, July 2019.
- [94] Max Tegmark, Andy Taylor, and Alan Heavens. Karhunen-Loeve eigenvalue problems in cosmology: How should we tackle large data sets? *Astrophys. J.*, 480:22, 1997.
- [95] Matteo Tellarini, Ashley J. Ross, Gianmassimo Tasinato, and David Wands. Non-local bias in the halo bispectrum with primordial non-Gaussianity. *JCAP*, 07:004, 2015.

- [96] Matteo Tellarini, Ashley J. Ross, Gianmassimo Tasinato, and David Wands. Galaxy bispectrum, primordial non-Gaussianity and redshift space distortions. *JCAP*, 06:014, 2016.
- [97] Joseph Tomlinson, Donghui Jeong, and Juhan Kim. Efficient parallel algorithm for estimating higher-order polyspectra. *Astron. J.*, 158(3):116, 2019.
- [98] Licia Verde and Alan F. Heavens. On the trispectrum as a Gaussian test for cosmology. *Astrophys. J.*, 553:14, 2001.
- [99] Licia Verde, Alan F. Heavens, Will J. Percival, Sabino Matarrese, Carlton M. Baugh, Joss Bland-Hawthorn, Terry Bridges, Russell Cannon, Shaun Cole, Matthew Colless, Chris Collins, Warrick Couch, Gavin Dalton, Roberto De Propris, Simon P. Driver, George Efstathiou, Richard S. Ellis, Carlos S. Frenk, Karl Glazebrook, Carole Jackson, Ofer Lahav, Ian Lewis, Stuart Lumsden, Steve Maddox, Darren Madgwick, Peder Norberg, John A. Peacock, Bruce A. Peterson, Will Sutherland, and Keith Taylor. The 2dF Galaxy Redshift Survey: the bias of galaxies and the density of the Universe. *MNRAS*, 335(2):432–440, September 2002.
- [100] Licia Verde, Li-Min Wang, Alan Heavens, and Marc Kamionkowski. Large scale structure, the cosmic microwave background, and primordial non-gaussianity. *Mon. Not. Roy. Astron. Soc.*, 313:L141–L147, 2000.
- [101] Francisco Villaescusa-Navarro et al. The Quijote simulations. 9 2019.
- [102] Digvijay Wadekar and Roman Scoccimarro. The Galaxy Power Spectrum Multipoles Covariance in Perturbation Theory. 10 2019.
- [103] Victoria Yankelevich and Cristiano Porciani. Cosmological information in the redshift-space bispectrum. *Mon. Not. Roy. Astron. Soc.*, 483(2):2078–2099, 2019.